

H₆ and mBDCA-5p-H₆ in oxygen-saturated DMF solution. An increase in the limiting current as well as decreasing slope of the Koutecký-Levich (K-L) analysis of diffusion-limited currents (Fig. 3B, inset) is consistent with a greater number of electrons transferred during reduction of oxygen in the presence of mBDCA-5t-H₆ than the one-electron reduction process without mBDCA-5t-H₆ (20). A large excess of cryptand is needed in order to drive the electrochemical process completely to peroxide encapsulation during rotating-disk electrode experiments. K-L analysis of diffusion-limiting currents as a function of the inverse square root of rotation speed, collected in 0.1 M [TBA][ClO₄] DMF solution saturated with 1% O₂ in argon with 4.8 mM mBDCA-5t-H₆ (Fig. 3C), indicates that the number of transferred electrons increases toward an overall two-electron process, which is expected if every oxygen molecule was reduced and encapsulated by the cryptand.

Figure 3D shows a simulation of the cyclic voltammogram using the reaction sequence illustrated in Fig. 4. The reaction sequence used to model the electrochemistry concurs with the established chemical reactivity of O₂ and cryptand described by Fig. 1. Parameters obtained from the simulation are collected in table S5, a and b. Our model suggests that rapid encapsulation of O₂^{•−} by free cryptand drives further one-electron reduction, either directly by the working electrode or through a disproportionation reaction with another equiv of O₂^{•−}, resulting in the formation of [(O₂)₂mBDCA-5t-H₆]^{2−}. The assumption that the diffusion coefficient of O₂ is much greater than that of the cryptand species (table S5b) in DMF containing 0.1 M [TBA][ClO₄] reproduces the sharp feature observed before the wave attributed to one-electron reduction of O₂. An appropriate fit for the anodic sweep could only be accomplished by modeling the oxidation of [(O₂)₂mBDCA-5t-H₆]^{2−} as a series of two, one-electron oxidations.

The reversible one-electron reduction of oxygen in DMF is altered by addition of both strong and weak acids (21). In the case of mBDCA-5t-H₆, the cryptand could serve as a source of protons. However, figs. S27 and S28 illustrate that the reduction of oxygen in the presence of strong and weak acids, respectively, differs from oxygen reduction in the presence of mBDCA-5t-H₆ at equal concentration. These data suggest that the cryptand does not serve as a Brønsted acid in the overall oxygen reduction process.

The electrochemistry of mBDCA-5t-H₆ and mBDCA-5p-H₆ in the presence of oxygen is consistent with reduction of oxygen by one electron to superoxide followed by incorporation into the cryptand cavity, in turn driving disproportionation to give the cryptand-encapsulated peroxide adduct. Oxidation of peroxide dianion within the cavity restores oxygen and the free cryptand ligand. The proposed electrochemical mechanism in Fig. 4 maps on to the observed chemical reactivity of Fig. 1; the combined chemical and electrochemical studies demonstrate encapsulation-driven

chemically reversible two-electron reduction of O₂ to peroxide dianion.

We have synthesized a molecular peroxide dianion adduct by the use of the cavity of hexacarboxamide cryptands as a molecular recognition site. Reduction of oxygen in situ and stabilization of peroxide dianion is facilitated by hydrogen bonding within the cavity of the cryptand, and this process mimics the structural characteristics of biological systems that use peroxide as an oxidant. The use of molecular recognition of an in situ-generated reactive oxygen species has the potential to be incorporated into several technologies, including Li-air batteries, because it is chemically reversible, prevents over-reduction to lithium oxide, and imparts substantial solubility in aprotic media (22). In addition, because the present peroxide adducts can be obtained in high yield in a one-pot reaction and are stable in solution, they could be used as a soluble source of peroxide dianion for a variety of reactions.

References and Notes

1. B. Meunier, Ed., *Metal-Oxo and Metal-Peroxo Species in Catalytic Oxidations* (Springer, Berlin, 2000).
2. B. Meunier, Ed., *Biomimetic Oxidations Catalyzed by Transition Metal Complexes* (Imperial College Press, London, 2000).
3. B. Meunier, S. P. de Visser, S. Shaik, *Chem. Rev.* **104**, 3947 (2004).
4. A. Butler, M. J. Clague, G. E. Meister, *Chem. Rev.* **94**, 625 (1994).
5. M. V. George, K. S. Balachandran, *Chem. Rev.* **75**, 491 (1975).
6. T. Kato *et al.*, *Chem. Lett.* **39**, 136 (2010).
7. M. Grehl, R. Fröhlich, S. Thiele, *Acta Crystallogr. C* **51**, 1038 (1995).
8. S. O. Kang, J. M. Llinares, D. Powell, D. VanderVelde, K. Bowman-James, *J. Am. Chem. Soc.* **125**, 10152 (2003).
9. S. O. Kang, V. W. Day, K. Bowman-James, *J. Org. Chem.* **75**, 277 (2010).
10. G. E. Alliger, P. Müller, C. C. Cummins, D. G. Nocera, *Inorg. Chem.* **49**, 3697 (2010).
11. G. E. Alliger, P. Müller, L. H. Do, C. C. Cummins, D. G. Nocera, *Inorg. Chem.* **50**, 4107 (2011).
12. J. L. Sessler, P. A. Gale, W.-S. Cho, *Anion Receptor Chemistry* (Royal Society of Chemistry, London, ed. 1, 2006).
13. M. García-Viloca, A. González-Lafont, J. M. Lluch, *J. Am. Chem. Soc.* **119**, 1081 (1997).
14. A. K. Boal, J. A. Cotruvo Jr., J. Stubbe, A. C. Rosenzweig, *Science* **329**, 1526 (2010).
15. R. D. Jones, D. A. Summerville, F. Basolo, *Chem. Rev.* **79**, 139 (1979).
16. G. R. Desiraju, T. Steiner, in *The Weak Hydrogen Bond in Structural Chemistry and Biology* (Oxford Univ. Press, Oxford, 1999), p. 13.
17. The residual electron density of refinements without assignment of the electron density of N-H hydrogen atoms surrounding the peroxide moiety suggests that the protons reside at the carboxamide nitrogens of the cryptand, even though the exact position cannot be obtained from x-ray data. Thus, hydroperoxide anion HO₂^{•−} is unlikely to be the species trapped, and the best model obtained was of peroxide dianion (figs. S29 to S32).
18. N. Bartlett, F. O. Sladky, *Chem. Commun.* **1968**, 1046 (1968).
19. D. L. Maricle, W. G. Hodgson, *Anal. Chem.* **37**, 1562 (1965).
20. A. J. Bard, L. R. Faulkner, in *Electrochemical Methods: Fundamentals and Applications* (Wiley, New York, ed. 2, 2000), p. 341.
21. D. T. Sawyer, G. Chiericato Jr., C. T. Angelis, E. J. Nanni Jr., T. Tsuchiya, *Anal. Chem.* **54**, 1720 (1982).
22. G. Girishkumar, B. McCloskey, A. C. Luntz, S. Swanson, W. Wilcke, *J. Phys. Chem. Lett.* **1**, 2193 (2010).

Acknowledgments: This research was supported by the NSF—Centers for Chemical Innovation (CHE-0802907). Grants from the NSF also provided instrument support to the Department of Chemistry Instrument Facility at MIT (grants CHE-9808061 and DBI-9729592). D.J.G. thanks the NSF Graduate Research Fellowship Program for support. We thank Y. Surendranath for productive discussions and collecting mass spectrometry data, A. F. Cozzolino and P. Müller for structure refinement discussions, and F. A. Armstrong for helpful discussions. Complete crystallographic data were deposited in the Cambridge Crystallographic Database Centre (CCDC 831953 to 831955 and 831962).

Supporting Online Material

www.sciencemag.org/cgi/content/full/335/6067/450/DC1
Materials and Methods
Figs. S1 to S32
Tables S1 to S5
References (23–27)

15 August 2011; accepted 13 December 2011
10.1126/science.1212678

A Long-Lived Lunar Core Dynamo

Erin K. Shea,^{1*} Benjamin P. Weiss,¹ William S. Cassata,² David L. Shuster,^{2,3} Sonia M. Tikoo,¹ Jérôme Gattacceca,⁴ Timothy L. Grove,¹ Michael D. Fuller⁵

Paleomagnetic measurements indicate that a core dynamo probably existed on the Moon 4.2 billion years ago. However, the subsequent history of the lunar core dynamo is unknown. Here we report paleomagnetic, petrologic, and ⁴⁰Ar/³⁹Ar thermochronometry measurements on the 3.7-billion-year-old mare basalt sample 10020. This sample contains a high-coercivity magnetization acquired in a stable field of at least ~12 microteslas. These data extend the known lifetime of the lunar dynamo by 500 million years. Such a long-lived lunar dynamo probably required a power source other than thermochemical convection from secular cooling of the lunar interior. The inferred strong intensity of the lunar paleofield presents a challenge to current dynamo theory.

The discovery of remanent magnetization in samples taken by the Apollo lunar missions and by spacecraft observations of the lunar crust has long suggested that the Moon formed a metallic core and a dynamo-generated

magnetic field (*1*). However, the association of magnetization with the antipodes of impact basins and laboratory studies of transient plasma-generated magnetic fields suggest that meteoroid impacts could also be a source of lunar magnetization (*2, 3*).

Because impact fields from the largest basin-forming events are expected to last less than 1 day (2), they should only be recorded by shocked or quickly cooled rocks. Therefore, to identify records of a core dynamo field, it is important to study slowly cooled samples with high magnetic recording fidelity that show no petrographic evidence of shock. Unfortunately, few lunar rocks have all of these properties (1). An exception is lunar troctolite sample 76535, which was observed to have a stable natural remanent magnetization (NRM) formed in a field of ~ 1 to 50 μT that is stable up to coercivities >200 mT (4). The magnetic history of this sample, coupled with its slow (millions of years) cooling time scale, suggests that the Moon had a core dynamo at 4.2 billion years ago (Ga). This re-

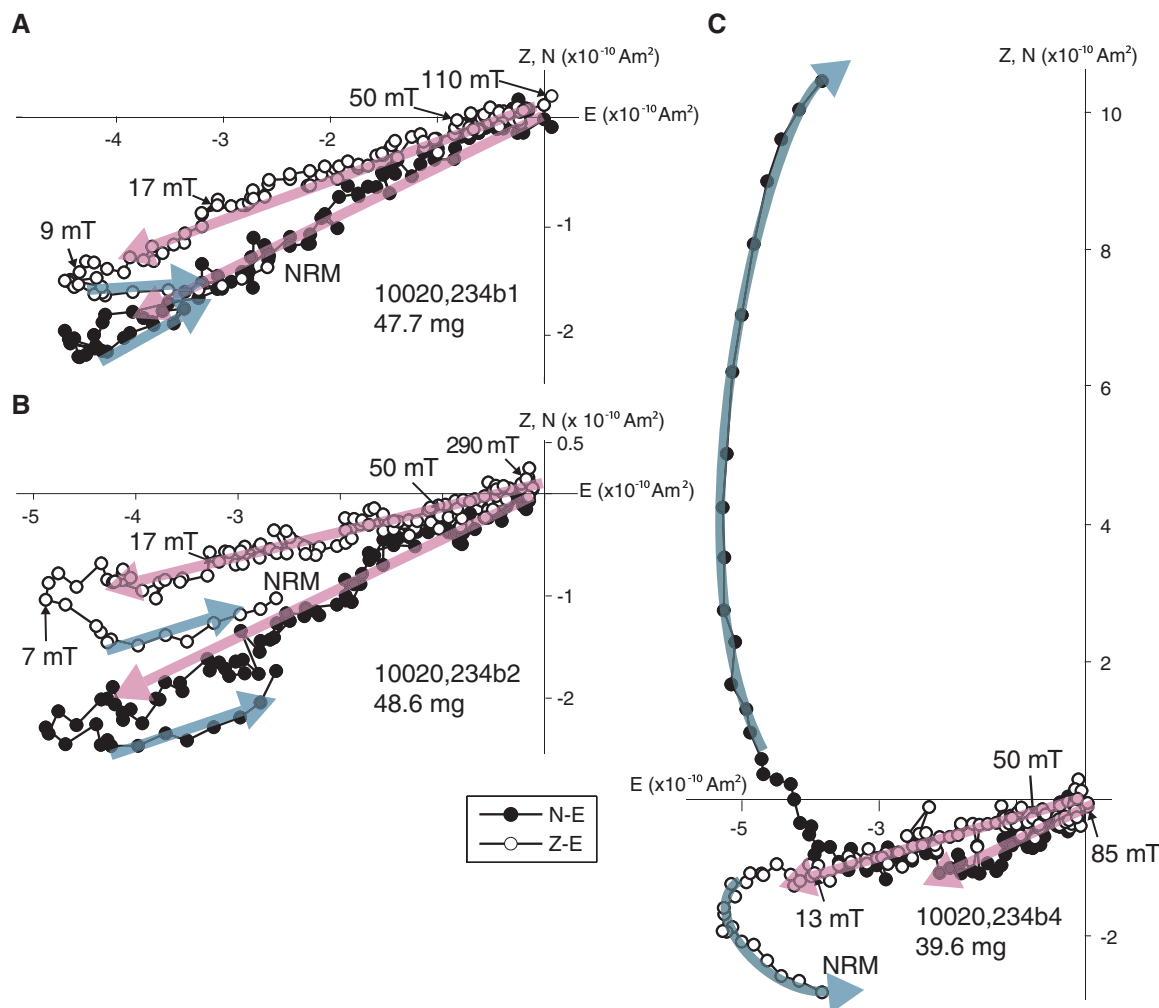
sult is consistent with recent analyses of Apollo-era seismic data (5) and lunar laser ranging (6) that indicate that even today the Moon has a small (~ 330 km in diameter) partially molten metallic core.

The lifetime of the early lunar dynamo remains uncertain. Thermochemical core convection owing to secular planetary cooling, which is widely thought to power most, if not all, dynamos in the present-day solar system (7), is not expected to have persisted beyond ~ 4.2 Ga (8, 9). Therefore, evidence that the dynamo continued after this time would probably indicate that it was powered by an alternative energy source (10, 11). Here we report a paleomagnetic study of another lunar sample with high magnetic recording fidelity, mare basalt 10020. This sample has the potential to contain a record of lunar magnetism 500 million years (My) after troctolite 76535 and has a much simpler thermal history. Furthermore, 10020 formed during a putative high-field epoch of the Moon, when paleofields may have exceeded even that of Earth today (1).

10020 was collected on 20 July 1969 as un-oriented regolith float from the southwestern edge of Mare Tranquillitatis. Along with the

other Apollo 11 basalt samples, 10020 is thought to have been excavated from mostly intact bedrock by the impact that created West Crater at ~ 102 million years ago (Ma) [see supporting online material section 5 (SOM 5) and (12)]. 10020 is a fine-grained, vesicular, low-potassium ilmenite basalt of petrologic group B3 (13), with primary igneous glass (14, 15) and no apparent shock features [SOM 5 and (16)]. Its primary ferromagnetic mineral is kamacite ($\alpha\text{-Fe}_{1-x}\text{Ni}_x$ with $x < 0.02$) [SOM 5 and (16)]. Our petrologic observations (SOM 5) found that plagioclase shows no fracturing, mechanical twinning, or alteration to maskelynite, and olivine shows no undulatory extinction, indicating peak shock pressures <5 GPa. 10020 has an $^{40}\text{Ar}/^{39}\text{Ar}$ age of 3.72 ± 0.04 Ga (17, 18) [recalculated using modern decay constants (19)], which is within error of Rb/Sr crystallization ages of other group B3 Apollo 11 basalts (17, 18). A previous paleomagnetic investigation observed that two un-oriented chips of 10020 displayed some of the most stable NRM of any studied lunar sample (blocked up to at least 50 to 65 mT) [(20) and fig. 30 in (1)], possibly a reflection of its relatively high glass content (SOM 5). The late-stage ($\lesssim 1100^\circ\text{C}$) primary igneous cooling rate of 10020

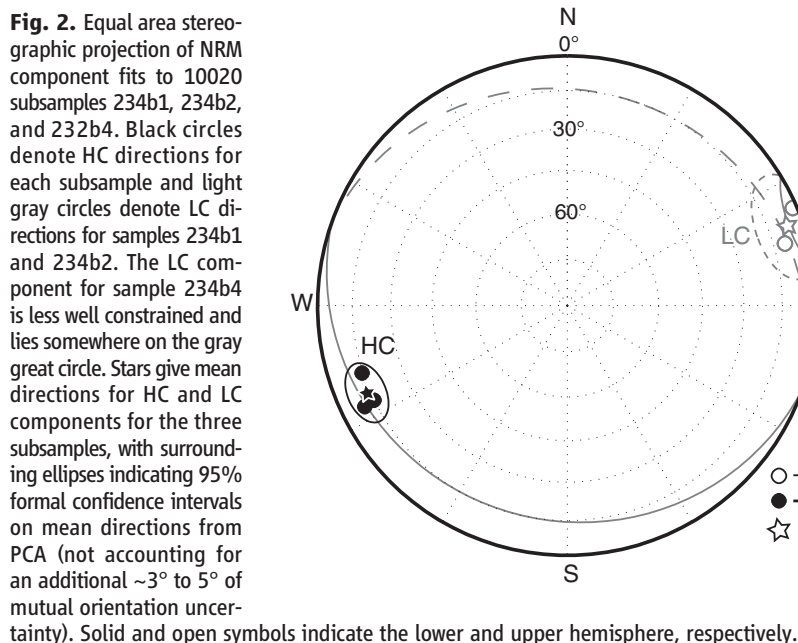
Fig. 1. NRM in mare basalt 10020. Shown is a two-dimensional projection of the NRM vectors of subsamples 234b1, 234b2, and 234b4 during AF demagnetization. Solid symbols represent the end points of magnetization projected onto the horizontal N-E planes, and open symbols represent those projected onto the vertical Z-E planes. Peak fields for selected AF steps are labeled in microteslas. Arrows denote HC component directions determined from principal components analyses (PCA). The mass of each subsample is listed below the sample name. (A) Subsample 234b1. (B) Subsample 234b2. (C) Subsample 234b4.



is estimated to have been $3^{\circ}\text{C hour}^{-1}$ (13), using the maximum plagioclase width cooling indicator [SOM 5 and (21)]. Given that cooling rates

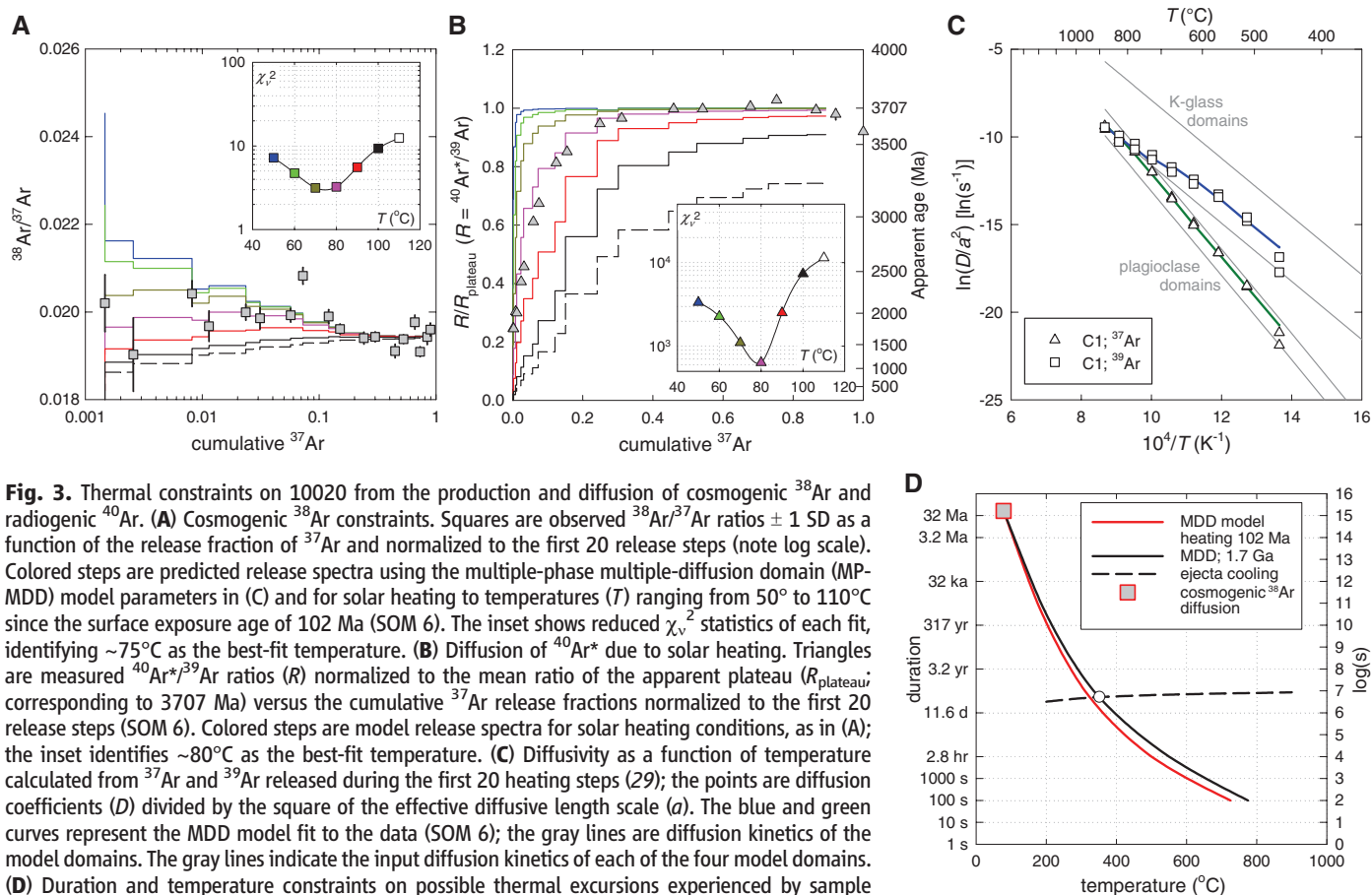
are often slower at lower temperatures, this indicates that cooling and the acquisition of magnetization from the 780°C Curie temperature of

kamacite to ambient lunar temperatures occurred over at least ~ 300 hours, far longer than the lifetime of modeled impact-generated fields.



These features make 10020 an ideal sample for testing the lunar dynamo hypothesis at 3.7 Ga. However, previous paleomagnetic analyses of 10020 (1, 20) did not demonstrate conclusively that the NRM originated on the Moon as a primary thermoremanence (TRM) (SOM 2). More importantly, these studies did not establish whether this field originated from a lunar dynamo or from transient impact-generated fields (SOM 2). We used nondestructive three-axis alternating field (AF) demagnetization to characterize the NRM component in two discrete sets of mutually oriented subsamples, one of which is discussed here and the other in SOM 2.

We identified a low-coercivity (LC) and high-coercivity (HC) component in each subsample (Figs. 1 and 2 and figs. S1 and S3). The LC component, blocked below ~ 17 mT, is approximately unidirectional at the scale of several millimeters but nonunidirectional at larger scales and has a relatively high ratio of NRM to isothermal remanent magnetization (IRM) (ranging up to 8%). These features suggest that the LC component is a secondary IRM resembling that observed in



many other Apollo samples (4, 22, 23) and which is inferred to originate from handling after sampling on the Moon.

Depending on the subsample, the HC component is blocked from 8.5 to 17.5 mT up to >66 to 290 mT and decays linearly to the origin, suggesting that it is the final, primary component. Although the LC and HC components in the three 234b subsamples are antipodal (Fig. 2), other subsamples (SOM 2) do not show this relationship, making it unlikely that this has a rock magnetic source in general. The rate of decay of the HC component during AF demagnetization differs from that of a strong-field IRM or a weak-field pressure remanent magnetization (PRM) acquired at 1.8 GPa (the upper limit of our experimental setup), but is very similar to that of an anhysteretic remanent magnetization (ARM), an analog for TRM (SOM 3 and 4). Furthermore, our PRM acquisition experiments indicate that a very strong field (~700 μ T) would have been necessary to produce the HC component if it were a shock remanent magnetization (SRM) (SOM 4). Our viscous remanent magnetization (VRM) acquisition experiments suggest that no more than 0.1% of the NRM could be a VRM acquired since the sample's arrival on Earth (SOM 4). These data collectively indicate that the HC component is very likely a TRM acquired during primary cooling in a field on the Moon.

The inferred paleointensities (SOM 3) for the HC components for our five subsamples, using anisotropy-corrected IRM and ARM methods, are $66 \pm 37 \mu$ T and $55 \pm 19 \mu$ T (uncertainty ranges are observed from multiple samples with 1 SD) with an overall mean value of 60 μ T and estimated minimum value of ~12 μ T (for comparison, Earth's surface field intensity is ~50 μ T) (SOM 4). Such paleointensities are several orders of magnitude larger than that expected from external sources such as Earth, the Sun, the protoplanetary disk, or the Galaxy at 3.7 Ga (4, 24) and are nearly two orders of magnitude stronger than the strongest crustal remanent fields measured at the Apollo landing sites (1). The very slow cooling rate and lack of shock effects in 10020 suggest that the recorded field was temporally stable, like that expected from a core dynamo.

Although the crystallization age of 10020 is 3.7 Ga, its magnetization could have been acquired during subsequent thermal events. The lack of shock features precludes any brief, high-temperature shock-heating events associated with impacts, but temperature excursions such as those associated with low-grade metamorphism or burial in a hot ejecta blanket are possible. To assess this possibility, we conducted $^{40}\text{Ar}/^{39}\text{Ar}$ and $^{38}\text{Ar}/^{37}\text{Ar}$ thermochronometry on two whole-rock subsamples (SOM 6). We found that 10020 has a weighted average $^{40}\text{Ar}/^{39}\text{Ar}$ plateau age of 3705.6 ± 13.5 Ma [uncertainty 1 SD; includes uncertainty in the decay constant and the age of the fluence monitor (25)], which is indistinguishable from a previous study of this rock as well as

the mean crystallization age of other Apollo 11 group B3 basalts (19). The apparent spatial distributions of radiogenic ^{40}Ar ($^{40}\text{Ar}^*$) and cosmogenic ^{38}Ar ($^{38}\text{Ar}_{\text{cos}}$) within plagioclase and glass (Fig. 3, A and B, and SOM 6) are consistent with diffusive loss of Ar due to heating to a constant temperature of ~80°C since the rock was exposed near the lunar surface at ~102 Ma [as indicated by cosmic ray exposure ages from (17, 18) and our measurements (SOM 6)]. This temperature is essentially the effective temperature equivalent to the expected Ar degassing solely due to solar heating integrated over the exposure age of 10020 (26). As has been concluded for many other Apollo 11 basalts (26), the only apparent thermal disturbance to 10020 since its formation at 3.70 Ga was from solar heating over the past 100 My (27).

Our data thus indicate that a dynamo field, and therefore an advecting metallic core, persisted on the Moon until at least as recently as ~3.70 Ga. It is not yet clear when the dynamo ceased activity. Combined with the paleomagnetic study of the 4.2-billion-year-old troctolite 76535 (4), our data imply a minimum lifetime of 500 My for the lunar dynamo, although it need not have been continuously active throughout the period spanned by these two samples. The lunar dynamo persisted until at least ~130 My after the estimated end of the late heavy bombardment [3.90 to 3.85 Ga (28)] and long after monotonic secular cooling models (9) predict that a core dynamo should have been active. Even non-monotonic models involving the removal of thermal blankets from the core/mantle boundary do not unambiguously generate a dynamo after ~4.4 Ga (8). Potential alternative mechanisms for generating a late lunar dynamo are mechanical stirring of the core by precession (11) or by the impact of large bolides (10). These models predict surface fields at 3.7 Ga of ~0.2 to 15 μ T, although this range is uncertain given that it is derived from scaling laws estimated for convection-driven dynamos. Nevertheless, these values are well below our mean 60 μ T paleointensity estimate and barely overlap our minimum 12 μ T estimate from 10020. Therefore, the late, intense paleomagnetic record from 10020 presents a challenge to current dynamo theory.

References and Notes

1. M. Fuller, S. M. Cissowski, in *Geomagnetism*, J. A. Jacobs, Ed. (Academic Press, Orlando, FL, 1987), vol. 2, pp. 307–455.
2. L. L. Hood, N. A. Artemieva, *Icarus* **193**, 485 (2008).
3. D. A. Crawford, P. H. Schultz, *Int. J. Impact Eng.* **23**, 169 (1999).
4. I. Garrick-Bethell, B. P. Weiss, D. L. Shuster, J. Buz, *Science* **323**, 356 (2009).
5. R. C. Weber, P.-Y. Lin, E. J. Garnero, Q. Williams, P. Lognonné, *Science* **331**, 309 (2011).
6. J. R. Williams, D. H. Boggs, C. F. Yoder, J. T. Ratcliff, J. O. Dickey, *J. Geophys. Res.* **106**, 27933 (2001).
7. D. J. Stevenson, *Space Sci. Rev.* **152**, 651 (2010).
8. D. R. Stegman, A. M. Jellinek, S. A. Zatman, J. R. Baumgardner, M. A. Richards, *Nature* **421**, 143 (2003).

9. W. Konrad, T. Spohn, *Adv. Space Res.* **19**, 1511 (1997).
10. M. Le Bars, M. A. Wiczeorek, Ö. Karatekin, D. Cébron, M. Laneuville, *Nature* **479**, 215 (2011).
11. C. A. Dwyer, D. J. Stevenson, F. Nimmo, *Nature* **479**, 212 (2011).
12. D. W. Beaty, A. L. Albee, *Proc. Lunar Planet. Sci. Conf.* **11th**, 23 (1980).
13. D. W. Beaty, A. L. Albee, *Proc. Lunar Planet. Sci. Conf.* **9th**, 359 (1978).
14. E. Roedder, P. W. Weiblen, *Proc. Apollo 11 Lunar Sci. Conf.*, 801 (1970).
15. M. R. Dence, J. A. V. Douglas, A. G. Plant, R. J. Traill, *Proc. Apollo 11 Lunar Sci. Conf.*, 315 (1970).
16. S. E. Haggerty, F. R. Boyd, P. M. Bell, L. W. Finger, W. B. Bryan, *Proc. Apollo 11 Lunar Sci. Conf.*, 513 (1970).
17. J. Geiss *et al.*, *Philos. Trans. R. Soc. London Ser. A* **285**, 151 (1977).
18. S. Guggisberg *et al.*, *Proc. Lunar Planet. Sci. Conf.* **10th**, 1 (1979).
19. G. A. Snyder, D.-C. Lee, L. A. Taylor, A. N. Halliday, E. A. Jerde, *Geochim. Cosmochim. Acta* **58**, 4795 (1994).
20. D. W. Collinson, S. K. Runcorn, A. Stephenson, A. J. Manson, *Proc. Lunar Sci. Conf.* **3rd**, 2343 (1972).
21. T. L. Grove, D. Walker, *Proc. Lunar Sci. Conf.* **8th**, 1501 (1977).
22. K. P. Lawrence, C. L. Johnson, L. Tauxe, J. Gee, *Phys. Earth Planet. Inter.* **168**, 71 (2008).
23. G. W. Pearce, D. W. Strangway, *Apollo 16 Preliminary Science Report. NASA SP-315* (NASA, Washington, DC, 1972), pp. 7–55 to 7–58.
24. B. P. Weiss *et al.*, *Science* **322**, 713 (2008).
25. P. R. Renne, G. Balco, K. Ludwig, R. Mundil, K. Min, *Geochim. Cosmochim. Acta* **75**, 5097 (2011).
26. G. Turner, *Earth Planet. Sci. Lett.* **11**, 169 (1971).
27. Some other thermal histories cannot be excluded by the Ar data alone. However, the combination of Ar data with geologic constraints strongly favors solar heating as the only major thermal disturbance after primary cooling (SOM 6).
28. C. R. Chapman, B. A. Cohen, D. H. Grinspoon, *Icarus* **189**, 233 (2007).
29. H. Fechtig, S. T. Kalbitzer, in *Potassium Argon Dating*, O. A. Schaeffer, J. Zahring, Eds. (Springer-Verlag, New York, 1966), pp. 68–107.

Acknowledgments: We thank the Johnson Space Center staff and the Curation and Analysis Planning Team for Extraterrestrial Materials for allocating 10020; N. Chatterjee for help with the microprobe analyses; C. Ross for use of her vibrating sample magnetometer; B. Carbone for administrative help; and C. Dwyer, F. Nimmo, M. Wiczeorek, and J. Wisdom for helpful discussions. B.P.W., M.D.F., and D.L.S. thank the NASA Lunar Advanced Science and Exploration Research Program; B.P.W. thanks the NASA Lunar Science Institute; B.P.W. and J.G. thank the MIT-France Seed Funds Program, the PICS Program (CNRS), and the Programme National de Planétologie (INSU/CNRS); E.K.S. and S.M.T. thank the NASA Graduate Student Researchers Program; and D.L.S. thanks the Ann and Gordon Getty Foundation for support. D.L.S. acknowledges the support of NSF grants EAR-0618219 and EAR-0838572. W.S.C. was supported by an NSF Graduate Research Fellowship. Paleomagnetic data have been included in the SOM.

Supporting Online Material

www.sciencemag.org/cgi/content/full/335/6067/453/DC1
SOM Text
Figs. S1 to S24
Tables S1 to S8
References (30–102)
Database S1
Caption for Database S1

17 October 2011; accepted 23 December 2011
10.1126/science.1215359



Supporting Online Material for

A Long-Lived Lunar Core Dynamo

Erin K. Shea,* Benjamin P. Weiss, William S. Cassata, David L. Shuster, Sonia M. Tikoo,
Jérôme Gattacceca, Timothy L. Grove, Michael D. Fuller

*To whom correspondence should be addressed. E-mail: nuptse@mit.edu

Published 27 January 2012, *Science* **335**, 453 (2012)

DOI: 10.1126/science.1215359

This PDF file includes:

SOM Text
Figs. S1 to S24
Tables S1 to S8
References (30–102)
Caption for Database S1

Other Supporting Online Material for this manuscript includes the following:

(available at www.sciencemag.org/cgi/content/full/335/6067/453/DC1)

Database S1: 10020-234 data

1. Introduction

1.1. Overview of samples and measurements. Sample 10020,234 was chipped off from the non-space weathered interior of parent sample 10020,204 using a non-magnetic stainless steel hammer and chisel during our visit to the NASA Lunar Sample Laboratory in May of 2009. Sample 234 was originally composed of two pieces: 234a and 234b. During chipping at NASA, 234a could not be oriented with respect to the rest of the sample. However, 234b was oriented with respect to the host sample. Both subsamples were shipped in a magnetically shielded case to the MIT Paleomagnetism Laboratory (<http://web.mit.edu/paleomag>) where they were stored in our magnetically shielded (DC field <150 nT), class ~10,000 clean room.

Upon arrival at MIT, 234a was subdivided into mutually oriented subsamples 234c and 234d (Set 1), while 234b was subdivided into mutually oriented subsamples 234b1, 234b2, 234b3, and 234b4 (234b3 was kept as a reserve) (Set 2). Each subsample was oriented and glued using non-magnetic cyanoacrylate cement to non-magnetic GE 124 quartz mounts. This and nearly all subsequent sample handling were performed in the magnetically shielded clean room at MIT.

Here we present paleomagnetic measurements of both sets of mutually oriented subsamples of 10020. Our measurements of the natural remanent magnetization (NRM) were conducted with a 2G Enterprises Superconducting Rock Magnetometer 755 (sensitivity $\sim 1 \times 10^{-12}$ Am²). We conducted room temperature three-axis alternating field (AF) demagnetization using a robotic sample handling system integrated with the magnetometer (30). Prior to analysis, the samples had been stored in our magnetically shielded clean room for ~6 months. Following demagnetization, the samples were subjected to paleointensity experiments and various rock magnetic experiments. A small chip of 234c was dated using ⁴⁰Ar/³⁹Ar and ³⁸Ar/³⁷Ar thermochronology. In the following sections we describe each of these analyses.

1.2. The need for a new study of 10020. Previous studies of 10020 (1, 20), while pioneering, had several key limitations: (1) the rock was not fully demagnetized, probably due to the limited fields achievable with AF equipment at the time (such that the primary magnetization component may not have been fully isolated) (2) mutually oriented subsamples were not analyzed [a requirement for establishing the unidirectionality of the magnetization, an important indicator for primary thermoremanent magnetization (TRM) (31)], (3) the NRM was not compared to viscous remanent magnetization (VRM), anhysteretic magnetization (ARM), isothermal remanent magnetization (IRM), and shock remanent magnetization (SRM) or pressure remanent magnetization (PRM) (also important for demonstrating its origin as a TRM); (5) shock petrography was not conducted (necessary for establishing that the NRM is not an SRM); (6) multicomponent paleointensities were not estimated; and (7) detailed ⁴⁰Ar/³⁹Ar thermochronology and cooling history studies were not conducted (critical for determining the age of the magnetization acquisition and the lifetime of the magnetic field, key requirements for timing the lunar dynamo).

2. Alternating field (AF) demagnetization

2.1. Methodology. We chose to conduct AF demagnetization on our samples. This method is advantageous relative to thermal demagnetization for analysis of lunar samples for several reasons. First, heating can permanently alter samples, which compromises their suitability for subsequent paleomagnetic, petrologic, or geochronologic studies. Second, lunar samples are rare, making the loss of a sample for a single analysis unacceptable while other methods exist. Third, many lunar samples have low-field IRM overprints that were acquired during sample handling (4, 23). AF demagnetization is far more effective than thermal demagnetization for removing secondary IRM (22, 32), which can be blocked up to the Curie point but is restricted to low coercivity grains (in the case of 10020, below 8.5-17.0 mT, depending on the subsample; Table S1 and Section 2.2).

As discussed by ref. (31), acquisition of spurious ARM noise and gyroremanent magnetization (GRM) are two disadvantages of AF demagnetization. To reduce spurious ARM noise, we made repeat AF applications (between 5-11 times depending on the field) and calculated the vector mean for each field level. Moment measurements were made after AF application along each of the three orthogonal axes to reduce the effects of GRM [following the Zijdeveld-Dunlop method (4, 31)].

We conducted AF demagnetization up to 290 mT for 234c, to 250 mT for 234d, to 130 mT for 234b1, to 290 mT for 234b2, and to 85 mT for 234b4. NRM magnetization directions were characterized using principal component analysis (PCA) (33).

2.2. Results

2.2.1. NRM. The initial NRM directions of subsamples 234b1 and 234b2 differed by only 11°. However, the NRM direction of 234b4 diverged from 234b1 and 234b2 by 89° and 98°, respectively, and had 4.3 times stronger NRM per unit mass than these two subsamples (Fig. 1). The initial NRM directions of subsamples 234c and 234d diverged by 118° (Fig. S1A and B). Additionally, 234c had a 9× stronger NRM per unit mass than 234d.

2.2.2. Demagnetization of 10020,234b1. This sample had a weak low coercivity (LC) overprint that was removed by AF 8.5 mT (Fig. 1A and Table S1). Above this level, the moment remained in a stable, origin-trending high-coercivity (HC) direction until at least 110 mT, at which point it was essentially fully demagnetized (Fig. 1A and Table S1).

2.2.3. Demagnetization of 10020,234b2. This sample had a weak LC overprint similarly oriented to that of 234b1 that was removed by 6 mT, after which the magnetization reached a stable, origin-trending HC direction almost identical to that of 234b1 until at least 260 mT (Fig. 1B and Table S1), the maximum field reachable by our AF equipment. *This is the most stable NRM component yet identified in any lunar sample.*

2.2.4. Demagnetization of 10020,234b4. This sample contained a much larger LC overprint than either 234b1 or 234b2, lasting until ~12 mT (Fig. 1C and Table S1). The trajectory of the demagnetization vector was curved throughout this low-coercivity range (NRM-12 mT), likely

due to a mixture of components (LC and HC) being demagnetized. This mixture of components made it difficult to confidently identify the LC direction. However, a great circle fit of the trajectory of 234b4 passes through the LC components of both 234b1 and 234b2 (Fig. 2 and Table S1), suggesting that the LC component is unidirectional throughout these three subsamples. Above 12.5 mT, sample 234b4 maintained a stable, HC origin-trending direction almost identical to that of 234b1 and 234b2 until 85 mT, at which point it was essentially demagnetized (Fig. 2 and Table S1).

2.2.5. Demagnetization of 10020,234c. This sample had a strong overprint that was removed by AF 17 mT (Fig. S1A and Table S1). Above this level, the moment remained in an origin-trending direction until at least 66 mT (Fig. S1C and Table S1). After 66 mT, the sample was essentially fully demagnetized.

2.2.6. Demagnetization of 10020,234d. Demagnetization to 9.5 mT removed an LC component 131° away from that of 234c (Fig. S1B and Table S1). Above this level, 234d maintained a stable, origin-trending HC direction that lasted until at least 81 mT (Fig. S1B and Table S1), at which point it was essentially fully demagnetized.

2.2.7. Previous paleomagnetic studies of 10020. Two previous studies were conducted on unoriented subsamples of 10020: subsample 4F and 210 (I, 20). Both samples contained very weak LC overprints and stable, approximately origin-trending HC components. We were able to recover data from 10020,4F (20) (Fig. S2), from which we determined an angular distance of $\sim 26^\circ$ between its two components.

2.2.8. Unidirectionality of components and test for origin-trending magnetization. The HC components are clearly unidirectional within both Set 1 (Fig. S3 and Table S1) and Set 2 (Fig. 2 and Table S1). Within Set 2, the LC component is unidirectional across 234b1, 234b2, and probably also 234b4. However, the LC components in Set 1 are clearly non-unidirectional; they do not overlap within their 95% confidence intervals, nor do they lie on a great circle fit. Furthermore, although the Set 1 subsamples not mutually oriented with respect to those of Set 2, it is clear that, under the assumption that the HC component is unidirectional across all of 10020, the LC components in Set 2 are not unidirectional with respect to either LC component in Set 1: the angular difference between the Fisher mean LC and HC components for Set 2 subsamples is 173° , while the angular difference between the Fisher mean LC and HC components within each of 234c and 234d are 75° and 78° , respectively (with the latter two LC components themselves differing by 131°). This conclusion is supported by data from 10020,4F (discussed in Section 2.2.7).

A qualitative method for testing for origin-trending magnetization is to compare the deviation angle (dANG) (34) of a component from the origin direction to its maximum angular deviation (MAD). Although this test is imperfect because it does not assign a confidence interval to the origin-trending hypothesis, we used it in the absence of other methods. We found that when not forced through the origin, the estimated HC components of all our subsamples except for 234b1 have $MAD > dANG$, suggesting that these components trend to the origin (Table S1). While the unconstrained HC component of 234b1 has a $MAD < dANG$, the two

quantities only differ by 3°, suggesting that the HC component of this sample may trend to the origin as well. Therefore, we conclude that the HC component is likely origin-trending and can be best estimated using origin-constrained fits (Table S1).

2.3. Interpretation. 10020 exhibits no signs of chemical alteration or weathering following eruption, and its metal has the composition of nearly pure iron kamacite (Section 5.2). This indicates that none of the NRM components are likely a chemical remanent magnetization (CRM) from lunar or terrestrial weathering processes or a thermochemical remanence (TCRM) from sub-Curie point phase transformations in taenite during cooling on the Moon. Our VRM experiments indicate that neither the LC or HC component are likely to be a VRM acquired in the Earth's field over the last 40 years (Section 4.4). This leaves the possibility of a partial TRM (pTRM), TRM, IRM, and SRM origin for each component.

The non-unidirectionality of the LC component (see above) further strongly argues against its origin as a pTRM on the Moon when the samples were still together as part of the parent rock. The LC component is also unlikely to be a SRM: it is much softer than a 1.8 GPa PRM (Section 4.3) and 10020 shows no petrographic evidence for shock (Section 5.4). Our paleointensity experiments indicate that the LC component in our subsamples has NRM/IRM values ranging up to 8% (Section 3), suggesting it may be a low-field IRM that has partially viscously decayed. This would also be consistent with the fact that it is not unidirectional: secondary IRM is commonly not unidirectional in extraterrestrial samples due to the curved nature of IRM fields and the fact that it is often acquired during or after cutting (31). These data collectively indicate that the LC component is likely a weak field (~8-17 mT) IRM acquired during sample handling, similar to that seen in numerous other Apollo samples (1, 4, 22, 23).

The HC component's high bulk coercivity (up to >260 mT) (Section 2.2 and Table S1) and low NRM/IRM (1-4%) rule out its origin as a secondary IRM (Section 3). Its high coercivity relative to a 1.8 GPa PRM and the fact that a 700 μ T field would be required to explain its intensity if it were a 5 GPa SRM (Section 4.3) render an SRM origin extremely unlikely. The fact that the HC component is origin-trending (Section 2.2.8) indicates that it is the characteristic (i.e., primary) magnetization in 10020. This suggests that the most likely origin of the HC component is a TRM acquired during primary cooling from the Curie point on the Moon.

3. Paleointensities

3.1. Paleointensity methodology. For terrestrial TRM-bearing igneous rocks, the Thellier-Thellier heating experiment is the preferred method for estimating paleofields. However, alteration can occur during heating, leading to inaccurate paleointensity estimates and destruction of valuable samples. Furthermore, as discussed above, low-field IRM overprints can contaminate Thellier-Thellier paleointensities (22, 32) but will not affect AF-based paleointensity estimates from high coercivity components. Therefore, we chose to use non-destructive room-temperature AF-based techniques to estimate paleointensities from 10020. As described in detail in refs. (4, 24), we normalized the NRM of each subsample to a laboratory IRM and ARM. We did not use the recently developed Preisach method (35, 36) because it is

mainly advantageous for samples dominated by single domain grains (unlike the multidomain grains in 10020; see Section 4.1).

For the IRM experiments, a strong field up to the maximum of the HC component in each subsample (ranging between 130-230 mT depending on the subsample) was applied. For the ARM experiments, two separate estimates were obtained for an AC field of 290 mT and DC bias fields of 50 μ T and 200 μ T for all samples. An additional experiment was performed on Set 2 samples at AC fields between 85-290 mT (peak field chosen to be near that of the maximum coercivity of the HC component in each subsamples) and a DC bias field of 600 μ T (Table S2). The artificial IRM and ARM were progressively AF demagnetized using the same field steps used to demagnetize the NRM. We computed the amount of NRM lost, ARM gained, and IRM lost for each coercivity bin using vector subtraction from the start of each component, and then computed NRM/ARM and NRM/IRM for each NRM component averaged over its coercivity range. Therefore, this is a multicomponent method like that described by ref. (37). Finally, the IRM and ARM paleointensities were then estimated using the following formulas:

$$\text{ARM paleointensity in } \mu\text{T} = (\Delta\text{NRM}/\Delta\text{ARM})/f' \times (\text{bias field in } \mu\text{T}) \quad (1a)$$

$$\text{IRM paleointensity in } \mu\text{T} = (\Delta\text{NRM}/\Delta\text{IRM}) \times a \quad (1b)$$

where f' and a^{-1} are the ratio of TRM to ARM and IRM, respectively. ΔNRM , ΔARM , ΔIRM are, respectively, the vector-subtracted gain or loss of NRM, ARM, and IRM as derived from least squares fits for each component in the paleointensity plots (NRM lost vs. ARM gained and NRM lost vs. IRM lost) in the AF range for a given component.

The unknown values of f' and a for 10020 are the main source of uncertainty in our paleointensity estimates. As described in detail in refs. (4, 24), these quantities vary depending on grain size and shape, with typical values $f' = 1.34$ and $a = 3000$. Nearly all rocks for which TRM/ARM and TRM/IRM have been measured have been found to have f' and a lying within a factor of 3-5 of these values (35, 37-41). A sample with single domain acicular magnetite was observed to have a that is ~50 times larger than this value (42), but such grains are not observed in 10020 (Section 5.2). A recent analysis of these two methods (38) indicates that the IRM method may be more reliable than the ARM method, but that the best approach is to employ both methods and demonstrate that they produce consistent paleointensities. This is our approach.

A secondary source of uncertainty is that associated with the least squares fits to the paleointensity plots. Although far less significant than the systematic uncertainties described above, this uncertainty is still important because it determines whether the slopes in the paleointensity plots are statistically distinguishable from zero (e.g., it permits assessment of the hypothesis of a null field). Therefore, for each paleointensity, we computed the 95% confidence interval on the slope using Student's t -test (Table S2) (43).

3.2. Paleointensity results. A previous IRM paleointensity estimate of 10020,4F using the total REM method (comparison of undemagnetized NRM to saturation IRM) determined a value of 86 μ T (44) (recalculated using our value of a). Our subsamples of 10020 yielded paleointensities ranging between 20-89 μ T from the ARM method and between 33-117 μ T for the IRM method (Fig. S4 and Table S2). Correcting for remanence anisotropy using the ARM anisotropy ellipsoid measured for each subsample (Section 4.5) following ref. (45) gives values ranging

between 20-91 μT from the ARM method and between 33-125 μT for the IRM method (Fig. S4 and Table S2). This range of variability is expected given the uncertainty in the calibration factors for these methods (Section 3.1). The multispecimen average values for the anisotropy-corrected ARM and IRM methods are 54.8 ± 18.8 and 66.2 ± 36.5 μT , and the mean of all experiments is 60.5 μT (Table S2). This similarity between the ARM and IRM values gives confidence that each method is producing relatively accurate results. Given that each individual paleointensity is uncertain by a factor of 3-5 (Section 3.1), the multispecimen mean values should be significantly less uncertain than this factor. Therefore, a very conservative minimum estimate can be obtained if we divide the mean value of all experiments by a factor of 5, giving a value of 12 μT .

3.3. Paleointensity fidelity tests. Many lunar rocks have poor magnetic recording properties and acquire spurious ARM during AF demagnetization (46). Such spurious remanence can mask the underlying NRM and yield inaccurate paleointensity values, particularly for components isolated at high AF demagnetization levels. Therefore, it is important to demonstrate that a particular rock is capable of recording field intensities like those inferred for the NRM. A straightforward approach is to conduct artificial paleointensity experiments in which the sample is given an ARM [as a simulated TRM (47)] in fields of varying intensities, for which a paleointensity is then estimated using the same techniques as those used for the NRM paleointensities. The NRM-derived paleointensity is considered reliable only if the artificial paleointensity experiments accurately retrieve the simulated TRM at equivalent field levels.

With this goal, we gave 10020,234d various ARMs using an AC field of 85 mT and DC bias fields of 100, 50, 20, and 10 μT . We call these “artificial NRMs”. Using the same value of TRM/ARM as that used for the NRM paleointensity experiments ($f' = 1.34$), the artificial NRMs correspond to TRMs acquired in fields of 75, 37, 15, and 7 μT , respectively. We AF demagnetized the artificial NRMs using the same protocol used for the true NRM and then computed paleointensities via the ARM method using bias fields of 50 and 200 μT . We found that we could retrieve applied fields in the range of the average anisotropy-corrected paleointensity (50-100 μT) (Table S2) with 1-10% accuracy (Fig. S5 and Table S3).

4.0. Rock magnetism

4.1. Hysteresis data. To determine the domain state of the ferromagnetic grains in 10020, we measured room temperature hysteresis loops on subsample 234c with a Digital Measurement Systems vibrating sample magnetometer in the laboratory of C. Ross at MIT. The high-field slope (between 1 and 0.95 T) of the hysteresis loop was used to estimate the contribution of paramagnetic minerals. This contribution was subtracted from the loops to recover the ferromagnetic contribution. The results (Fig. S6 and Table S4) indicate ratios of saturation remanence to saturation magnetization (M_{rs}/M_s) and coercivity of remanence to coercivity (H_{cr}/H_c) (where H_{cr} was measured using IRM experiments described in Section 4.2) that are characteristic of a mean grain size in the multidomain range (48). Nevertheless, 10020 shows more single-domain characteristics (relatively high M_{rs}/M_s and low H_{cr}/H_c) than the majority of lunar basalts [compare Table S4 with Fig. 22 of ref. (1)]. This is likely part of the explanation for its relatively stable NRM (Section 2).

4.2. ARM and IRM experiments. We conducted a variety of remanence experiments to constrain the origin of the NRM, determine the coercivity spectrum, assess the degree of magnetostatic interactions, and constrain the ferromagnetic mineralogy in 10020. Samples 234d and 234b4 were given stepwise ARM in increasing DC bias fields from 0.2 to 2 mT in a peak AC field of 200 mT (Fig. S7) to infer the degree of magnetostatic interactions in the sample (49). Following ARM acquisition, the ARM was then stepwise AF demagnetized. The two samples were then given an IRM in a field of 200 mT that was also subsequently stepwise AF demagnetized (Fig. S8). Sample 234b4 was also subjected to progressive IRM acquisition (Fig. S8). IRM acquisition data and AF demagnetization of IRM data are indicators of the coercivity spectrum of the sample. The field at which IRM acquisition and AF demagnetization of IRM curves intersect is indicative of H_{cr} , as is the back field value at which the remanence goes to zero. Finally, a comparison of normalized curves of AF demagnetization of ARM and IRM (Fig. S9) constitutes the Lowrie-Fuller test, an indicator of grain size and stress state (50, 51).

The Lowrie-Fuller test indicates that 10020 exhibits high-field-type (IRM more stable than ARM) behavior, consistent with kamacite in the pseudo single domain to multidomain size range (see also Section 4.1). ARM susceptibility (Fig. S7) and Cisowski R values (49) (Fig. S8, Table S4) indicate that 10020 contains moderately interacting multidomain grains. IRM acquisition and demagnetization data (Fig. S8) and H_{cr} values are consistent with the presence of multidomain kamacite [and not the high coercivity mineral tetrataenite (52, 53)] as the dominant ferromagnetic phase in 10020.

The HC component of the NRM demagnetizes very similarly to an ARM and differently than an IRM (Fig. S8). Given that ARM is a reasonable analog for TRM (47), this provides good evidence in favor of a TRM origin for the HC component. As shown next, the demagnetization characteristics of PRM also make SRM unlikely to account for the HC component.

4.3. PRM experiments. It is important to demonstrate that the NRM preserved in 10020 could not have been produced by a shock. This is because SRM is acquired virtually instantaneously and can therefore record a short-lived magnetic field like that which might be produced by impact-generated plasmas (3, 54) rather than long-lived dynamo fields. Furthermore, our paleointensity techniques, which are calibrated for TRM, would only give lower limits on the true paleointensity for a SRM because this form of magnetization is typically less efficient than TRM [e.g., (55)].

Although our thin section analysis (Section 5.2) eliminates exposure to shock pressures above 5 GPa, pressures below 5 GPa will not leave identifiable petrographic features. To assess the effect of lower pressure shocks, we compared the NRM demagnetization to laboratory-induced PRM. Low pressure (<5 GPa) PRM has been found to have AF demagnetization properties almost indistinguishable from SRM produced at the same peak pressure. PRM experiments were conducted at CEREGE in Aix-en-Provence, France. All sample preparation was conducted in the CEREGE non-magnetic room (DC fields <400 nT). Sample 234d was placed in a Teflon cup filled with fluid to ensure hydrostatic pressurization and then inserted into a non-magnetic pressure vessel. The vessel was then placed in a calibrated field-generating coil. Following setup, the coil current was turned on to produce a field of 800 μ T and the sample was

raised to the desired pressure. The sample was left at pressure for 1 minute and then slowly depressurized. After return to ambient pressure, the sample was unloaded from the pressure vessel subjected to stepwise AF demagnetization. Although this pressure is applied for a considerably longer period than a meteorite impact, comparative experiments have shown that the duration of the applied pressure has no significant effect on the acquired magnetization (56). These experiments were conducted for pressures of 0.4, 0.9, 1.4, and 1.8 GPa.

Like previous such studies of lunar rocks (56), we found that PRM was acquired dominantly by low-coercivity grains ($< \sim 30\text{--}40$ mT), with even the 1.8 GPa PRM significantly softer than the NRM (Fig. S9). This suggests that the neither the LC nor the HC components are likely SRM. We observed a linear relationship between the acquired SRM intensity and pressure (Fig. S10). This linear relationship holds for both the undemagnetized PRM as well as the PRM after demagnetization to 10 mT. With these relationships, we estimated the total PRM and the PRM demagnetized to 10 mT that would be produced by a 5 GPa shock in a 800 μT field (Fig. S10). These values allow us to calculate the paleofield intensity that would have been necessary to produce the observed LC and HC components (e.g., NRM blocked above and below AF 10 mT) assuming they were a 5 GPa PRM:

(2a)

$$\text{Paleofield (LC)} = \text{lab field} \times [\text{NRM} - \text{NRM}(\text{AF } 10 \text{ mT})] / [\text{PRM}(5 \text{ GPa}) - \text{PRM}(5 \text{ GPa}, 10 \text{ mT})]$$

(2b)

$$\text{Paleofield (HC)} = \text{lab field} \times \text{NRM}(\text{AF } 10 \text{ mT}) / \text{PRM}(5 \text{ GPa}, 10 \text{ mT})$$

where NRM(AF 10 mT) and PRM(5 GPa, 10 mT) are the NRM and 5 GPa PRM after demagnetization to 10 mT, respectively. Using the above experiments, we find that a 110 μT and a 700 μT field would have been necessary to produce the LC and HC components, respectively. Both fields (especially the latter) are high relative to estimates of dynamo fields on the Moon (1) and limits on impact-generated fields that have been inferred from terrestrial impact craters [e.g., (57, 58)]. Therefore, these field values provide further evidence against an SRM origin for either NRM component.

4.4. VRM experiments. Another possible source of the magnetization in 10020 is VRM acquired at ambient temperatures during exposure to the Earth's field over the last ~ 40 y. To estimate this contribution, we conducted two laboratory VRM acquisition experiment on sample 234c. During the two experiments, the sample was placed in the Earth's field in a fixed position for 6 days 11 hours and 37 min (first experiment) and 7 days 4 hours and 33 min (second experiment). After each exposure, it was returned to our shielded room and, after about 30 s, its magnetization was repeatedly measured to determine the intensity of the acquired VRM and its decay rate with time (Fig. S11).

We found that a weak VRM (6.69×10^{-11} and 2.44×10^{-11} Am^2 , equivalent to 0.5% and 0.2% of the initial NRM) was acquired during each experiment. As has been observed in many previous experiments (24, 59), the decay rate of VRM was distinctly non-linear with $\log(\text{time})$, indicating that it is not possible to unambiguously fit for a magnetic viscosity decay coefficient $S_d = d(\text{VRM lost})/d[\log(\text{time})]$. Although we cannot unambiguously determine the VRM decay rate over 40 y without conducting a 40 y-long experiment, we can estimate the VRM acquired on Earth for various assumed decay functions. An extrapolation of a linear fit to the later time data

(red line in Fig. S11), would predict that the total VRM resulting from 40 y of exposure to the Earth's field [$\log(\text{time}) = 9.1 \log(\text{s})$] followed by viscous decay in our magnetically shielded room for ~6 months [$\log(\text{time}) = 7.2 \log(\text{s})$] prior to our first NRM measurements would be ~0.14% of the observed NRM for this sample. Alternatively, an exponential fit (black line in Fig. S11) would predict that 3.0% of the observed NRM could be a VRM. Linear and exponential fits to data from the second experiment predict similarly low amounts of terrestrial VRM (0.12% and 0.43% of the initial NRM). Regardless of the precise functional form of VRM acquisition and decay, it is clear that neither the LC nor the HC components in 10020 are likely to be a VRM from exposure to the Earth's field. Rather, the high paleointensities and non-unidirectionality of the LC component suggest it is an IRM from sample handling, while the HC component is likely a primary TRM (Section 2.3).

4.5. Magnetic anisotropy. Paleomagnetic directions and paleointensity values inferred from samples with strong remanence anisotropy can be biased if this anisotropy is not taken into account. To check this possibility, we measured the ARM and IRM anisotropy of all samples except 234c, which was partially destroyed for radiometric dating (Table S1). We applied an IRM (20 mT) and ARM (80 mT AC field, 2 mT DC field) in three orthogonal directions to construct an anisotropy matrix and then solved for the principal axes of the ARM and IRM anisotropy ellipsoids following refs. (60, 61). We repeated each of these experiments twice and observed consistent results. The results show that only the smallest subsample, 234b4, required substantial paleointensity corrections (Table S2).

Following ref. (45) we calculated the ancient field direction (H_{anc}) by multiplying the measured HC direction by the ARM anisotropy tensor. Dividing the remanence acquired in a unit field parallel to the ancient field and the remanence acquired in a unit field in the laboratory field direction gives the ratio r of magnetization due to the ancient field and magnetization from the laboratory field. Dividing the paleointensity by r yields the anisotropy-corrected paleointensity.

4.5.1. Anisotropy of 10020,234b1. We found that the ARM and IRM anisotropies of sample 234b1 have degrees (62) of $P = 1.08$ and 1.18 , respectively, and shape factors (63) of $T = -0.16$ and -0.64 , suggesting a prolate fabric. Average HC direction and paleointensity corrections using the ARM ellipsoid are 3° and 5% , respectively.

4.5.2. Anisotropy of 10020,234b2. Anisotropy measurements of subsample 234b2 yielded degrees of ARM and IRM anisotropy of $P = 1.07$ and 1.17 , respectively, and shape factors of $T = 0.40$ and 0.23 , respectively, suggesting an oblate fabric. Average HC direction and paleointensity corrections using the ARM ellipsoid are 1° and 1% , respectively.

4.5.3. Anisotropy of 10020,234b4. Anisotropy measurements of 234b4, our smallest subsample, yielded degrees of ARM and IRM anisotropy of $P = 1.52$ and 1.96 , respectively, and ARM and IRM shape factors of $T = 0.46$ and 0.51 , respectively, indicating an oblate fabric. Average HC direction and paleointensity corrections the ARM ellipsoid are 7° and 50% , respectively.

4.5.4. Anisotropy of 10020, 234d. The anisotropy experiment on 234d gave a degree of ARM and IRM anisotropy of $P = 1.27$ and 1.51 , respectively and an ARM and IRM shape factor of $T =$

-0.70 and -0.65, respectively, suggesting a prolate fabric. Average HC direction and paleointensity corrections the ARM ellipsoid are 1.5° and 1%, respectively.

5. Geologic and Petrologic observations

5.1. Geology of the Apollo 11 landing site. Apollo 11 initially planned to land in the impact ejecta directly surrounding West Crater, a ~200 m diameter, 30 m deep, sharp-rimmed impact crater in the southwestern region of Mare Tranquillitatis (Fig. S12A). However, upon arrival at the landing site, the rocky terrain forced Armstrong to land approximately 0.5 km west of the crater. The Eagle landed on a flow of high-Ti, high-K basalt [petrologic group A of (12, 19)]. Ejecta from West Crater are clearly present at the landing site and it is thought that much of the float in the area is from this young (Copernican), fresh crater (Fig. S12B) (12, 64). Basaltic samples collected during the extra-vehicular activity (EVA) span a range of compositions, textures, and isotopic ages, and can be divided into five petrologic groups: A, B1, B2, B3, and D (13). These petrologic groups can be further subdivided into three magmatic groupings (from youngest to oldest): A, B1-B3, and B2-D (65, 66). The low-K group B2 and D basalts represent the earliest volcanic activity sampled at the Apollo 11 site (~3.85 Ga) (19, 66). Approximately 150 My later, the relatively high-Ti and low-K groups B1 and B3 (to which 10020 belongs) were erupted. Finally, the high-K group A, the youngest basalts sampled by Apollo 11, was erupted at ~3.6 Ga to form the present surface for most of the southwest portion of Tranquillitatis. Spectral mapping using Galileo and Clementine data indicate that groups A and B1-B3 are continuous at the basin scale, with groups B1-B3 possibly extending as far north as the Apollo 17 landing site in southeastern Mare Serenitatis (65).

Using the five petrologic groupings (see above), isotopic ages, and petrographically estimated cooling rates, a stratigraphic section can be assembled that places the deepest (and oldest) rocks a minimum of 30 m below the present lunar surface (12). Despite their range of compositions and ages, Apollo 11 basalt samples other than group A basalts have remarkably similar cosmic ray exposure (CRE) ages (around 100 Ma) and show no evidence for pre-irradiation, while group A basalts have CRE ages ranging up to ~500 Ma and show evidence for pre-irradiation. This suggests that group A basalts were exposed at the surface and that all Apollo 11 basalts were excavated by a single impact at 100 Ma (12). Excavation of the inferred minimum ~30 m stratigraphic thickness would require a simple crater at least ~200 m in diameter [assuming a transient crater depth-to-diameter ratio of ~0.14 (67)]. This crater-formation event was likely relatively recent: a rock the size of 10020 [which had a mass of 425 g (68)], which is mid-range in mass among the returned basalt samples (69), would have a ~70% probability of being destroyed after ~100 My of surface exposure and a ~99% probability of being destroyed after 200 My of surface exposure (69). Although there are other large craters in the vicinity of Tranquility Base (Fig. S12A, B), these other craters are heavily degraded and no longer have visible rays composed of blocky ejecta. West Crater is the only obvious sharply defined (and therefore young) crater within ~700 m of the landing site that is deep enough to have excavated such a large (~30 m) stratigraphic thickness [ref. (70) and Fig. S12A] [note that the group B3 basalts like 10020 are thought to have originated from >15 m depth (12)]. Both astronaut surface photos and satellite imagery suggest that one of the blocky rays of West Crater crosses the landing site and is likely the source of the returned basalts [ref. (12) and Fig. S12B]

5.2. Overall petrographic description. 10020 is an ophitic-intergranular, fine-grained (~200 μm mean grain size) quartz-normative low-K ilmenite basalt (13, 68). The major phases are plagioclase, pyroxene, and ilmenite with accessory minerals including metal (<0.05 vol.%) and K-rich aluminosilicate glass [~1-2 vol. %, calculated by dividing the whole rock K_2O abundance (13) by the abundance of K_2O measured in the glass (Table S5)].

We conducted electron microprobe analyses and backscattered electron microscopy (BSEM) in the MIT Electron Microprobe Facility on 30 μm thin section 10020,75 (Figs. S13 and S14). We used a JEOL 8200 microprobe with 15 keV accelerating voltage, 10 nA beam current, and a spot size less than 1 μm . Raw analytical data were reduced using the $\phi(\rho z)$ algorithm (71) implemented by Paul Carpenter as CITZAF (72) in the JEOL software. Matrix corrections for oxides use the Armstrong correction (73) and metals use the XPP correction (74).

We observed similar mineral assemblages and compositions as those previously described including the three main Ar-bearing phases K-glass, plagioclase and pyroxene (Table S5 and Section 6.4) (13). Our microprobe analyses indicate that the plagioclase is essentially unzoned (variation in K_2O is below the minimum detectability limit). Our BSEM and microprobe analyses of metal in 10020,75 found that it is typically intergrown with troilite (Fig. S14) and has a composition of nearly pure metallic iron ($\text{Fe}_{1-x}\text{Ni}_x$ with $x < 0.02$) (Table S5), in agreement with Apollo-era measurements (16). This composition indicates an essentially pure kamacite ($\alpha\text{-Fe}$) structure with Curie point of 780°C [Fig. 1 of (75)]. Because the high temperature taenite phase ($\gamma\text{-Fe}$) with this bulk composition transforms fully to kamacite at 912°C, which is above kamacite's Curie temperature (75), the kamacite in 10020 should have acquired a pure TRM during primary cooling rather than the TCRM that forms when $x > 0.03$ (76).

5.3. Cooling rate analysis. Like some Apollo basalts, petrologic studies of 10020 indicate a two-stage cooling history, with an early rapid phase of cooling at high temperatures followed by a slower rate at lower temperatures. Using the correlation between concentration of Al in pyroxene and cooling rate in lunar basalts (77), measurements of Al in 10020 pyroxene indicate an early stage (>~1100°C) cooling rate of ~30°C h⁻¹. For temperatures of ~1100°C and below, cooling rate studies of quartz-normative mare basalts (21) have established that both the width of plagioclase laths and pyroxene phenocryst nucleation density directly correlate with late-stage cooling rate. We therefore measured the width of the [010] face (perpendicular to albite twinning) of the most pristine plagioclase laths in 10020 (Fig. S15). We found that the mean observed width of the large laths was ~50 μm , indicating a cooling rate of ~3°C/hour, essentially identical to that previously estimated for this sample (13). Given that cooling rates are expected to slow further at even lower temperatures, these data indicate that 10020 cooled from the Curie point of iron (~780°C) to ambient surface temperatures (ranging between ~-170°C to 100°C) over a period of >300 hours.

5.4. Shock effects. We observed no petrographic evidence for shock in 10020: plagioclase does not exhibit any mechanical twinning, fracturing, or alteration to maskelynite, and olivine does not show undulatory extinction (Figs. S13 and S15). Following ref. (78), this indicates that 10020 could not have experienced peak shock pressures greater than 5 GPa.

6. $^{40}\text{Ar}/^{39}\text{Ar}$ and $^{38}\text{Ar}/^{37}\text{Ar}$ thermochronology

6.1. $^{40}\text{Ar}/^{39}\text{Ar}$ analyses. Two whole rock aliquots of 10020,234c (subsamples 234c1 and 234c2 with masses of 2.81 and 3.40 mg, respectively) were subjected to $^{40}\text{Ar}/^{39}\text{Ar}$ analyses at the Berkeley Geochronology Center. The samples were placed into aluminum discs alongside Hb3gr neutron fluence monitors and were irradiated for 100 hours at the Oregon State University TRIGA reactor in the Cadmium-Lined In-Core Irradiation Tube (CLICIT) facility. Following irradiation, the whole-rock fragments were loaded into small metal tubes of high purity Pt-Ir alloy and incrementally degassed using feedback-controlled laser heating with a 150 W diode laser (wavelength of 810 ± 10 nm) equipped with a coaxially aligned optical pyrometer. To account for the temperature dependent emissivity of the Pt-Ir metal, the single-color pyrometer was calibrated against a type-K thermocouple under high vacuum ($<10^{-8}$ torr) and under the same conditions as the diffusion experiments (i.e., same alloy, viewport, cover slide, and focal point).

During the Ar analyses, the samples were first held under static vacuum at a controlled temperature for 600 s. The degassed Ar was then purified using one hot and one cold SAES getter, and analyzed with a Mass Analyzer Products 215-50 mass spectrometer using a Balzers SEV-217 electron multiplier. Corrections were made for interfering nuclear reaction products (79), ^{37}Ar and ^{39}Ar decay, spectrometer discrimination, and extraction line blanks. Apparent ages were calculated relative to the Hb3gr standard (1081 Ma) using the decay constants and standard calibration of (25) and isotope abundances of (80) (full datasets appear in Table S6).

CRE ages were calculated from the ratio of cosmogenic ^{38}Ar ($^{38}\text{Ar}_{\text{cos}}$) to reactor-produced ^{37}Ar ($^{37}\text{Ar}_{\text{Ca}}$) according to the following equation:

$$\text{CRE Age} = \left(\frac{^{38}\text{Ar}_{\text{cos}}}{^{37}\text{Ar}_{\text{Ca}}} \right) \left(\frac{\gamma}{P38_{\text{Ca}}} \right) \quad (3)$$

where $P38_{\text{Ca}}$ is the production rate of $^{38}\text{Ar}_{\text{cos}}$ relative to the Ca concentration and γ is the irradiation parameter relating $^{37}\text{Ar}_{\text{Ca}}$ to Ca content [see (81) for additional details]. By mass balance, the $^{38}\text{Ar}/^{36}\text{Ar}$ ratio defines the proportion of cosmogenic and trapped Ar isotopes (assuming these are the only two sources) according to the following equation:

$$^{38}\text{Ar}_{\text{cos}} = ^{38}\text{Ar}_T \left[1 - \frac{1.54 - (^{38}\text{Ar}/^{36}\text{Ar})_{\text{meas}}}{1.54 - 0.19} \right] \quad (4)$$

where 1.54 is the cosmogenic $^{38}\text{Ar}/^{36}\text{Ar}$ ratio (82) and 0.19 is the trapped $^{38}\text{Ar}/^{36}\text{Ar}$ ratio (83). We assumed a 1% uncertainty on both of these numbers. $P38_{\text{Ca}}$, adapted from (84), is given by

$$P38_{\text{Ca}} = 8.08 + 0.44 \left(\frac{[\text{Fe} + \text{Ni}]}{[\text{Ca}]} \right) + 1.70 \left(\frac{[\text{Ti} + \text{Cr} + \text{Mn}]}{[\text{Ca}]} \right) + 12.9 \left(\frac{[\text{K}]}{[\text{Ca}]} \right) \quad (5)$$

where the elemental concentrations are in weight-% and $P38_{Ca}$ is in units of 10^{-13} moles per gram of Ca per Ma. Exposure ages are listed in Table S7.

6.2. Overall results. Our two analyzed subsamples yielded extremely similar $^{40}\text{Ar}/^{39}\text{Ar}$ and $^{38}\text{Ar}/^{37}\text{Ar}$ release spectra (Fig. S16). We found that our two samples exhibited relatively low apparent $^{40}\text{Ar}/^{39}\text{Ar}$ ages in the first ~40% of ^{37}Ar release (with initial step ages of ~1.7 Ga) and plateau ages of 3706.6 ± 3.4 and 3704.8 ± 2.9 Ma (analytical uncertainties given as one standard deviation), for a weighted mean age of 3705.6 ± 2.2 Ma [± 13.5 when uncertainties in the decay constant and age of the fluence monitor are propagated following ref. (25)]. Our samples yielded concordant $^{38}\text{Ar}_{\text{cos}}/^{37}\text{Ar}$ ratios throughout the plateau portions of the age spectra. The $^{38}\text{Ar}_{\text{cos}}$ released at these temperatures is predominantly derived from plagioclase ($P38_{Ca} = 8.081 \times 10^{-13}$ mol/g_{Ca}/Ma) and yields exposure ages of 101.8 ± 0.8 and 102.6 ± 0.6 Ma for the two samples [one standard deviation uncertainties not including uncertainty on the production rate], for a weighted mean exposure age of 102.3 ± 0.5 Ma (Table S7). These results are very similar to the previous study of 10020 (18), with the important exception that our heating schedule had much higher gas release resolution. As described below, these data permitted us to accurately quantify thermal events which could have produced the degassed initial part of the $^{40}\text{Ar}/^{39}\text{Ar}$ data age spectrum. We also quantified the effects of post-formational thermal events on cosmogenically produced ^{38}Ar , which allowed us to better temporally constrain the thermal events because of the relatively young exposure age of 10020.

6.3. Thermal modeling of $^{40}\text{Ar}/^{39}\text{Ar}$ data. Using feedback-controlled thermal extractions (85, 86), the stepwise release of nuclides produced via neutron irradiation (i.e., ^{39}Ar and ^{37}Ar) can be used to quantify the kinetics of Ar diffusion from the hosting phase (29). Assuming that the Ar diffusion kinetics observed at laboratory conditions also applies to natural conditions, this information can be used to test various thermal histories through geologic time that would result in the apparent spatial distribution of radiogenic ^{40}Ar ($^{40}\text{Ar}^*$) or cosmogenic ^{38}Ar ($^{38}\text{Ar}_{\text{cos}}$), as constrained by observed $^{40}\text{Ar}^*/^{39}\text{Ar}$ and $^{38}\text{Ar}_{\text{cos}}/^{37}\text{Ar}$ stepwise release spectra [e.g., Fig. S16; (87)]. In the following section, we describe a number of thermal modeling strategies to constrain permissible thermal conditions of sample 10020 from the observed $^{40}\text{Ar}/^{39}\text{Ar}$ datasets (Table S6). We present these models in order of increasing complexity and compare their results.

6.3.1. Constructing the single-domain models. Under the most simplifying set of assumptions, the linear Arrhenius relationships for ^{37}Ar observed in the first 20 extractions of both samples 234c1 and 234c2 (Fig. S17A) can be assumed to be the effective kinetics of Ar diffusion from plagioclase (85, 86). Using the fraction of $^{39}\text{Ar}_K$ and $^{37}\text{Ar}_{Ca}$ from the first 20 steps and the duration of each step, we calculated the Ar diffusion coefficient (D) normalized to the square of the effective diffusive length-scale (a) following refs. (29, 88), assuming an effective spherical geometry. Assuming that the $^{40}\text{Ar}^*/^{39}\text{Ar}$ ratios of these steps reflect the production and diffusion of $^{40}\text{Ar}^*$ in plagioclase since the apparent plateau age of ~3700 Ma (Fig. S17C), we constrain permissible thermal paths using a single-domain, spherical production and diffusion model. We determined E_a and $\ln(D/a^2)$ based on the linear ^{37}Ar Arrhenius array (Fig. S17A). Non-linearity observed in the ^{39}Ar Arrhenius array is discussed below. We initially assume that diffusive loss of $^{40}\text{Ar}^*$ primarily occurred either at (a) the ~102 Ma CRE age determined from the ^{38}Ar

abundance (see below and Table S7), or (b) during a reheating event at ~ 1.7 Ga, as inferred from the remarkable agreement in initial step ages of both aliquots (Fig. S16). Based solely on the Ar release data, these two points in time may correspond to, and bound the timing of, impact events.

We find that these simple models are remarkably successful in predicting the observed $^{40}\text{Ar}^*/^{39}\text{Ar}$ spectra of both aliquots (Fig. S17C). Best-fitting models of this class are identified by a misfit statistic (Fig. S18A) and provide duration and temperature constraints on the hypothetical reheating events at 102 Ma and 1.7 Ga shown in Fig. S18B. The best-fit temperature (T) value for each t was identified by the minimum in polynomial curves fit to reduced chi squared (χ_v^2) values for a range in T . Under this set of assumptions, these constraints correspond to specific values of Dt/a^2 and place an upper bound on the duration-temperature pairs if all $^{40}\text{Ar}^*$ diffusion happened at either 102 Ma or 1.7 Ga. Alternatively, any reheating event that occurred between these points in time would plot between the curves shown in Fig. S18B.

Despite the apparent success of these models at explaining the age spectra, they clearly fail to predict the apparent Ca/K ratio spectra (Fig. S17B) calculated from the observed $^{37}\text{Ar}/^{39}\text{Ar}$ ratios, which increase by ~ 10 over the course of each analysis. This failure is also evident in the nonlinear Arrhenius plot calculated from ^{39}Ar release. Thus, the assumption that ^{37}Ar and ^{39}Ar are uniformly distributed within plagioclase is invalid, or another significant repository of one of these isotopes exists (e.g., K-glass) (Fig. S17A).

6.3.2. Constructing the K/Ca zonation models. Failure of the simple single-domain models (Section 6.3.1) to predict the $^{37}\text{Ar}/^{39}\text{Ar}$ release spectra indicates that more sophisticated models are required to completely explain the Ar dataset. Using otherwise the same set of assumptions above, we calculated new models by instead assuming that the domain is spatially zoned in Ca/K, with relatively high K concentration at the domain edge (Fig. S19). A non-uniform distribution of K within a single diffusion domain would predict the entire dataset well (Fig. S19) and provide similar thermal constraints as the single-domain model with a uniform K distribution. However, as discussed in Section 5.2, strong K-zonation in plagioclase was not observed in our electron microprobe analyses.

6.4. Kinetics of Ar diffusion in whole-rock sample 10020,234c. The Arrhenius plots and release spectra of whole-rock analyses of sample 10020 reflect contributions of Ar isotopes from multiple phases with different diffusion kinetics, including potassium-rich aluminosilicate glass (K-glass), plagioclase, pyroxene, olivine, and Fe-Ti oxides. Electron microprobe analyses were used to determine the relative abundances of these minerals, as well as their K, Ca, Fe, Ti, Cr, Mn, and Ni concentrations [ref. (13) and Table S5]. These data constrain the relative contributions of each phase to the total abundances of observed radiogenic ^{40}Ar ($^{40}\text{Ar}^*$), $^{39}\text{Ar}_\text{K}$, $^{38}\text{Ar}_\text{cos}$, $^{37}\text{Ar}_\text{Ca}$, and $^{36}\text{Ar}_\text{cos}$. K-glass is the primary host of $^{40}\text{Ar}^*$ and $^{39}\text{Ar}_\text{K}$, followed by plagioclase. Plagioclase is the primary host of $^{38}\text{Ar}_\text{cos}$, $^{36}\text{Ar}_\text{cos}$, and $^{37}\text{Ar}_\text{Ca}$, followed by pyroxenes. Olivine and Fe-Ti oxides are minor sources of $^{38}\text{Ar}_\text{cos}$ and $^{36}\text{Ar}_\text{cos}$.

Obtaining an accurate thermal history for sample 10020 requires knowledge of Ar diffusion kinetics in the phases containing Ar. Using a uniformly distributed Ar isotope (e.g., $^{39}\text{Ar}_\text{K}$ or $^{37}\text{Ar}_\text{Ca}$), a detailed laboratory heating schedule (Table S6) can isolate Ar released from different phases of interest. Our low temperature heating schedule (including duplicate 600 s

extractions at 50°C increments between 400 and 800°C) isolated the release of $^{39}\text{Ar}_\text{K}$ and $^{37}\text{Ar}_\text{Ca}$ from K-glass and plagioclase, respectively. Pyroxenes, olivine, and Fe-Ti oxides in sample 10020 appear to completely retain Ar over laboratory timescales at these low temperatures.

6.4.1. Estimation of diffusion coefficient. Using the fraction of $^{39}\text{Ar}_\text{K}$ and $^{37}\text{Ar}_\text{Ca}$ released and the duration of each step, we again calculated D/a^2 following refs. (29, 88) and assuming an effective spherical geometry (Fig. S20). The fractional release of $^{39}\text{Ar}_\text{K}$ and $^{37}\text{Ar}_\text{Ca}$ was normalized to the total abundances observed in the first 20 extractions (i.e., the K-glass and plagioclase portion of the age spectrum). Because the analyzed whole-rock fragments contain a distribution of grain (domain) sizes, the resulting Arrhenius arrays are non-linear (Fig. S20A). A multiple-phase, multiple-diffusion domain (MP-MDD) model was therefore constructed to reproduce the observed Arrhenius plot. Below we outline the procedure that was used to determine the activation energy (E_a) of each phase and domain distribution parameters (D_0/a^2 and Φ_{X-Y}) (summarized in Table S8). Φ_{X-Y} is the proportion of gas within each domain, where X designates model domain 1 or 2 of K-glass or plagioclase and Y designates ^{39}Ar or ^{37}Ar (Table S8). Additional information regarding MDD models and their applications to multi-phase samples can be found in refs. (89) and (81), respectively.

6.4.2. Constructing the MP-MDD model. We now list our procedures and assumptions used to quantify parameters of the multiple-phase MDD models. Our selections were based on the observed Ar data measured via stepwise degassing (Table S6), optical petrography and electron microprobe data [ref. (13) and Table S5].

- 1) We calculated the fraction of $^{39}\text{Ar}_\text{K}$ contained within plagioclase using the average large plagioclase Ca/K ratio (~800; Table S5) and the total abundance of $^{37}\text{Ar}_\text{Ca}$ [i.e., we assumed that all of the $^{37}\text{Ar}_\text{Ca}$ is contained within plagioclase, as indicated by the modal abundance of plagioclase relative to K-glass and its high Ca concentration (Table S5)].
- 2) The remaining $^{39}\text{Ar}_\text{K}$ (89%) was assigned to K-glass, which implies the relative modal abundance of plagioclase to K-glass is 33:1, consistent with electron microprobe observations (Table S5).
- 3) A small fraction of the total $^{37}\text{Ar}_\text{Ca}$ (<0.1%) was assigned to the K-glass such that the average Ca/K ratio was 0.32, as observed by electron microprobe analyses (Table S5).
- 4) Linear regressions to extractions that yielded reproducible D/a^2 values at a given temperature were used to constrain the E_a for Ar diffusion in K-glass and plagioclase. Steps 3-14 were included in the $^{37}\text{Ar}_\text{Ca}$ (plagioclase) regression, which yielded an E_a of 199.6 kJ mol⁻¹, consistent with published values for Ar diffusion in plagioclase (85). Steps 3-6 were included in the $^{39}\text{Ar}_\text{K}$ (K-glass) regression, which yielded an E_a of 138.1 kJ mol⁻¹, consistent with published values for Ar diffusion in silicate glasses (90) and in maskelynite in ALH 84001 (81).
- 5) Two domains were assigned to each phase. Additional domains would improve the goodness of fit between the observed and modeled Arrhenius arrays, but are not necessary.
- 6) The proportion of $^{39}\text{Ar}_\text{K}$ contained within the smaller K-glass domain (Φ_{1-39} for K-glass; Table S8) was quantified by the cumulative fraction of $^{39}\text{Ar}_\text{K}$ released prior to the

departure from linearity observed on the $\ln(r/r_o)$ plot [Fig. S21A and ref. (89)]. $\ln(r/r_o)$ is the natural logarithm of the deviation between a calculated value of D/a^2 and the linear reference defined by the earliest released argon used to quantify E_a of each phase (corresponding to a domain of radius r_o). This plot reveals a departure in the apparent domain size r from r_o , which we use to quantify Φ_{X-Y} . For example, Φ_{1-39} for K-glass = 0.21 (Fig. S21A). The remaining $^{39}\text{Ar}_K$ allocated to K-glass was assigned to the larger domain (Φ_{2-39} for K-glass).

- 7) The fraction of $^{37}\text{Ar}_{Ca}$ contained within the smaller plagioclase domain (Φ_{1-37} for plagioclase) was given by the cumulative fraction of $^{37}\text{Ar}_{Ca}$ released prior to the departure from linearity observed on a plot of $\ln(r/r_o)$ (Φ_{1-37} for plagioclase = 0.599; Fig. S21B). The remaining $^{37}\text{Ar}_{Ca}$ allocated to plagioclase was assigned to the larger domain (Φ_{2-37} for plagioclase).
- 8) The fraction of $^{39}\text{Ar}_K$ allocated to plagioclase was divided between the domains such that the domain Ca/K ratios reflected the variation observed in electron microprobe analyses (600-1000; Table S5).
- 9) The fraction of $^{37}\text{Ar}_{Ca}$ allocated to K-glass was divided between the domains such that the domain Ca/K ratios reflect the variation observed in electron microprobe analyses (0.2-0.45; Table S5).
- 10) The frequency factor (D_o/a^2) of each domain was a free parameter to optimize the goodness of fit between the modeled and observed Arrhenius plots.

The MP-MDD model parameters quantified by this procedure are summarized in Table S8. This model is consistent with the mineralogy and chemistry of sample 10020 and reproduces the observed Arrhenius plot and Ca/K spectrum for our laboratory heating schedule (Fig. S16). Our MP-MDD models indicate that K-glass is expected to lose a small fraction of Ar (<5%) during irradiation heating and extraction-line bake-out [average temperature of $\sim 270^\circ\text{C}$; (91)]. All models included this heating prior to the laboratory schedule to simulate diffusive loss during irradiation and extraction-line bake-out.

6.5. The thermal history of 10020. Age spectra obtained from 10020 are clearly discordant due to post-crystallization loss of radiogenic Ar. Certainly, this cannot be due to direct shock heating, since the peak shock pressure experienced by 10020 is below 5 GPa, indicating negligible heating (92). This leaves non-shock heating as the only viable mechanism. Amongst the various such possible scenarios, 10020 was unlikely to have been heated in a hot ejecta blanket at 100 Ma (the assumed excavation age of West Crater given the common CRE age of Apollo 11 basalts; see Section 5). This is because 10020 was sampled at the lunar surface, probably as part of a thin crater ray (see Section 5). In this section, we discuss two such thermal histories capable of producing the observed age discordance and discuss the strengths and weaknesses of each.

6.5.1. Episodic loss of Ar following burial in an ejecta blanket by an impact event at ~ 1.7 Ga. Initial step ages obtained from detailed laboratory heating schedules have been shown to record the timing of diffusive loss of $^{40}\text{Ar}^*$ [e.g., ref. (86)]. As discussed above, given the agreement in the initial step ages of both aliquots (Fig. S16 and Table S6), we initially assume that loss of

$^{40}\text{Ar}^*$ primarily occurred at this time, ~ 1.7 Ga. Mare volcanism in the vicinity of the Apollo 11 site apparently ceased by ~ 3.5 - 3.6 Ga (93), which precludes reheating due to near-surface magmatism. More likely, heating associated with an impact event may have partially reset the K-Ar system at ~ 1.7 Ga. Although 10020 cannot have been directly shock-heated (see above), it may have been diffusively heated following burial in an ejecta blanket with surrounding hot, shocked country rock and impact melt.

Observed cosmogenic Xe isotopes in sample 10020 (94) require that the sample received no subsurface irradiation prior to exposure at the lunar surface at 102 Ma, as constrained by the $^{38}\text{Ar}_{\text{cos}}/^{37}\text{Ar}_{\text{Ca}}$ ratio of plagioclase (Table S7). Thus, any ejecta blanket in which sample 10020 was buried prior to 102 Ma must have been sufficiently thick to shield the rocks from cosmic rays (i.e., >3 m beneath the surface). In Fig. S22, using the MP-MDD model, we show simple duration-temperature (t - T) constraints on thermal excursions at 1.7 Ga that predict the observed $^{40}\text{Ar}/^{39}\text{Ar}$ spectra. Again, the best-fit T value for each t was identified by the minimum in polynomial curves fit to reduced chi squared (χ^2_{ν}) values for a range in T (Fig. S23). The t - T curve shown in red represents the time t required to diffusively cool a rock from an initial temperature T to $<100^\circ\text{C}$ in the middle of a nominal 6 m thick ejecta blanket (i.e., 3 m below the surface), assuming the thermal diffusivity is $10^{-6} \text{ m}^2\text{s}^{-1}$. The intersection of these two curves approximates the thermal history of 10020 in a cooling ejecta blanket under this set of assumptions. In this scenario, the geologic history of sample 10020 could be summarized by the following:

- 1) Sample 10020 crystallized at ~ 3.70 Ga, as quantified by the plateau portion of the age spectrum (Fig. S16B)
- 2) At ~ 1.7 Ga, the sample was ejected from its bedrock location and deposited in a hot ejecta blanket of >3 m in thickness. Here it cooled from a peak temperature of $\sim 400^\circ\text{C}$ to ambient surface temperatures over several thousands of years, resulting in the diffusive loss of $^{40}\text{Ar}^*$.
- 3) At ~ 102 Ma, a second impact event brought 10020 to the surface where the observed cosmogenic ^{38}Ar was then produced.

6.5.2. Loss of Ar resulting from lunar surface temperatures due to prolonged solar heating. Daily surface temperatures in equatorial regions like the Apollo 11 landing site exceed 100°C (95, 96). As has been suggested for other Apollo 11 basalts (26), such elevated temperatures are sufficient to cause diffusive loss of Ar from K-glass and plagioclase in sample 10020 over its 102 Ma of near-surface exposure. Using our MP-MDD model, we simulated 102 My of simultaneous production and diffusive loss of $^{40}\text{Ar}^*$ and $^{38}\text{Ar}_{\text{cos}}$ due to daytime heating. We modeled the solar heating as a step function from -273°C (i.e., no Ar diffusion) to a specified temperature for half of the duration of cosmogenic ^{38}Ar production. Given that the actual solar heating of the analyzed samples is a function of the lunation cycle, local shadows and cm-scale depth beneath the exposed rock (97), a square-pulse model temperature will underestimate the maximum surface temperatures at the 10020 location, and instead represents an effective mean temperature of diffusion that integrates such complexity. Because diffusivity is exponentially dependent on temperature, a square-pulse temperature will not be substantially lower than the peak temperature of the sample through the lunation cycle. We discretized the calculation by 0.5

My steps; more information on our $^{40}\text{Ar}^*$ production-diffusion code can be found in refs. (81, 85, 98). The $^{38}\text{Ar}_{\text{cos}}$ production-diffusion code is identical to this $^{40}\text{Ar}^*$ code except production is linear through time and dependent on the concentration of both K and Ca in each domain (Table S8). Domain-specific production rates (moles of $^{38}\text{Ar}_{\text{cos}}/\text{g}_{\text{Ca}}/\text{Ma}$) based on a Ca:K production ratio of 1.0:1.6 (84) are listed in Table S8. Although our use of domain-specific Ca/K ratios somewhat improves the fit to the apparent Ca/K spectra (Fig. S16A), the overall model results are not strongly sensitive to this choice. Following a given thermal history, the relative abundances of $^{38}\text{Ar}_{\text{cos}}$ in each domain were normalized to the measured total (Table S8) such that the modeled and measured $^{38}\text{Ar}_{\text{cos}}/^{37}\text{Ar}_{\text{Ca}}$ ratios were directly comparable.

In Figs. 3 and S24, we show modeled $^{38}\text{Ar}_{\text{cos}}/^{37}\text{Ar}_{\text{Ca}}$ and $^{40}\text{Ar}^*/^{39}\text{Ar}_{\text{K}}$ age spectra resulting from daytime heating at temperatures of 40 to 110°C, alongside the observations. For both isotope systems, a square-pulse equivalent of daytime heating at 80°C predicts model spectra that best fit the observed data. The internal consistency of this diffusion temperature for both radiogenic $^{40}\text{Ar}^*$ (that primarily accumulated over 3.6 Gy) and cosmogenic ^{38}Ar (that was produced over only 102 My) suggests that this scenario is realistic. Moreover, this is almost exactly the effective temperature calculated by ref. (26) [see his equation (7)] as an equivalent to integrating $^{40}\text{Ar}^*$ degassing due to heating over the lunar day-night cycle for other Apollo 11 samples with activation energies close to 10020. In this scenario, the geologic history of sample 10020 is summarized by the following:

- 1) Sample 10020 crystallized at ~3.70 Ga.
- 2) At ~102 Ma it was ejected from its bedrock location (presumably by the West Crater impactor; see Section 5) and deposited near the lunar surface where daily temperature excursions exceed 80°C. Under these conditions, the simultaneous production and diffusion of cosmogenic ^{38}Ar resulted in the apparent $^{38}\text{Ar}_{\text{cos}}/^{37}\text{Ar}_{\text{Ca}}$ spectrum, while the distribution of $^{40}\text{Ar}^*$ that had accumulated during the prior ~3.6 Ga was diffusively perturbed.

6.5.3. Which thermal history is correct? Of the three scenarios just described, prolonged heating at elevated surface temperatures (Section 6.5.2) probably offers the simplest and most internally-consistent explanation for the apparent diffusive loss of Ar from sample 10020. Five observations support this interpretation:

- 1) Initial step $^{38}\text{Ar}_{\text{cos}}/^{37}\text{Ar}_{\text{Ca}}$ values are significantly lower than predicted by models without surface heating¹, indicating diffusive loss of $^{38}\text{Ar}_{\text{cos}}$ (Fig. S24A). Because this cosmogenic Ar was only produced in the last ~100 Ma when 10020 was near the surface, it would be very difficult to account for its diffusive loss without solar heating.
- 2) If such diffusive loss occurred, it must also have affected $^{40}\text{Ar}^*$. As expected, both the $^{40}\text{Ar}^*/^{39}\text{Ar}_{\text{K}}$ and $^{38}\text{Ar}_{\text{cos}}/^{37}\text{Ar}_{\text{Ca}}$ spectra are best fit by daytime heating at ~80°C, providing an internally consistent solution for two independent nuclide production mechanisms.

¹ The predicted $^{38}\text{Ar}_{\text{cos}}/^{37}\text{Ar}_{\text{Ca}}$ spectra rapidly declines from an initial value of ~0.025, which reflects gas derived from K-glass with a high production rate of $^{38}\text{Ar}_{\text{cos}}$ per gram of Ca (i.e., high K/Ca ratio), to ~0.019, which reflects gas derived from plagioclase with a low production rate of $^{38}\text{Ar}_{\text{cos}}$ per gram of Ca (i.e., high Ca/K ratio; see 50°C model in Fig. S24A).

- 3) The temperature predicted by both isotope systems ($\sim 80^\circ\text{C}$) is in good agreement with independent estimates of the effective constant lunar surface temperature at the Apollo 11 landing that yields the same amount of Ar degassing as the lunar day-night cycle (26).
- 4) This scenario is most consistent with the geology of the Apollo 11 landing site (Section 5.1) and exposure ages of the other Apollo 11 basalts. As discussed by (12), all the Apollo 11 basalts, including the type B3 basalts of which 10020 is a member, have the same exposure age of ~ 100 Ma except for those basalts that outcrop at the surface [the 3.6 Ga type A (high-K) basalts], which instead have exposure ages ranging from ~ 20 -500 Ma. Furthermore, Xe data indicate that the type A basalts but not the other Apollo basalts were preirradiated prior to ejection, consistent with their outcropping on the surface and shielding the underlying older basalts like 10020 (Section 5.1).

The proposed ~ 100 Ma age for the ejection event is generally consistent with the $^{40}\text{Ar}^*/^{39}\text{Ar}$ age spectra of the Apollo 11 basalts. All Apollo 11 basalt $^{40}\text{Ar}^*/^{39}\text{Ar}$ measurements have initial steps with ages ranging from near zero to <2.8 Ga [i.e., (17, 18, 66, 99, 100)]. If these intercepts were taken as indicative of individual impact-induced thermal events, this would require numerous impacts over the last 2 Ga at the Apollo 11 site. It seems likely that some of these hypothetical impacts would have excavated at least some samples to the surface, leading to more dispersed cosmic ray exposure ages than is observed and evidence for preirradiation in samples other than just group A basalts. This would be inconsistent with the simple exposure age distribution of the basalts.

This surface heating scenario requires that any diffusive loss of $^{40}\text{Ar}^*$ at time prior to 102 Ma be insignificant relative to the apparent loss of $^{40}\text{Ar}^*$ after 102 Ma. This suggests that sample 10020 did not reside at temperatures much in excess of 25°C for any significant duration between ~ 3.7 Ga and ~ 102 Ma.

6.5.5. Model failures and remaining uncertainties. Despite strong evidence in favor of the daytime heating scenario, the observed initial step ages for sample 10020 (~ 1.7 Ga) are significantly older than the initial ages of ~ 0.2 Ga predicted by our surface heating model (and by our 102 Ma impact model). These older initial step ages argue against Ar loss occurring during residence near the lunar surface over the past 102 Ma. They might suggest instead that diffusive loss is associated with a 1.7 Ga event (heating in an ejecta blanket). Under such a scenario, the lower than expected initial $^{38}\text{Ar}_{\text{cos}}/^{37}\text{Ar}_{\text{Ca}}$ values discussed above must reflect inaccuracies in our domain distribution parameters or inferred $^{38}\text{Ar}_{\text{cos}}$ production rates. Alternatively, initial extractions may comprise recoil-implanted $^{37}\text{Ar}_{\text{Ca}}$ degassing from the surface of K-glass domains, possibly derived from adjacent plagioclase and pyroxene grains, which would result in lower than expected $^{38}\text{Ar}_{\text{cos}}/^{37}\text{Ar}_{\text{Ca}}$ values. Moreover, the analyzed fragments of sample 10020 must have been sufficiently shielded from solar heating such that average daytime temperatures did not exceed $\sim 40^\circ\text{C}$, as higher temperatures are expected to cause diffusive loss and younger initial step ages.

If, however, the daytime heating scenario is correct, then the initial step ages must not reflect the last time of significant diffusive loss of $^{40}\text{Ar}^*$ (i.e., they must be anomalously old). Initial step ages may be erroneously old due to (1) the recoil loss of $^{39}\text{Ar}_{\text{K}}$ during irradiation, (2)

concurrent degassing of loosely bound “excess ^{40}Ar ” (e.g., ^{40}Ar within semi-coherent grain boundaries or microfractures), and/or (3) the loss of low initial extraction ages due to heating during irradiation and extraction line bake-out. Evidence for recoil loss of $^{39}\text{Ar}_K$ is manifest in the decrease in high-T step ages that appears to reflect initial pyroxene extractions contaminated by excess ^{39}Ar (i.e., recoil-implanted ^{39}Ar). We are unable to confidently assess the potential role of excess ^{40}Ar in augmenting initial step-ages. Additional experiments on sample 10020 using alternative heating schedules and on similar mare basalts would be productive. Thus the primary uncertainty in distinguishing between these two thermal histories is the reliability of the initial step ages, which largely reflect $^{40}\text{Ar}^*$ and $^{39}\text{Ar}_K$ released from fine-grained K-glass. Given the simplicity and internal consistency of the surface heating model, as well as seemingly plausible explanations for erroneously old initial ages, we postulate that it is the most probable solution.

Figure Captions

Fig. S1. Natural remanent magnetization in mare basalt 10020 subsamples 234c and 234d. Shown is a two-dimensional projection of the NRM vector during AF demagnetization. Solid (open) symbols represent end points of magnetization projected onto the horizontal N'-E' (vertical N'-Z') planes. This coordinate system is not absolutely oriented with respect to the unprimed coordinate system in Fig. 1. Peak fields for selected AF steps are labeled in mT. Arrows denote HC component directions determined from PCA. (A) Subsample 234c. (B) Subsample 234d. (C) Zoom of boxed area in (A).

Fig. S2. Natural remanent magnetization in mare basalt 10020,4F as measured by (20). Shown is a two-dimensional projection of the NRM vector during AF demagnetization. Solid (open) symbols represent end points of magnetization projected onto the horizontal N''-E'' (vertical N''-Z'') planes. The coordinate system is not absolutely oriented with respect to the unprimed or primed coordinate systems in Figs. 1 and S1. Peak fields for selected AF steps are labeled in mT. Arrows denote HC component directions determined from PCA.

Fig. S3. Equal area stereographic projection of NRM components fit to 10020 subsamples 234c and 234d. Black circles denote HC directions for each subsample. Star gives mean direction for HC components for both subsamples, with surrounding ellipse denoting 95% confidence interval on mean direction (not accounting for ~3-5° mutual orientation uncertainty). Grey circles denote LC directions for each subsample.

Fig. S4. Paleointensity experiments on 10020,234b1 (Fig. 1A). See Table S2 for paleointensity values. (A) ARM method, in which AF demagnetization of NRM is plotted as a function of cumulative ARM acquired in laboratory DC bias fields of 50 μ T (squares), 200 μ T (circles), and 600 μ T (triangles). Data points from LC and HC components are colored blue and red, respectively. (B) IRM method, in which cumulative AF demagnetization of NRM is plotted as a function of AF demagnetization of a strong field IRM (for this sample, 130 mT). Data points from LC and HC components are colored blue and red, respectively.

Fig. S5. Recovered paleointensities versus TRM-equivalent applied laboratory field for 10020,234d (circles). Perfect agreement is shown by dashed line of slope 1. Actual paleointensities for HC component of NRM for 234d using the ARM method with 200 μ T and 50 μ T bias fields are shown by horizontal dark blue and light blue lines, respectively.

Fig. S6. Room temperature hysteresis loop measured for 10020,234c. Shown is the sample moment as a function of applied field.

Fig. S7. ARM acquisition experiments on subsample 10020,234b4. Shown is the ARM acquired in a 200 mT AC field as a function of DC bias field. Upper dotted curve is that of highly interacting chiton tooth magnetite and lower dotted curve is non-interacting magnetite in magnetotactic bacteria (101).

Fig. S8. IRM acquisition and demagnetization experiments on subsample 10020,234b4. f_{SIRM} = fraction of IRM remaining/lost. (A) IRM acquisition (light blue points) and AF demagnetization of IRM (purple points). Both curves are normalized to the highest-field IRM value. (B) Derivative of AF demagnetization of IRM (light blue crosses) and of IRM acquisition (purple crosses), with running average given by solid lines.

Fig. S9. AF demagnetization of sample 10020,234d. Shown is the intensity of NRM (red squares) during AF demagnetization compared to that of various forms of laboratory-induced magnetization: ARM acquired in a 85 mT AC field and 0.2 mT DC bias field (yellow circles), IRM acquired in a 200 mT field (black diamonds), and PRM acquired in a field of 0.8 mT at a pressure of 1.8 GPa (blue triangles). (A) Magnetization normalized to initial (undemagnetized) step to emphasize comparison between LC component and laboratory magnetizations. (B) Magnetization normalized to 10 mT AF step to emphasize comparison between HC component and laboratory magnetizations.

Fig. S10. PRM acquisition by sample 10020,234d. Shown is the PRM intensity as a function of applied pressure (0.4, 0.9, 1.4, and 1.8 GPa) acquired in a 0.8 mT field. Empty circles are PRM normalized by the AF 0 mT step and filled circles are normalized by the AF 10 mT step. Solid lines are best fit linear regression to data. Extrapolation yields a maximum estimate of the PRM acquired at 5 GPa (stars) (56).

Fig. S11. VRM experiments on 10020,234c. Sample was stored for nearly 7 days in the Earth's magnetic field ($\sim 50 \mu\text{T}$) and then returned to our shielded room ($< 150 \text{ nT}$) where its moment was semi-continuously measured (white circles). All of the data can be fit well with an exponential curve (black curve) for the moment (in units of Am^2): $\text{moment} = 6.62 \times 10^{-13} \times \exp[0.732 \times \log(\text{time})]$. Later time data [$\log(s) > 3.07$] can be alternatively fit with a line (red): $\text{moment} = S_d \times \log(\text{time}) - 2.51 \times 10^{-11}$, where $S_d = 9.61 \times 10^{-12} \text{ Am}^2/\log(s)$.

Fig. S12. Lunar Reconnaissance Orbiter Camera (LROC) (72) photographs of the Apollo 11 landing site at two different illumination angles. (A) A low illumination angle shows the relatively young sharp-rimmed West Crater and Little West Crater (LROC image NACR00000ADA). (B) High illumination angle shows the distribution of impact ejecta from West Crater that reach to the landing site (LROC image M109080308RE).

Fig. S13. BSEM images of 30 μm thin section 10020,75. (A) Context image showing plagioclase (plag), pyroxene (pyx), ilmenite (ilm), K-rich glass, Fe-Ti-Cr spinel (sp), and cristobalite (cr). Black areas are holes in thin section. Box shows region magnified in (B). (B) Magnified image of K-rich glass and surrounding phases. Blue circles indicate microprobe spots. (C) Calcium (Ca) x-ray map. (D) Potassium (K) x-ray map. (E) Iron (Fe) x-ray map.

Fig. S14. BSEM images of troilite-kamacite assemblages in 30 μm thin section 10020,75. (A) Context image showing several patches of intergrown troilite and kamacite (arrows). Boxes show regions magnified in (B) and (C). (B, C) Troilite enclosing numerous small globules of kamacite. Metal grains are visible down to the spatial resolution limit ($< 1 \mu\text{m}$).

Fig. S15. Photograph of 30 μm thin section 10020,75 in transmitted light, crossed polars. Plagioclase is visible as light gray laths. Pyroxene is large phenocrysts displaying high order interference colors.

Fig. S16. Apparent Ca/K (A) and $^{40}\text{Ar}/^{39}\text{Ar}$ age (B) spectra for two aliquots (c1 and c2) of whole-rock sample 10020,234. Each spectrum is plotted against the cumulative release fraction of ^{39}Ar . Dimensions of boxes indicate ± 1 standard deviation (vertical) and the fraction of ^{39}Ar released (horizontal). Ca/K ratios were calculated from the $^{37}\text{Ar}_{\text{Ca}}/^{39}\text{Ar}_{\text{K}}$ ratio assuming that the relative production ratio for Ca to K is 1:1.96.

Fig. S17. Single-domain models. $^{40}\text{Ar}/^{39}\text{Ar}$ thermochronometry of plagioclase in two aliquots (c1 and c2) of sample 10020,234 using a spherical, one-domain diffusion model. Based on the relatively low apparent Ca/K ratios shown in Fig. S16A, we assume that the first 20 heating steps of each analysis primarily reflect diffusion of Ar from plagioclase (SOM text). (A) Diffusivity as a function of temperature (Arrhenius plot) calculated from both ^{37}Ar (filled symbols) and ^{39}Ar (open symbols) released during these steps; points are diffusion coefficients (D) divided by the square of the effective diffusive length-scale (a) calculated (29) using measured release fractions of each isotope. The line is the model $D(T)/a^2$ obtained from linear regression to the ^{37}Ar data. (B) The observed apparent Ca/K ratios (open symbols; same data as shown in Fig. S16A normalized to the first 20 steps) and the predicted Ca/K ratios at each degassing step (red symbols) when assuming a uniform distribution of Ca and K and the mean apparent Ca/K ratio of each aliquot. (C) Measured and modeled $^{40}\text{Ar}^*/^{39}\text{Ar}$ ratio evolution spectra for each aliquot, normalized as above. $^{40}\text{Ar}^*$ represents radiogenic ^{40}Ar (i.e., corrected for blank, mass discrimination and nuclear reactor-produced interferences to the measured ^{40}Ar signals). Open symbols are the measured $^{40}\text{Ar}^*/^{39}\text{Ar}$ ratios (R) normalized to the mean ratio of the plateau (R_{plateau} ; corresponding to the apparent plateau age = 3700 Ma) with associated uncertainties plotted versus the cumulative ^{37}Ar release fraction. Curves are modeled release spectra calculated for a square pulse of heating from the present mean lunar surface temperature (-25°C) to various constant temperatures for a duration of 1 hour at 1.7 Ga and 102 Ma using a spherical, one-domain model; these models correspond to specific values of Dt/a^2 (Fig. S19). Note that although these simple models successfully predict the observed $^{40}\text{Ar}^*/^{39}\text{Ar}$ spectrum of each sample, they fail to predict the apparent Ca/K spectra shown in panel (B).

Fig. S18. The best-fit values of Dt/a^2 from the spherical diffusion models assuming a uniform K distribution in plagioclase. (A) The reduced chi squared (χ_v^2) fit statistics of modeled $^{40}\text{Ar}/^{39}\text{Ar}$ release spectra [i.e., Fig. S17C] for various model heating events at 1.7 Ga and 102 Ma plotted versus values of $\log(Dt/a^2)$ assuming the ^{37}Ar -based diffusion kinetics shown in Fig. S17A; four example model results are shown in Fig. S17C. The best-fit value of Dt/a^2 for each model heating time is identified at the minimum χ_v^2 value; points indicate explicitly modeled conditions, and curves are polynomial fits to the χ_v^2 values used to identify the minima. (B) Duration-temperature constraints on possible thermal excursions at 1.7 Ga and 102 Ma experienced by sample 10020. The solution sets of duration and temperature (t - T) combinations are shown as curves of constant Dt/a^2 . Each curve indicates the permissible t - T combinations at

1.7 Ga and 102 Ma that would best predict the observed $^{40}\text{Ar}/^{39}\text{Ar}$ spectra shown in Fig. S17C under the spherical geometry assumption.

Fig. S19. K/Ca zonation models. $^{40}\text{Ar}/^{39}\text{Ar}$ thermochronometry of plagioclase in aliquot 234c1 using a spherical, one-domain diffusion model and a non-uniform distribution of K. Based on the apparent increase in Ca/K ratios of the initial 12 steps shown in Fig. S16A, here we assume that the outer edge of the effective diffusion domain has higher K concentration than the interior (SOM text). (A) Diffusivity as a function of temperature (i.e., Arrhenius plot) calculated from both ^{37}Ar (triangles) and ^{39}Ar (squares) released during the first 20 heating steps; points are diffusion coefficients (D) divided by the square of the effective diffusive length-scale (a) calculated (29) using measured release fractions of each isotope. The blue and green curves represent predicted values of D/a^2 calculated for the heating schedule of the analysis and assuming from a uniform Ca (i.e., ^{37}Ar) distribution and enriched K (i.e., ^{39}Ar) at the domain edge. (B) The observed apparent Ca/K ratios (open symbols) and the predicted Ca/K ratios at each degassing step (red symbols) assuming K/Ca zonation. (C) Measured and modeled $^{40}\text{Ar}^*/^{39}\text{Ar}$ ratio evolution spectra for aliquot 234c1, normalized as in Fig. S17. Shown as colored steps are the zonation model release spectra for a heating event at 1.3 Ga from the present mean lunar surface temperature (-25°C) to various constant temperatures lasting 3.17 ka (10^{11} s). Note that unlike the models shown in Fig. S17, the zonation models successfully predict the apparent Ca/K spectra shown in panel (B).

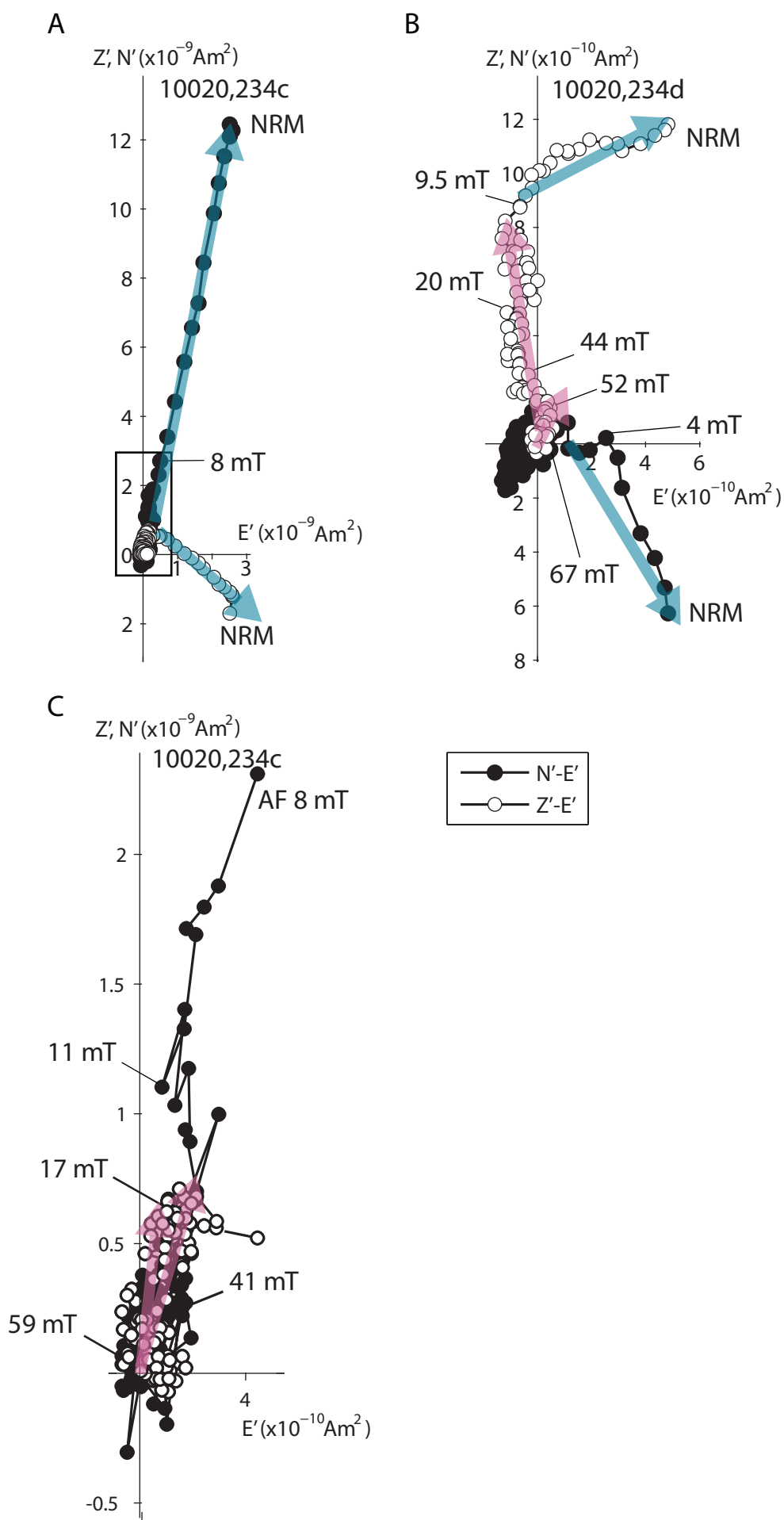
Fig. S20. Multiple-phase, multiple diffusion domain (MP-MDD) models. $^{40}\text{Ar}/^{39}\text{Ar}$ thermochronometry of K-glass and plagioclase in 10020,234c1 using MDD model. (A) Diffusivity as a function of temperature (i.e., Arrhenius plot) calculated from both ^{37}Ar (triangles) and ^{39}Ar (squares) released during the first 20 heating steps; points are diffusion coefficients (D) divided by the square of the effective diffusive length-scale (a) calculated (29) using measured release fractions of each isotope. The blue and green curves represent the multiple-domain model fit to the ^{39}Ar - and ^{37}Ar -based diffusion coefficients, respectively, for the heating schedule of the analysis using the 4 specified domain sizes and gas fractions listed in Table S8. The grey lines indicate the input diffusion kinetics of each of the four model domains. (B) The observed apparent Ca/K ratios (open symbols) and the predicted Ca/K ratios at each degassing step (red symbols) assuming the MDD parameters given in Table S8. (C) Measured and modeled $^{40}\text{Ar}^*/^{39}\text{Ar}$ ratio evolution spectra for aliquot 234c1, normalized as in Fig. S17. Shown as colored steps are the MDD model release spectra for a heating event at 1.3 Ga from the present mean lunar surface temperature (-25°C) to various constant temperatures lasting 3.17 ka (10^{11} s). Note that unlike the models shown in Fig. S17, the MDD models successfully predict the apparent Ca/K spectra shown in (B).

Fig. S21. Relationship between $\ln(r/r_o)$ (the difference between the natural logarithm of a given D/a^2 value and that expected from the low-temperature Arrhenius relationship) and the cumulative release fraction of ^{39}Ar (A) and ^{37}Ar (B). The exhaustion of a domain or onset of significant degassing from a larger domain appears as a segment of positive slope on a $\ln(r/r_o)$ plot (89). Dashed lines indicate the fraction of gas (Φ_{X-Y}) contained within the smallest domains.

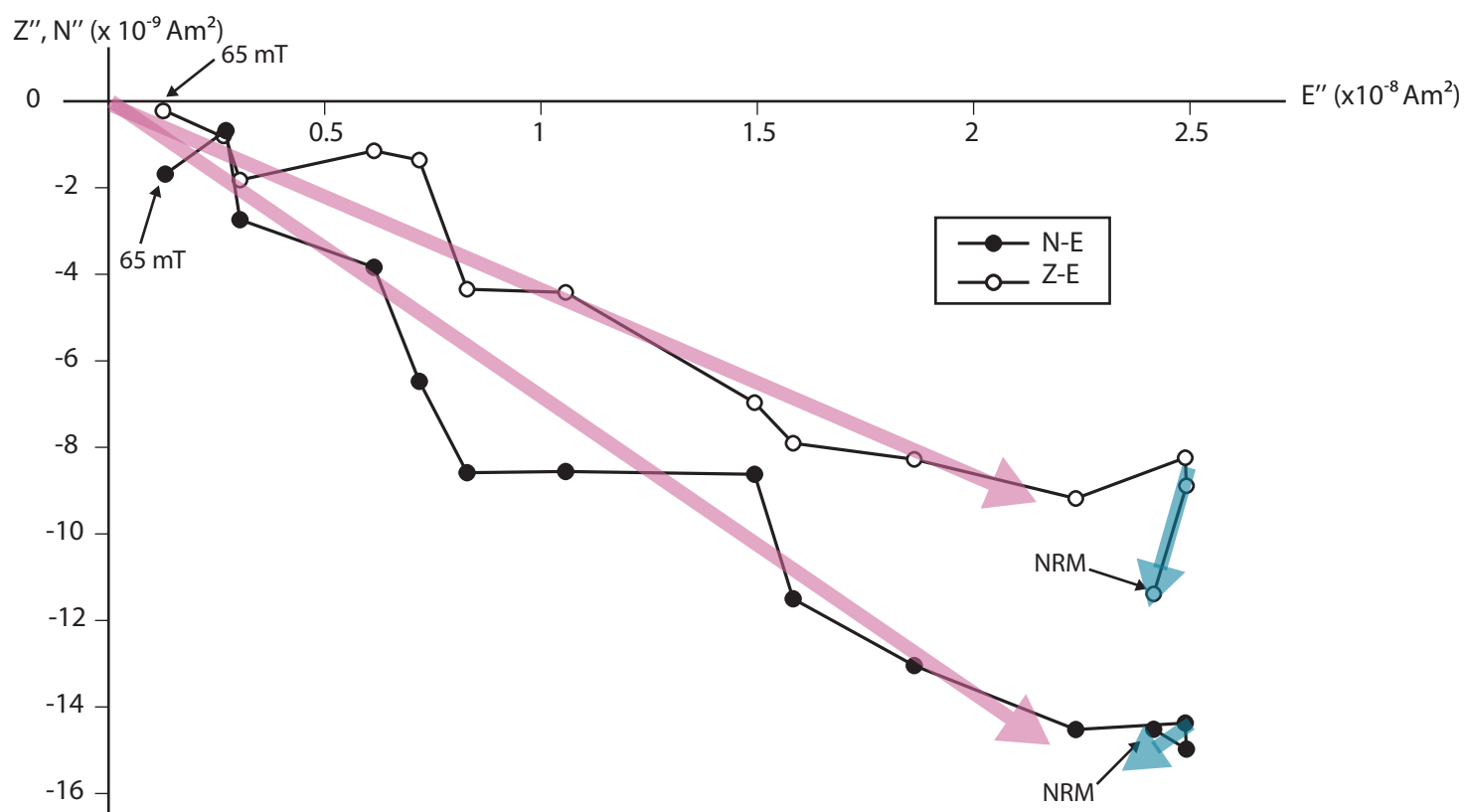
Fig. S22. Summary of thermal constraints using the single-domain, multiple diffusion domain, and cosmogenic ^{38}Ar diffusion models. The permissible duration and temperature combinations are shown for possible thermal excursions experienced by sample 10020,234 at various points in time. The solid and dashed curves (without points), equivalent to those shown in Fig. S18B, determined using the single-domain model. The solid curves (with points) are permissible conditions at 1.7 Ga, 1.3 Ga and 102 Ma that would best predict the observed $^{40}\text{Ar}^*/^{39}\text{Ar}$ spectrum using the MDD model in Fig. S20; points indicate the best-fit conditions of explicitly-calculated durations (e.g., Fig. S23). The square is the best-fit solution for production and diffusion of cosmogenic ^{38}Ar as shown in Fig. S24. The red curve predicts residence temperature of a 6 m-thick ejecta blanket emplaced at 1.7 Ma. Solar heating since ~102 Ma provides an internally consistent prediction of the entire Ar dataset, thereby precluding significantly elevated temperature at earlier points in time.

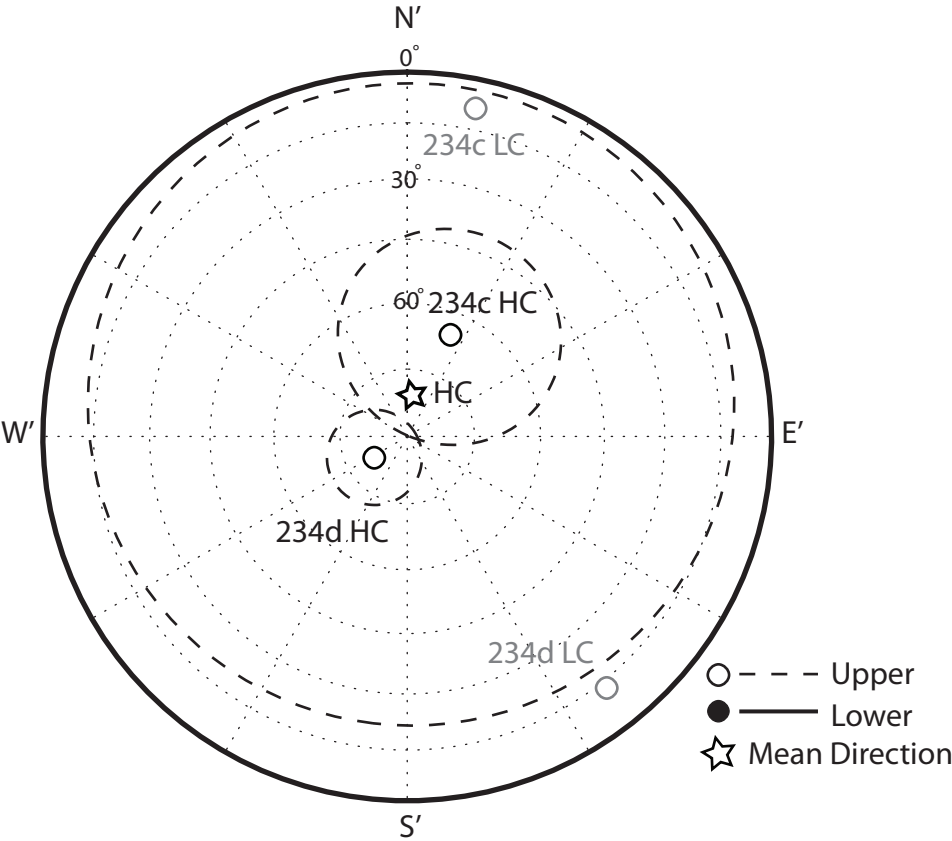
Fig. S23. The best-fit values of temperature (T) for different model heating durations from the MDD model. (A-D) The reduced chi squared (χ_v^2) fit statistics of modeled $^{40}\text{Ar}/^{39}\text{Ar}$ release spectra (i.e., Fig. S17C) for model heating durations of 100s (A), 10^4 s (B), 10^7 s (C), and 10^{11} s (D) plotted versus the temperature of each event assuming the MDD model parameters shown in Fig. S20 and Table S8. Model heating events were calculated at 1.7 Ga, 1.3 Ga, and 102 Ma; fit statistics were calculated in comparison to the 10020,234c1 dataset. The best-fit value of T for each model heating time is identified at the minimum χ_v^2 value; points indicate explicitly modeled conditions, and curves are polynomial fits to the χ_v^2 values used to identify the minima in χ_v^2 .

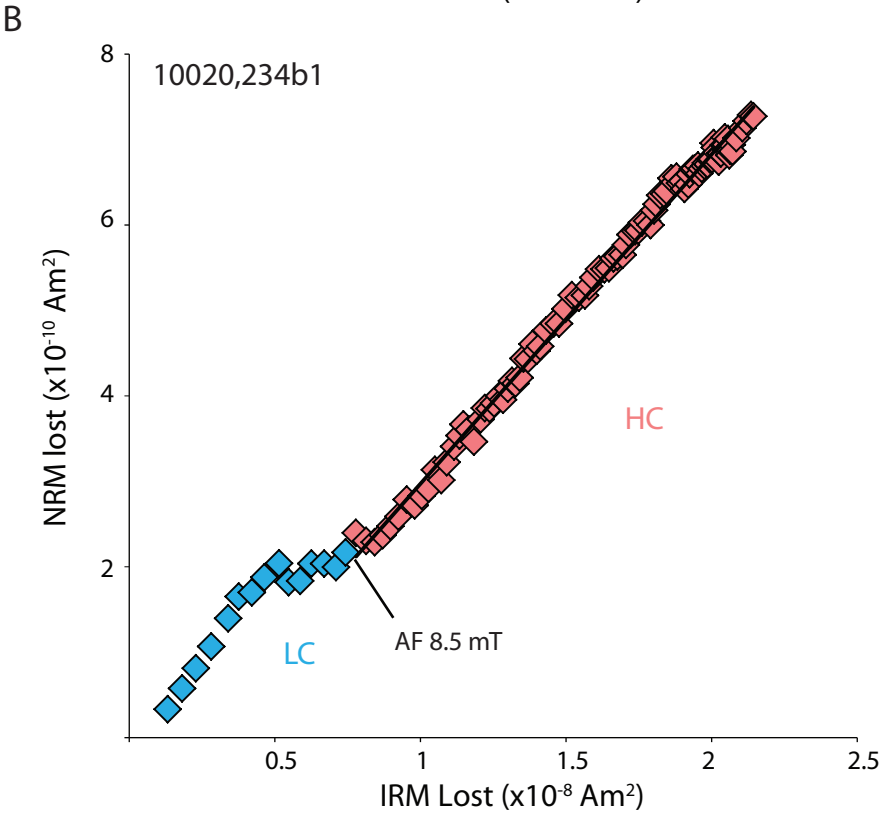
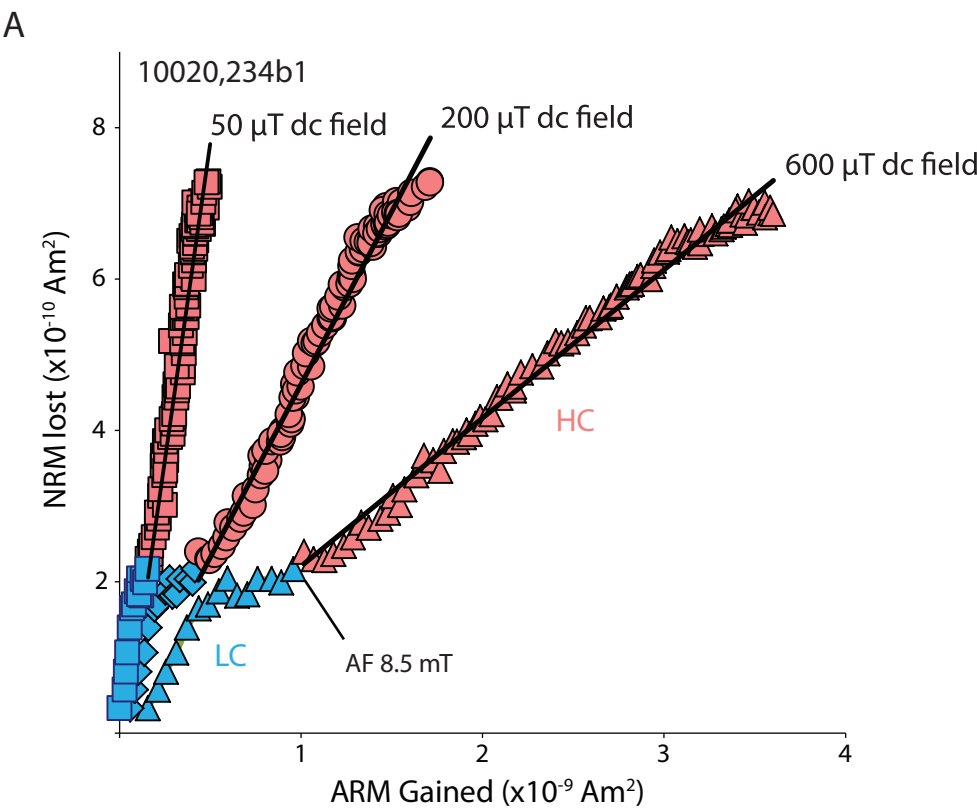
Fig. S24. The predicted effects of solar heating at the lunar surface using the MDD model. (A) The production and diffusion of cosmogenic ^{38}Ar . Shown as grey squares are the observed $^{38}\text{Ar}/^{37}\text{Ar}$ ratios with ± 1 standard deviation, plotted against the cumulative release fraction of ^{37}Ar (note the log scale). In this case, the ^{38}Ar is cosmogenic and was produced in-situ while sample 10020 was exposed at the surface of the moon. Based on the observed concentrations of Ca in the plagioclase and element-specific production rates of (84), the apparent plateau in the plagioclase $^{38}\text{Ar}/^{37}\text{Ar}$ ratios (inset) corresponds to an exposure age of ~102 Ma (Table S7). The colored steps are model release spectra calculated using the MDD model parameters shown Table S8 and for the production and diffusion of cosmogenic ^{38}Ar held at various constant effective temperatures ranging from 50 to 110°C due to solar heating during the last 102 Ma (i.e., cosmogenic ^{38}Ar is produced continuously over this duration, while diffusion occurs only half of this period during elevated temperatures due to incident solar radiation). (B) The diffusion of radiogenic ^{40}Ar due to solar heating. (C) Reduced chi squared (χ_v^2) statistics of each fit, identifying 75-80 °C as the best-fit temperature.

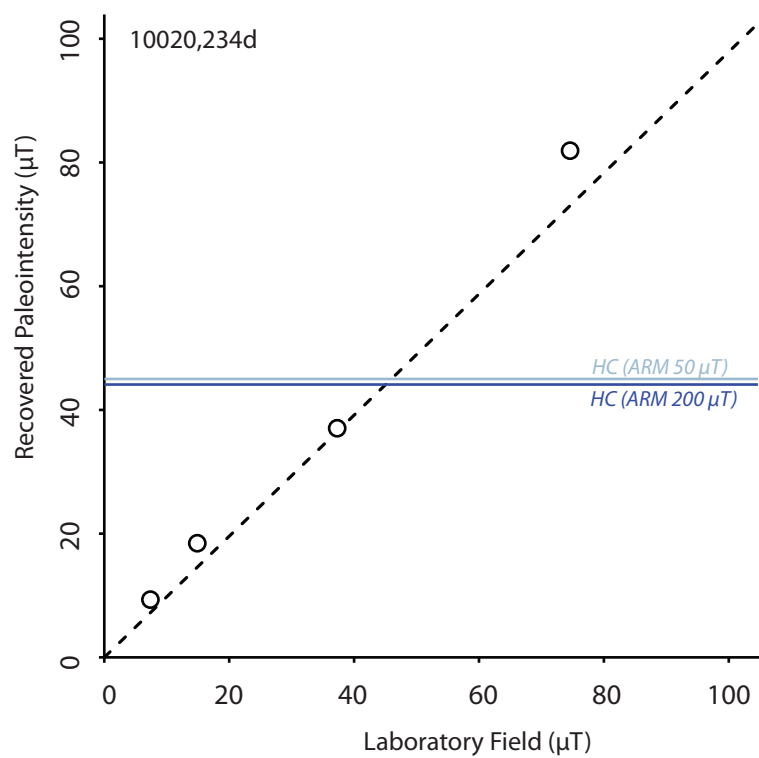


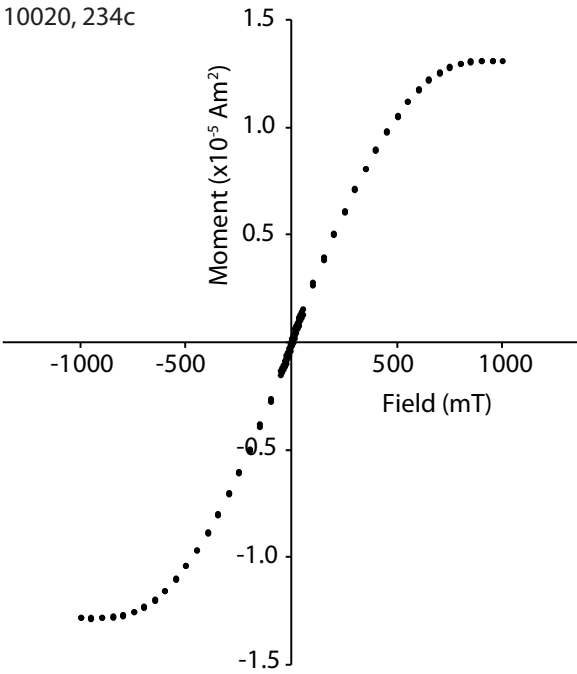
A Long-Lived Lunar Core Dynamo, 2011
Fig. S2

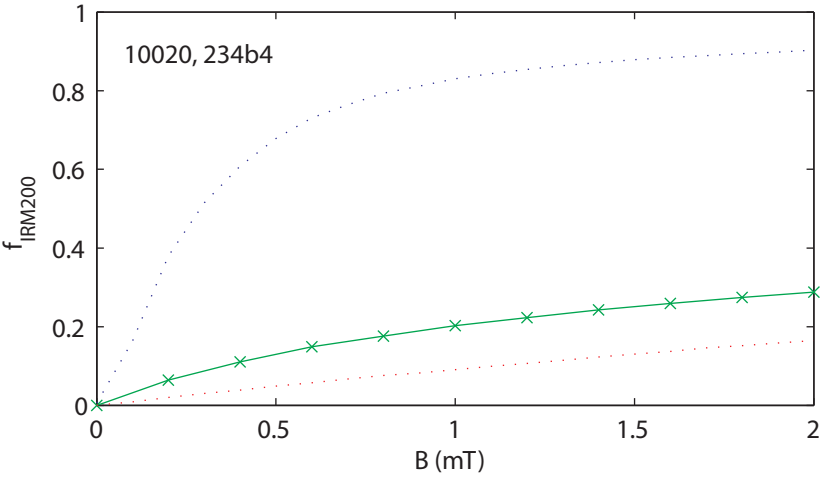




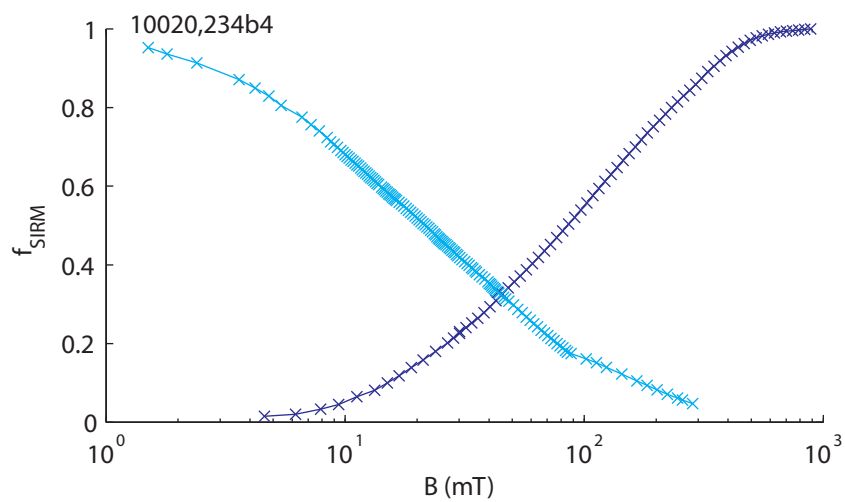




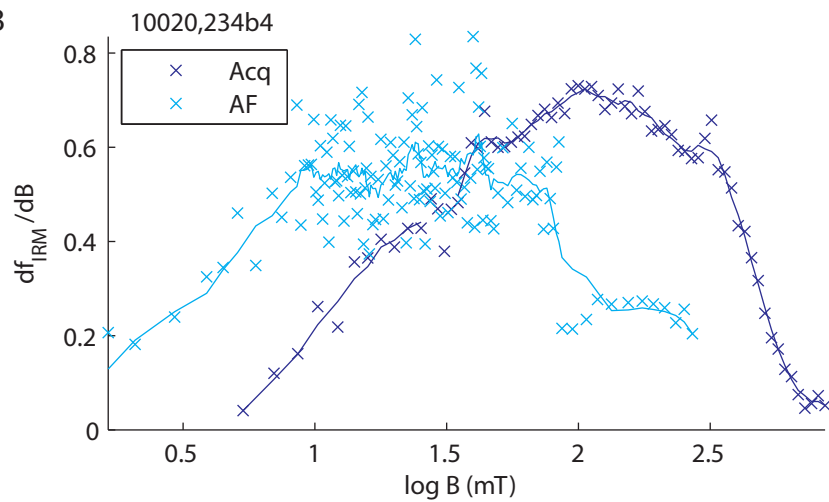


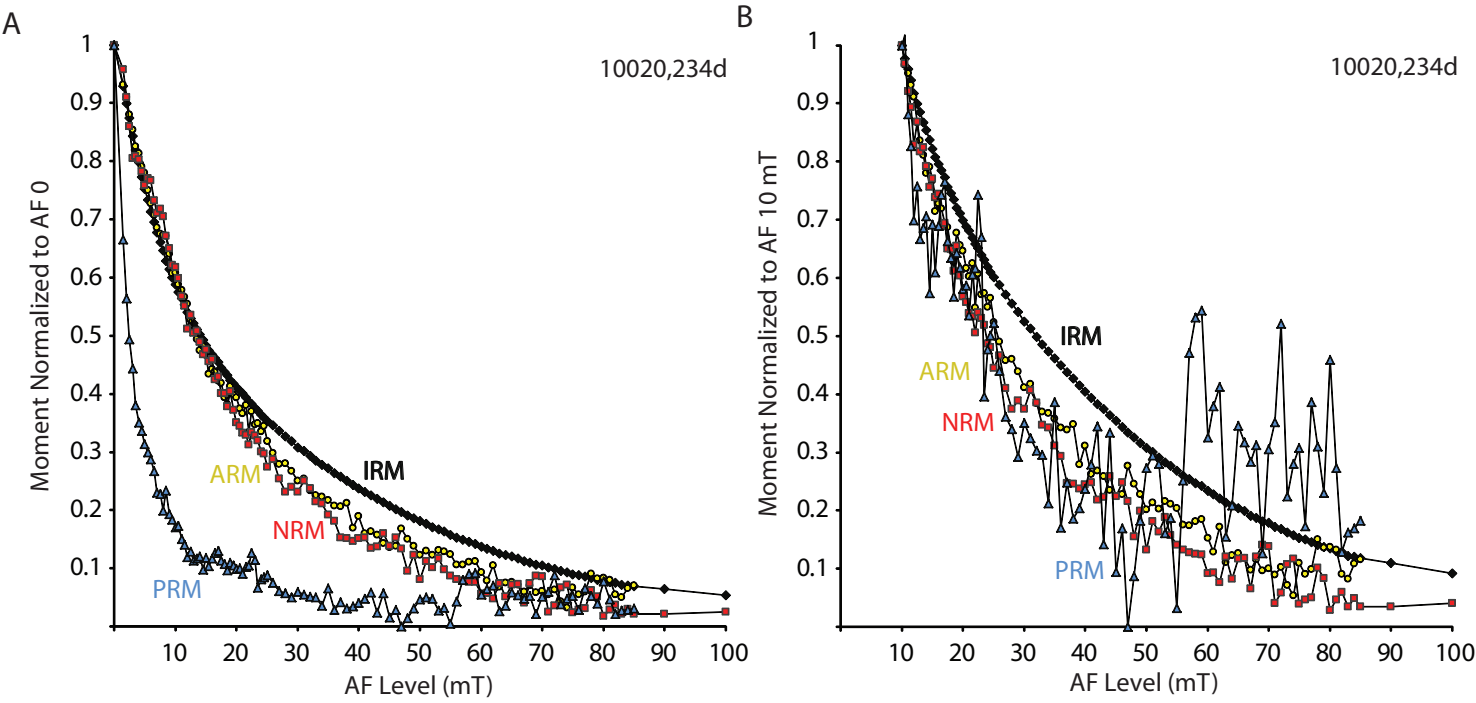


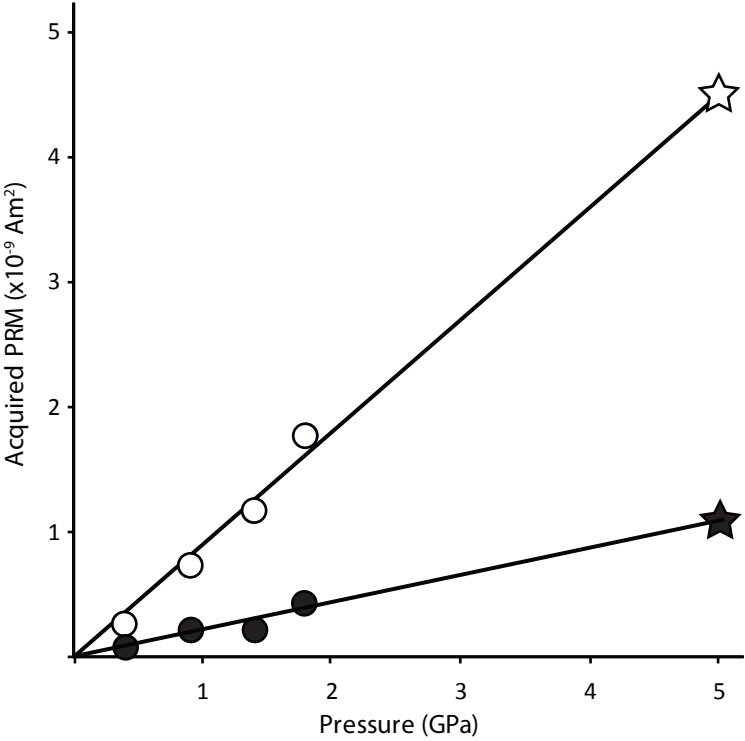
A

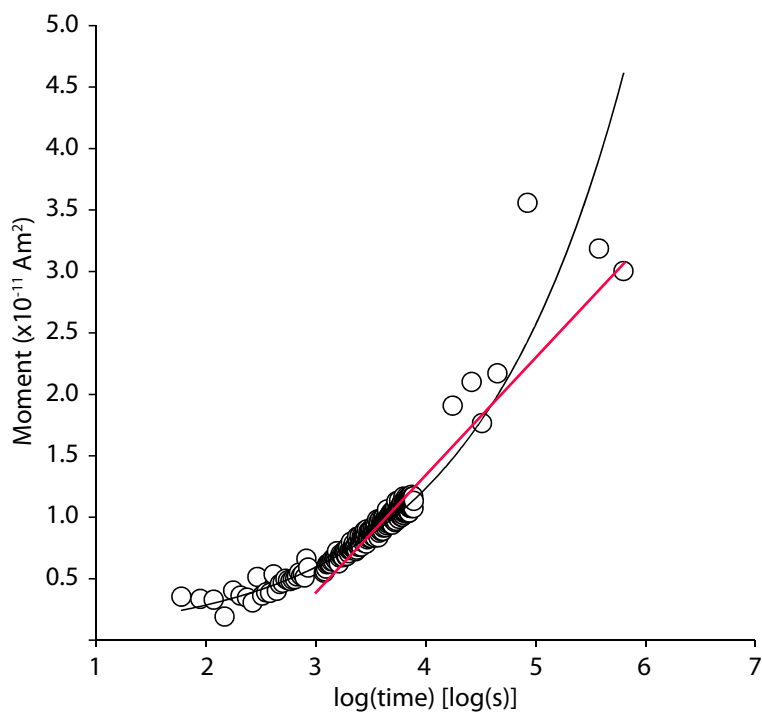


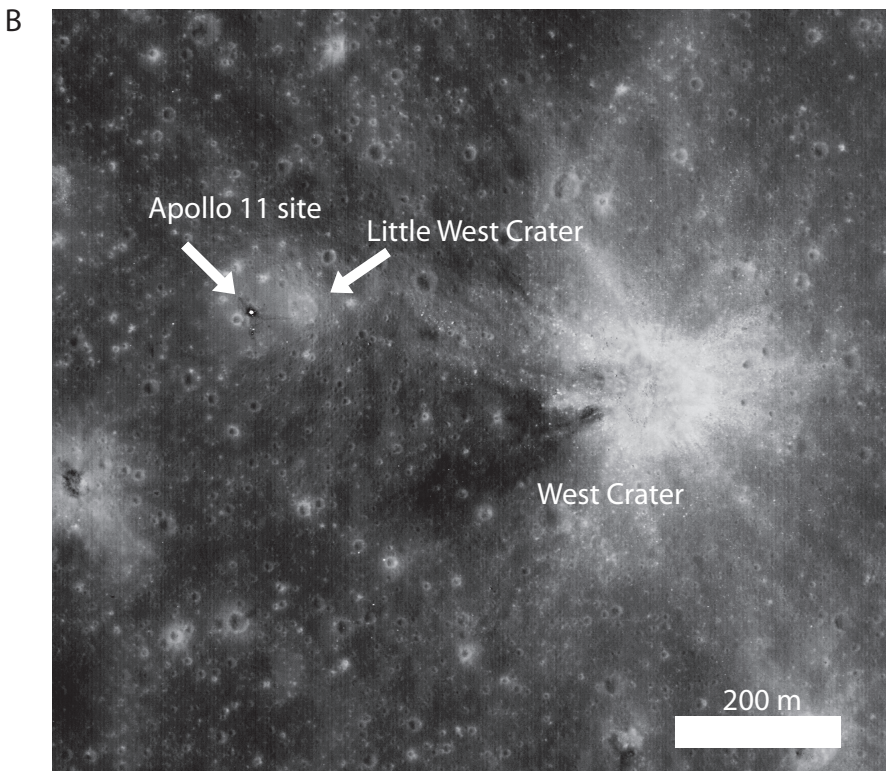
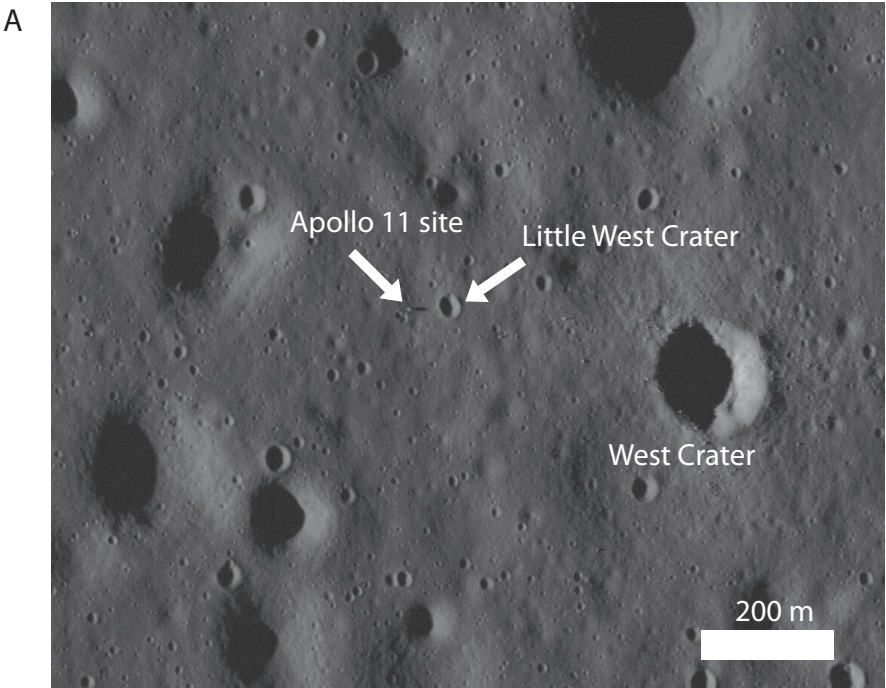
B

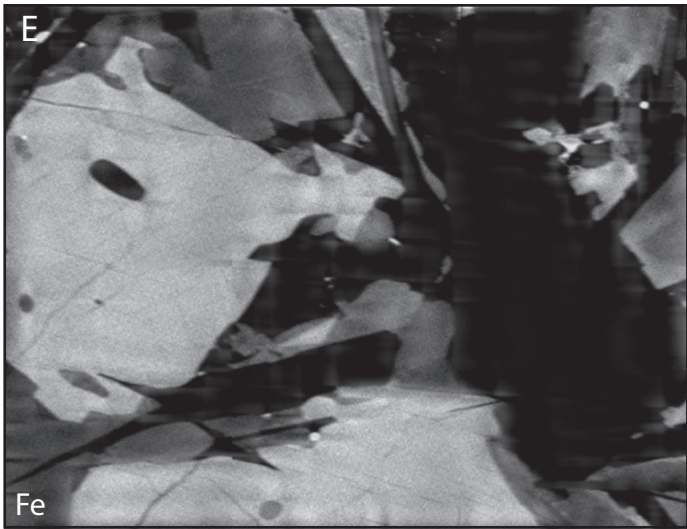
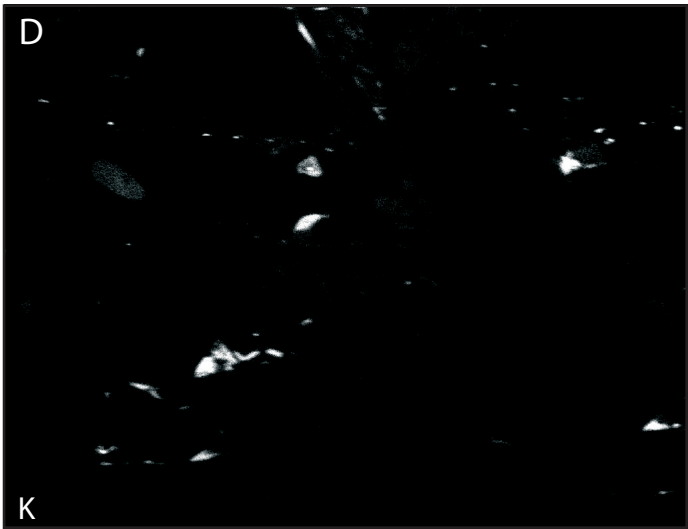
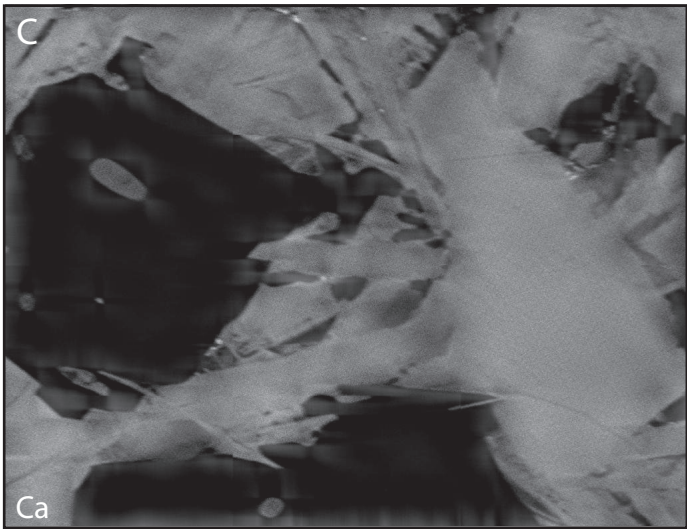
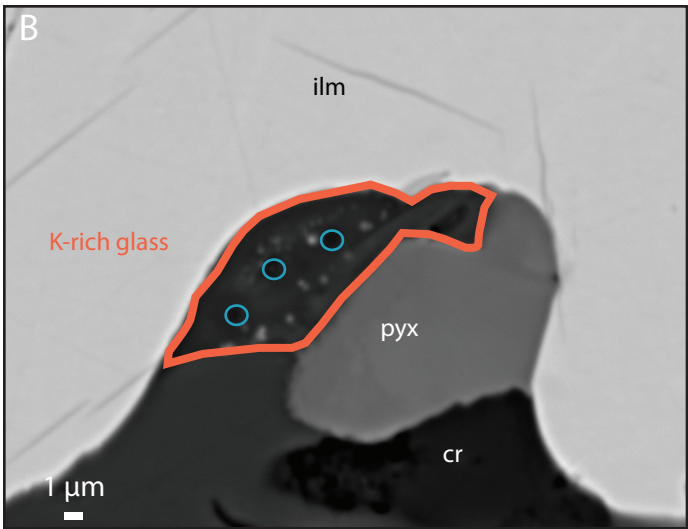
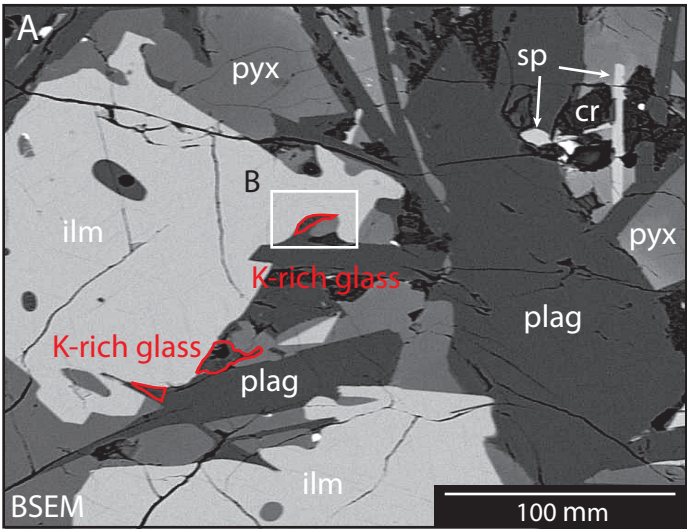


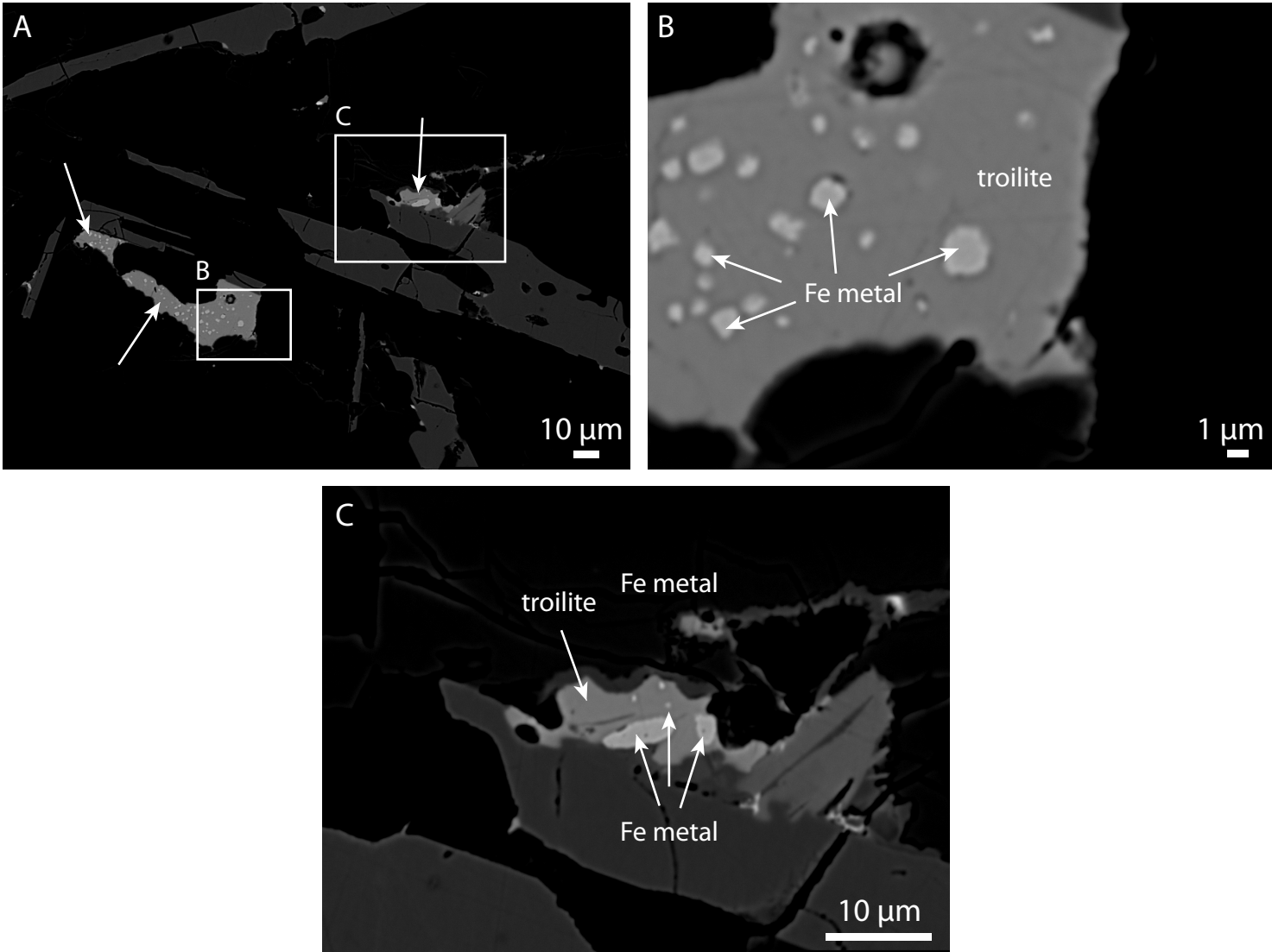


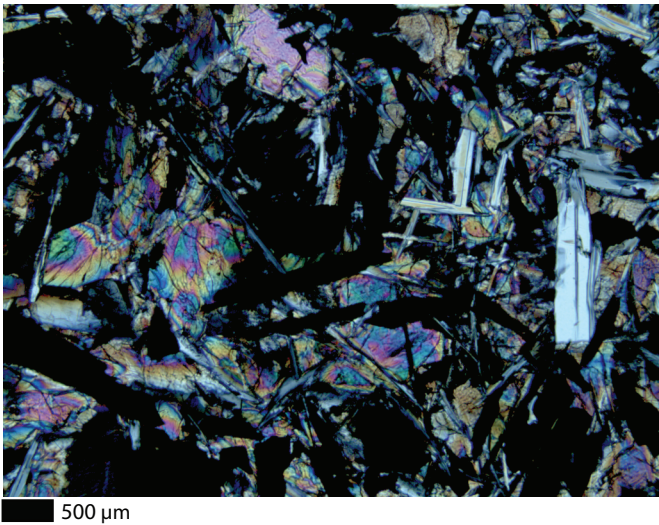


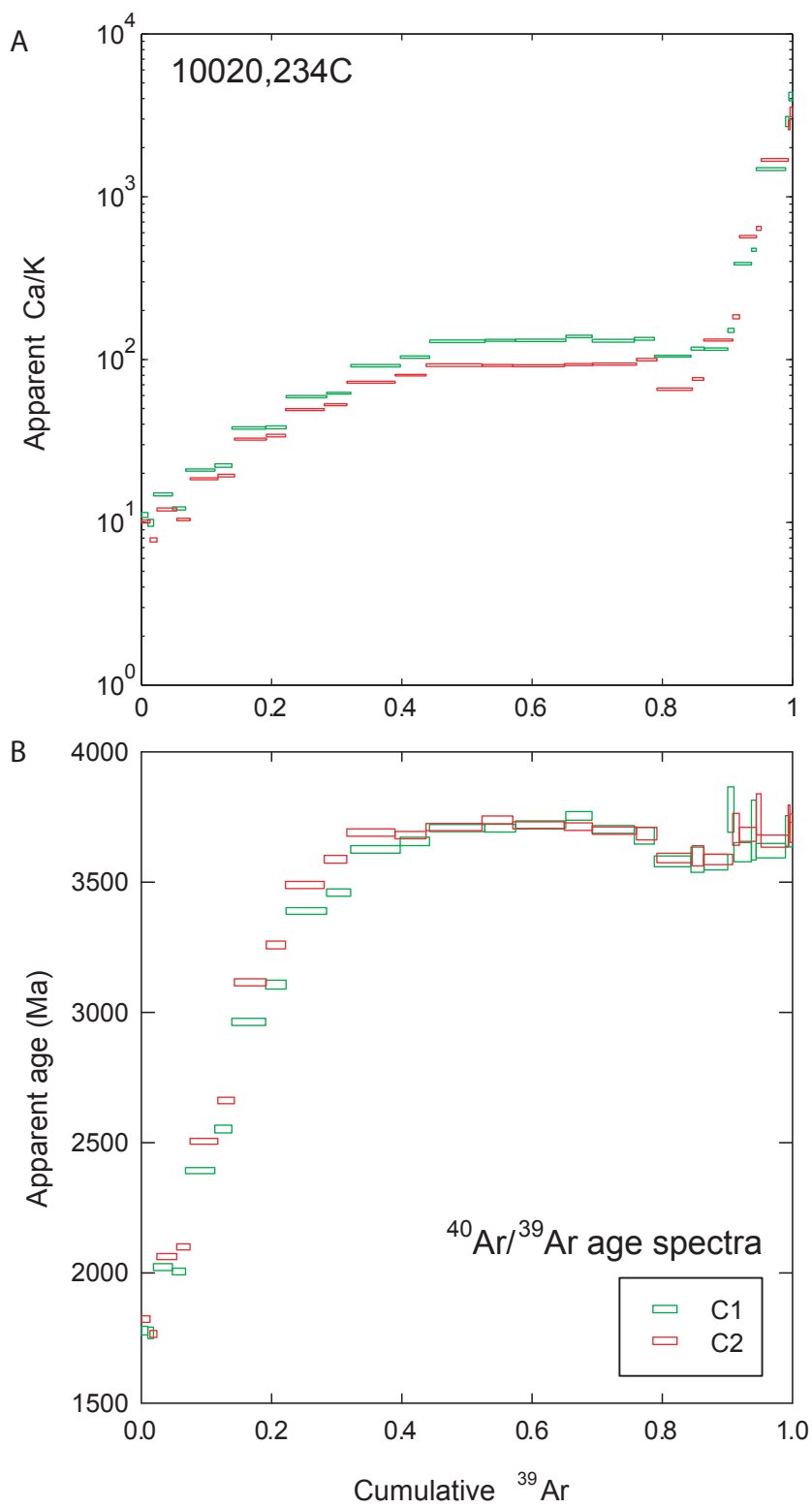


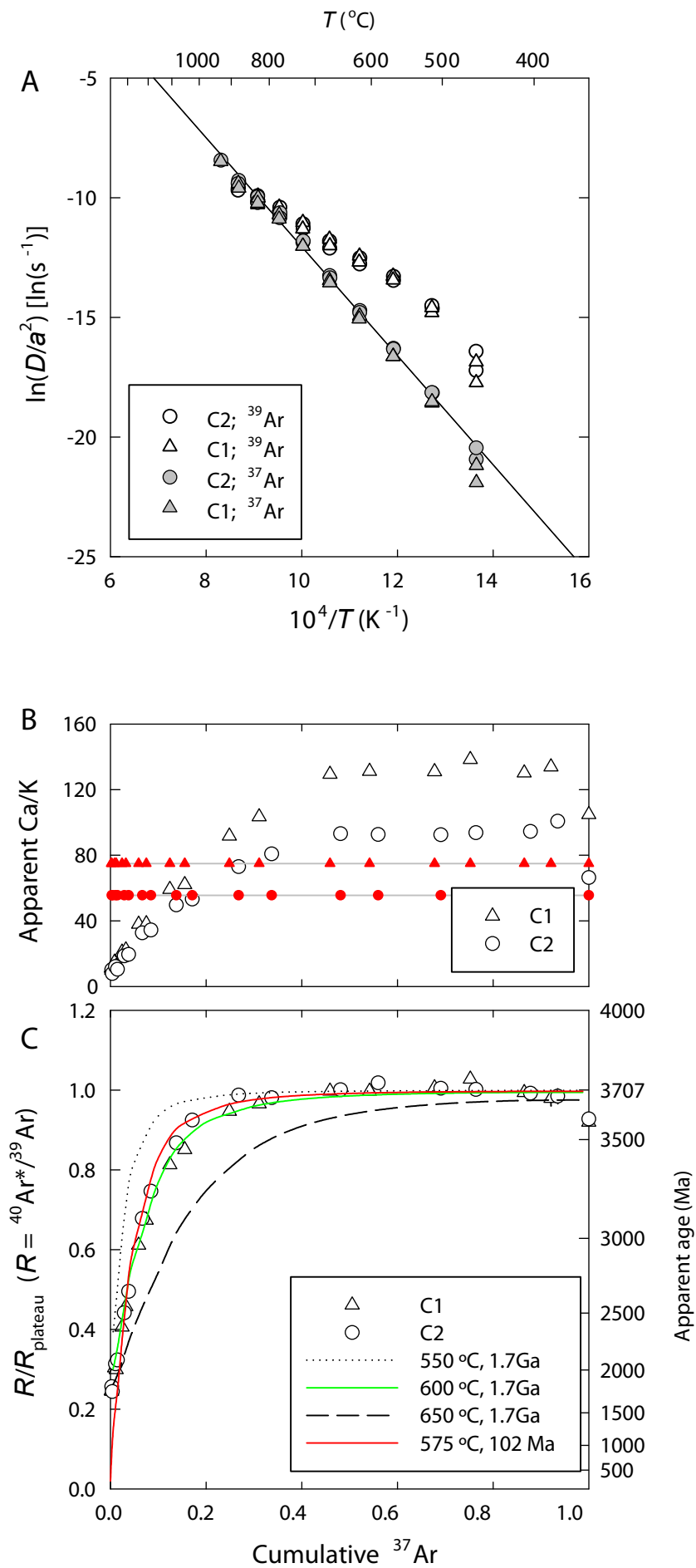


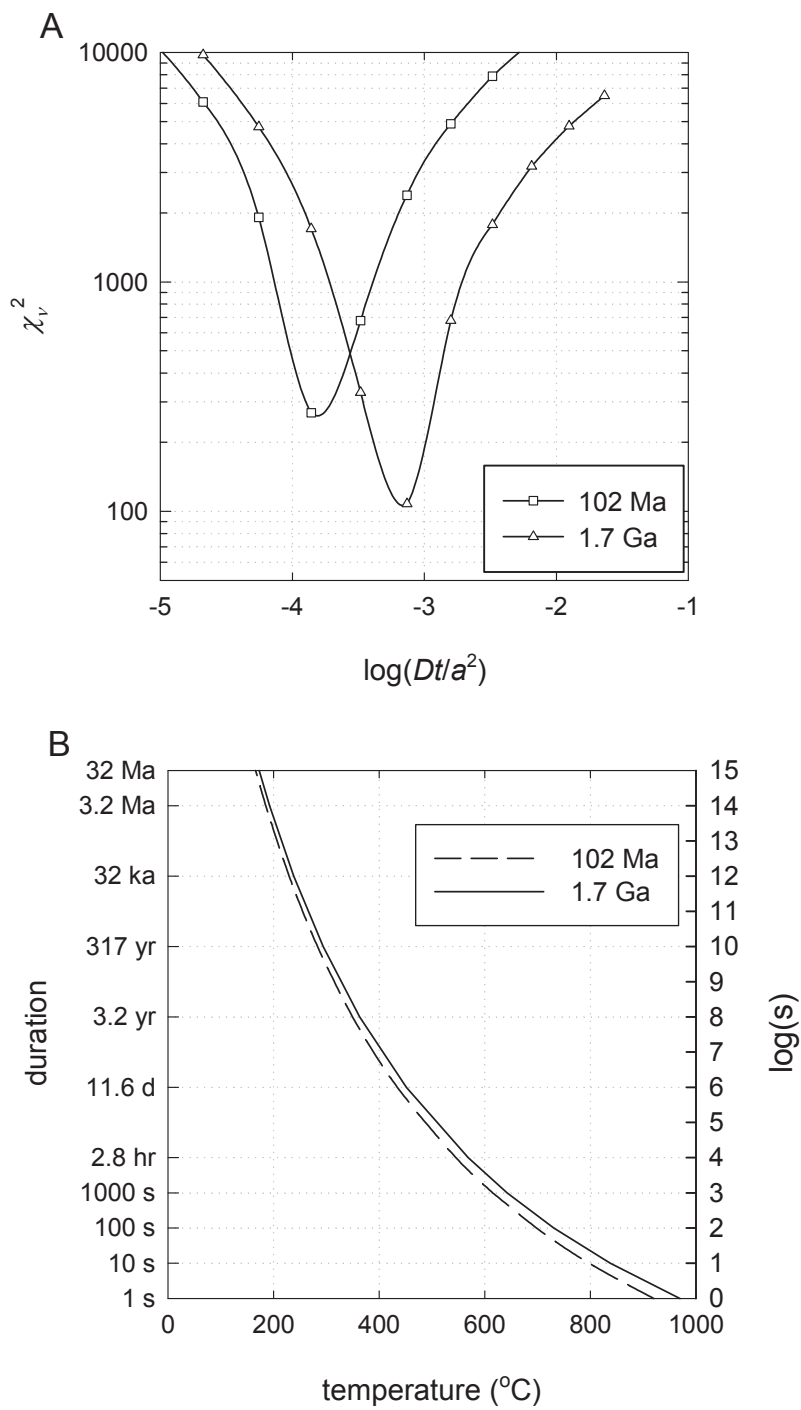


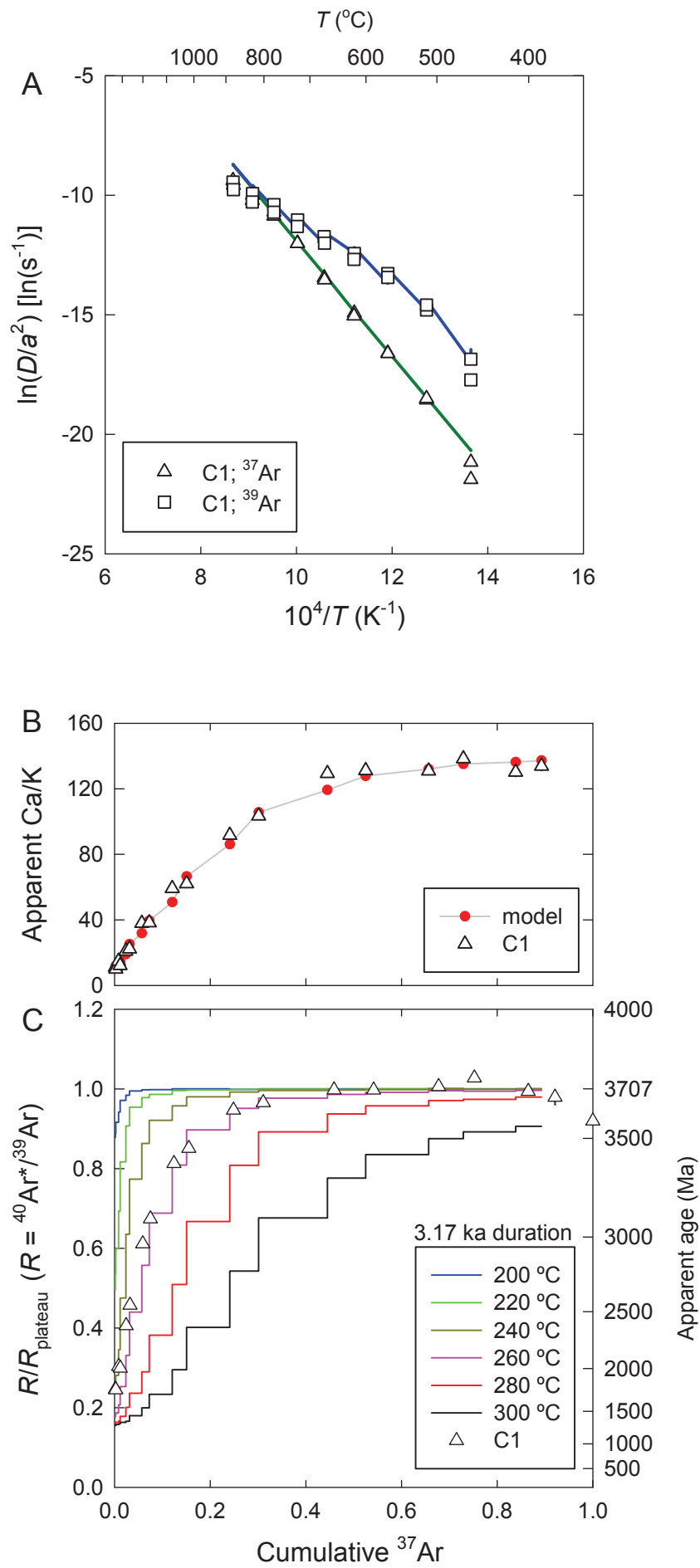


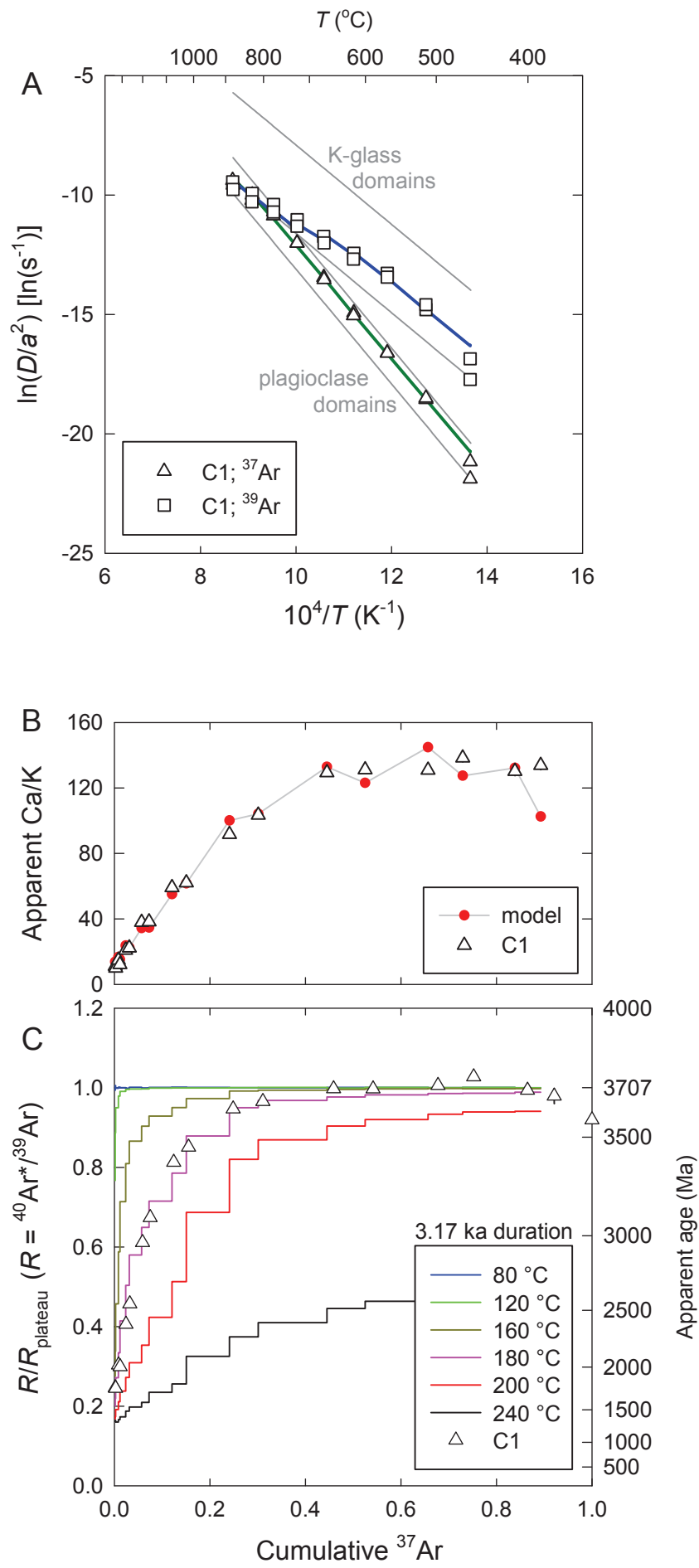


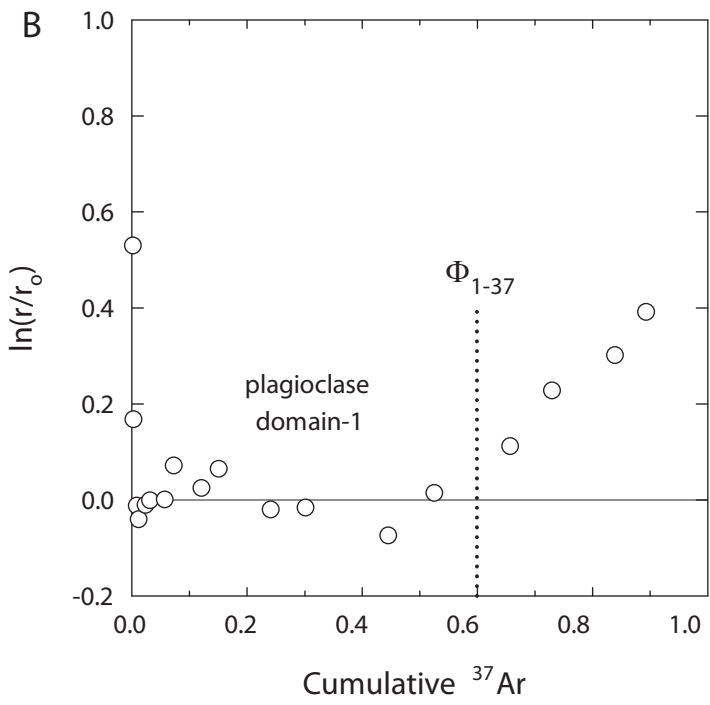
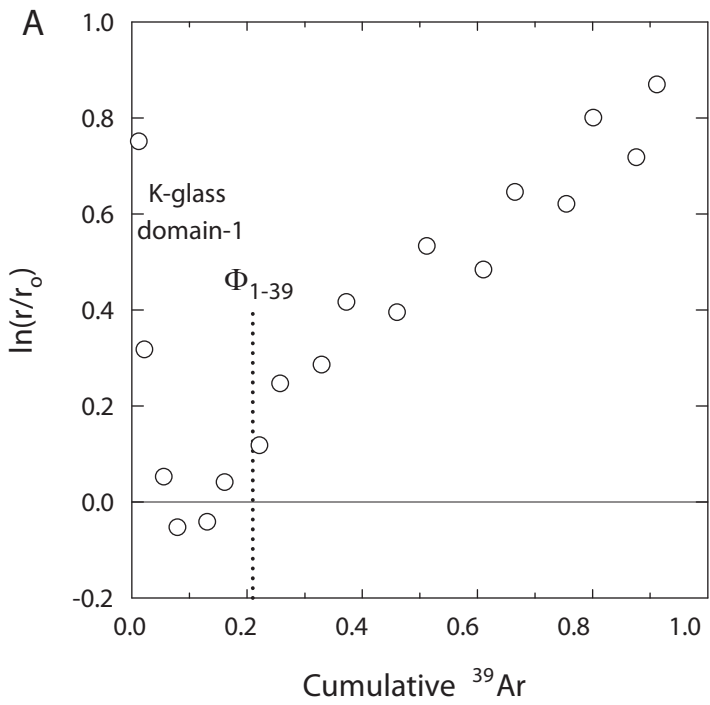


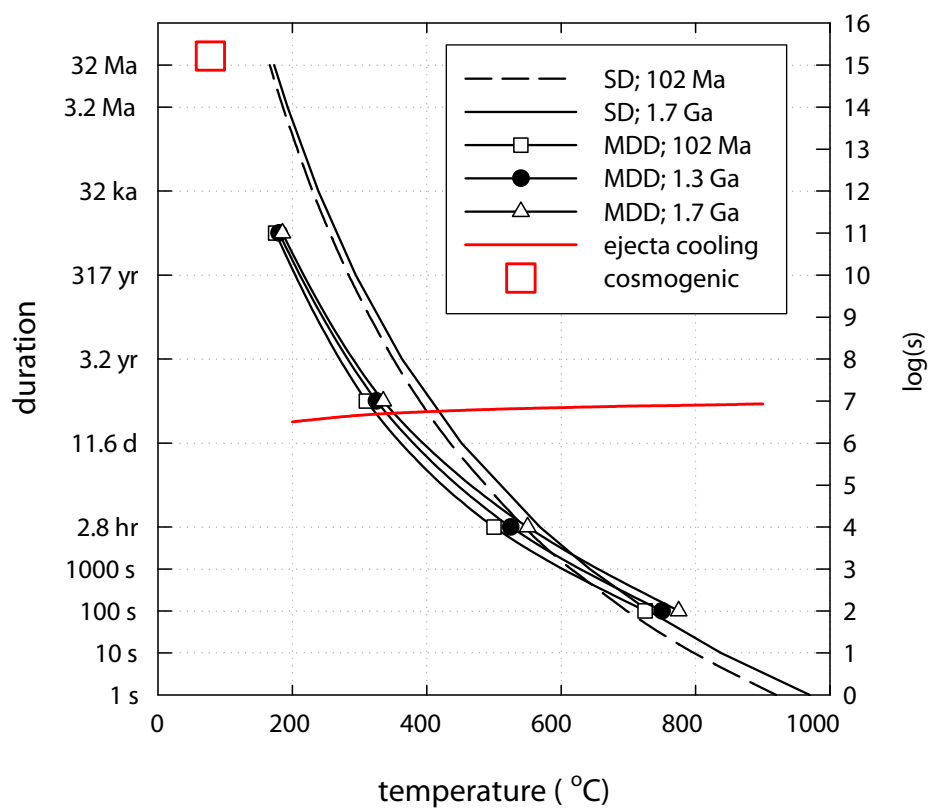


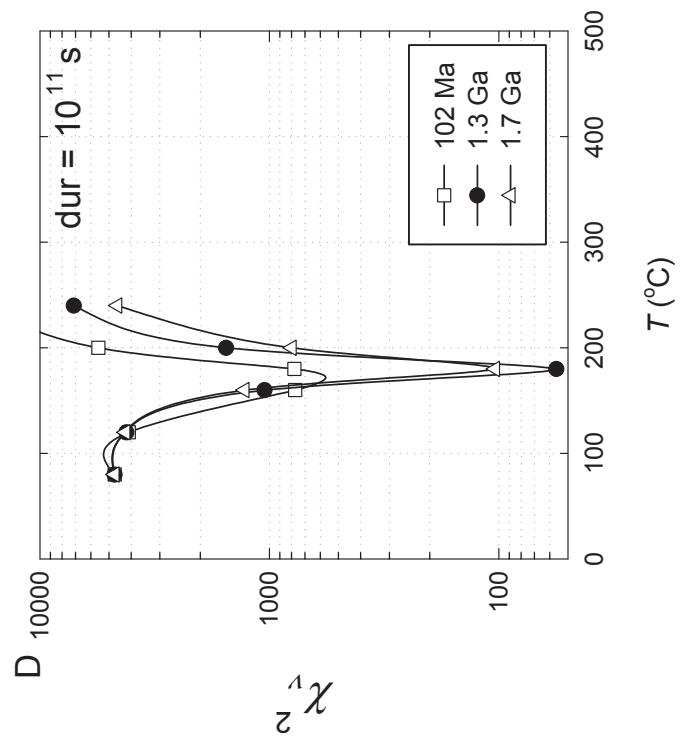
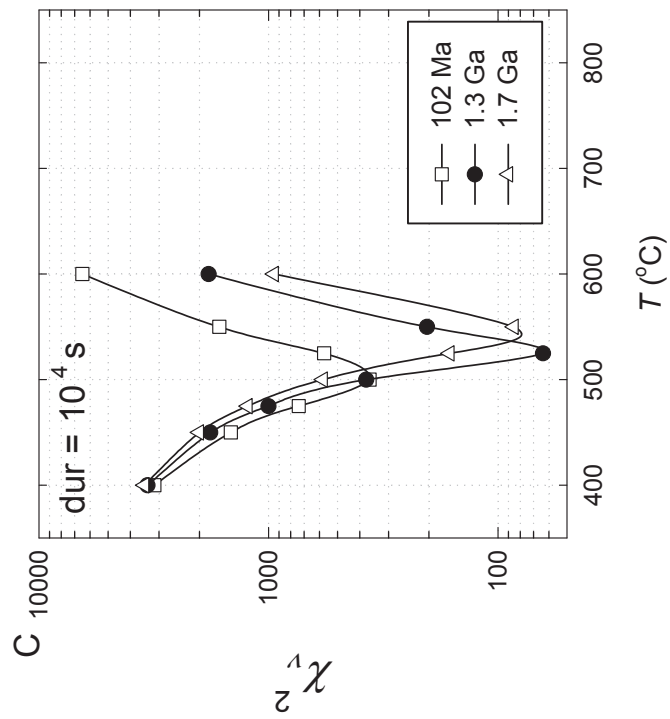
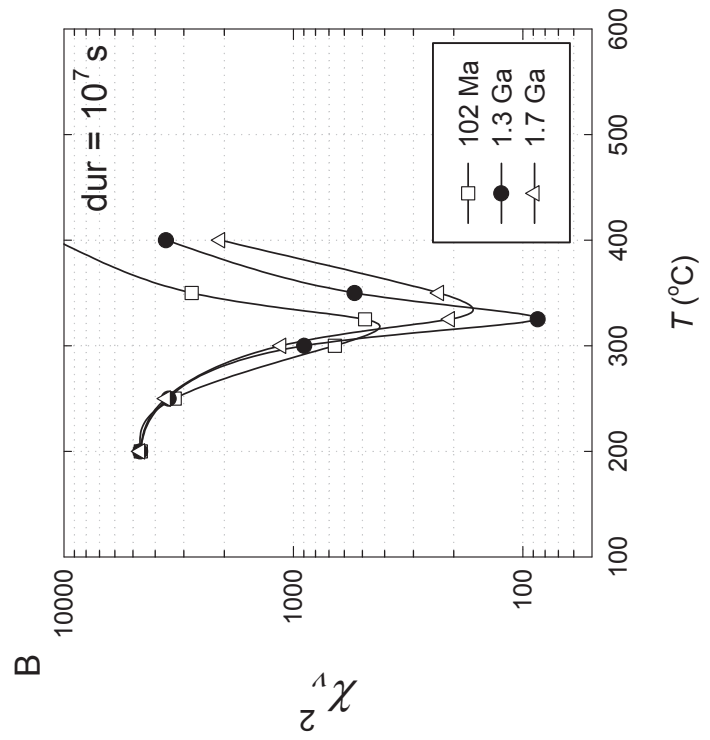
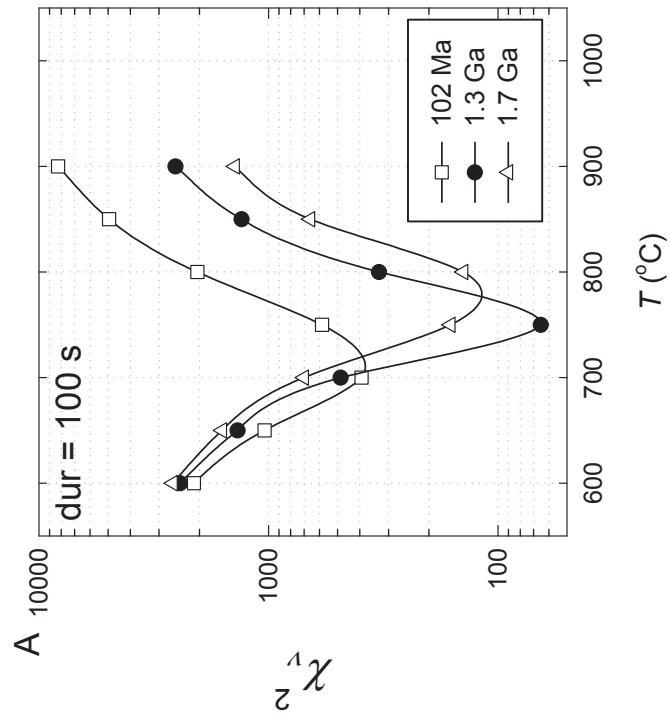


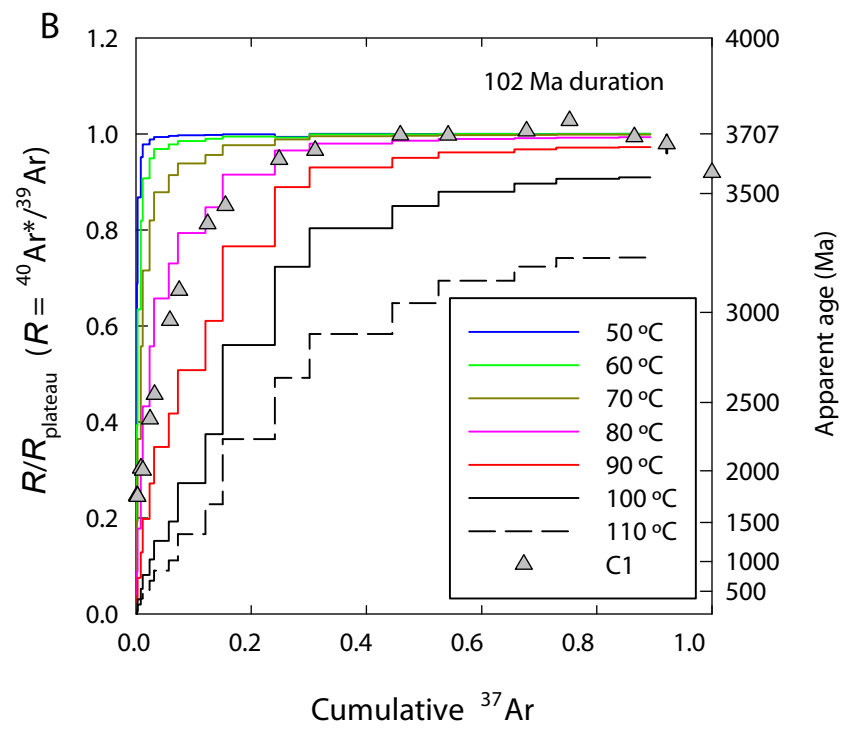
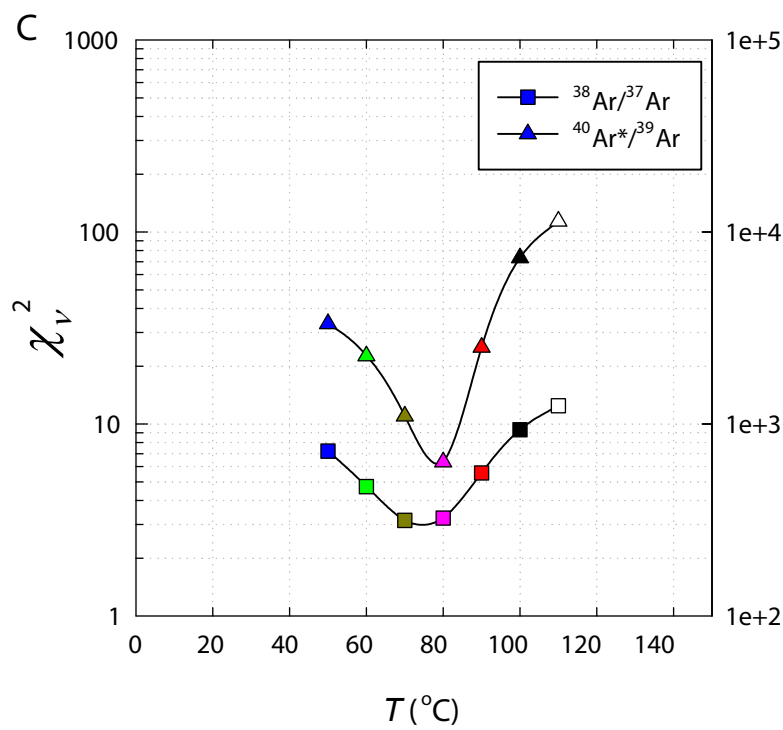
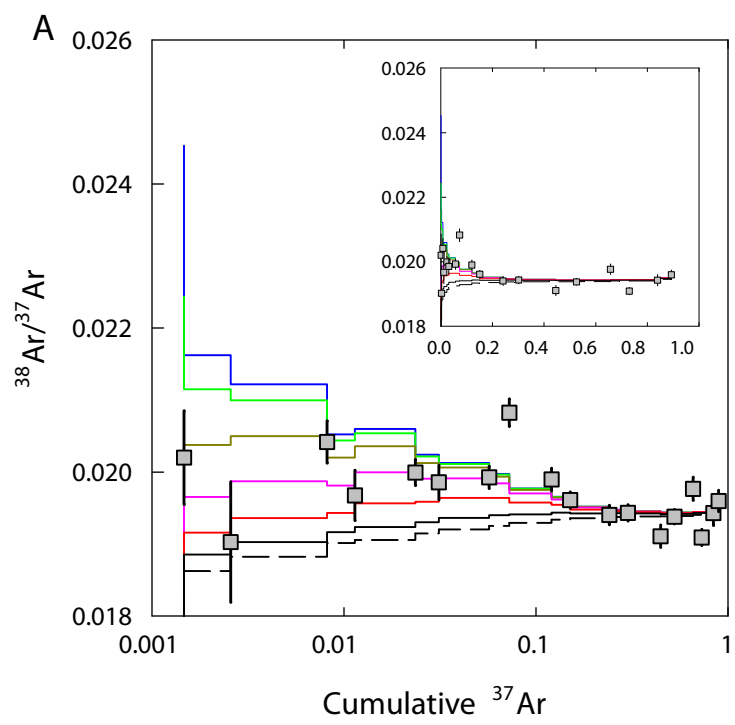












Tables

Table S1a. Summary of LC and HC components for subsamples from 10020,234 obtained with principal component analysis.

Sample, Component	Mass (mg)	AF range (mT)	Type	Dec., Inc. (°)	MAD (°)	dANG (°)	N_s
234b1	47.7						
LC		NRM-8.5	L	66.6, -1.9	9.7		16
HC		9.0-110.0	AL	243.9, 14.9	4.5/4.5	7.1	96
234b2	48.6						
LC		NRM-6.0	L	74.1, -10.3	12.9		11
HC		8.5-260.0	AL	243.5, 10.3	3.9/5.5	4.2	104
234b4	39.6						
LC		NRM-12.0	C	119.7, 74.8	4.3		23
HC		12.5-85.0	AL	251.8, 14.6	8.2/11.3	8.4	86
234c	155.6						
LC		NRM-17.0	L	11.8, 8.8	2.0		33
HC		17.5-66.0	AL	23.0, -65.2	24.6/40.8	13.3	57
234d	119.1						
LC		NRM-9.5	L	141.6, -13.0	15.0		18
HC		10.0-81.0	AL	237.4, -81.3	10.6/14.5	10	81

Note: Subsamples b1, b2, and b4 are mutually oriented. Subsamples c and d are also mutually oriented, but are derived from a chip not oriented with respect to the parent sample. The first column gives the subsample name and component name; the second column gives the subsample mass; the third column gives the range of AF steps used for the fit; the fourth column gives the fit type (L = line; AL = line anchored to the origin; C = great circle fit); the fifth column gives the declination and inclination of the fit direction (for line fits) or great circle pole (for circle fits); the sixth column gives the maximum angular deviation (MAD) of the component forced through the origin/not forced through the origin; the seventh column gives the deviation angle (dANG); and the eighth column gives the number of AF steps used in fit (N_s).

Table S1b. Fisher mean component directions derived from 10020,234 data in Table S1a.

Subsamples	Component	Dec. (°)	Inc. (°)	a_{95} (°)	k	N
234b1, 234b2, 234b4	LC	70.2	-6.9	13.3	143.0	3
	HC	246.4	13.3	7.97	240.4	3
234c, 234d	HC	6.8	-80.8	77.4	6.3	2

Note: Subsamples b1, b2, and b4 are mutually oriented. Subsamples c and d are also mutually oriented, but are derived from a chip not oriented with respect to the parent sample. The first column gives the names of the subsamples used to compute the mean direction; the second column gives the component name; the third column gives the declination of the mean direction; the fourth column gives the inclination of the mean direction; the fifth column gives the 95% angular confidence interval (a_{95}); the sixth column gives the Fisher precision parameter (k); and the seventh column gives the number of subsamples (N).

Table S2. NRM paleointensity estimates for LC and HC components in 10020.

Sample, Experiment	LC slope	HC slope	HC Paleointensity (μT)	HC Paleointensity, Anisotropy-Corrected (μT)
234c				
ARM 50 μT	-	0.54 ± 0.13	20.1 ± 6.6	-
ARM 200 μT	-	0.21 ± 0.04	31.2 ± 1.8	-
ARM 600 μT	-	-	-	-
IRM	0.082 ± 0.007	0.011 ± 0.002	33.4 ± 0.1	-
234d				
ARM 50 μT	-	1.25 ± 0.08	46.5 ± 4.0	46.5 ± 4.0
ARM 200 μT	-	0.31 ± 0.01	45.6 ± 0.6	45.6 ± 0.6
ARM 600 μT	-	-	-	-
IRM	0.025 ± 0.005	0.016 ± 0.001	47.3 ± 0.02	47.7 ± 0.02
234b1				
ARM 50 μT	-	1.71 ± 0.07	63.8 ± 3.3	65.9 ± 3.3
ARM 200 μT	-	0.47 ± 0.01	70.1 ± 0.6	72.5 ± 0.6
ARM 600 μT	-	0.200 ± 0.005	88.7 ± 0.2	91.7 ± 0.2
IRM	0.027 ± 0.007	0.039 ± 0.001	117.3 ± 0.03	125.3 ± 0.03
234b2				
ARM 50 μT	-	1.65 ± 0.10	61.6 ± 5.1	61.1 ± 5.0
ARM 200 μT	-	0.40 ± 0.02	59.9 ± 1.0	59.4 ± 1.0
ARM 600 μT	-	0.16 ± 0.01	71.6 ± 0.4	71.0 ± 0.4
IRM	0.029 ± 0.006	0.025 ± 0.003	76.6 ± 0.1	76.3 ± 0.1
234b4				
ARM 50 μT	-	1.55 ± 0.09	57.7 ± 4.3	42.5 ± 4.3
ARM 200 μT	-	0.43 ± 0.01	63.5 ± 0.7	46.8 ± 0.7
ARM 600 μT	-	0.18 ± 0.05	79.1 ± 0.3	58.3 ± 0.3
IRM	0.084 ± 0.008	0.026 ± 0.001	79.4 ± 0.04	48.3 ± 0.04
<i>Mean Values</i>				
<i>ARM 50 μT</i>	-	1.34 ± 0.48	49.9 ± 18.0	47.2 ± 18.0
<i>ARM 200 μT</i>	-	0.36 ± 0.10	54.1 ± 15.6	51.1 ± 15.5
<i>ARM 600 μT</i>	-	0.18 ± 0.02	79.8 ± 8.6	73.7 ± 16.9
<i>ARM all</i>	-	0.70 ± 0.58	58.4 ± 18.8	54.8 ± 18.8
<i>IRM all</i>	0.049 ± 0.030	0.02 ± 0.01	70.8 ± 32.5	66.2 ± 36.5

Note: The first column gives the names of the subsample and paleointensity method (first 25 rows) or the mean values derived from all samples (last 6 rows); the second column gives the slope for the LC component inferred from plots of NRM lost vs. IRM lost; the third column gives the slope for the HC component inferred from plots of NRM lost vs. IRM lost or NRM lost vs. ARM gained; the fourth column gives ARM paleointensity in $\mu\text{T} = (\text{NRM lost})/(\text{ARM gained})/f' \times (\text{bias field in } \mu\text{T})$ or IRM paleointensity in $\mu\text{T} = (\text{NRM lost})/(\text{IRM lost}) \times a$ where we used $f' = 1.34$ and $a = 3000$; the fifth column gives corrected paleointensities using the ARM anisotropy ellipsoid measured for each sample following ref. (45). Uncertainties on each paleointensity value in rows 1-25 are formal 95% confidence intervals on the slope fit using Student's t -test (102) and do not include the factor of ~ 3 -5 uncertainty associated with the unknown ratios of ARM and IRM to TRM. Uncertainties on mean values are observed 1 standard deviation from multiple samples. 10020,234c was partially consumed for Ar analyses before its anisotropy ellipsoid could be measured. Nevertheless, the relatively large mass of this sample

suggests that anisotropy corrections for the paleointensities should be negligible. We assumed this for 234c when calculating the mean anisotropy-corrected values. Calculated values are rounded to the nearest decimal place but calculations were conducted with raw data.

Table S3. Paleointensity fidelity estimates for 10020,234d. Recovered intensity calculated via the ARM method with a bias field of 200 μ T.

ARM DC Bias Field (μ T)	TRM-Equivalent Field (μ T)	Recovered Intensity (μ T)	Uncertainty (%)
10	7.46	9.61	0.55
20	14.93	18.77	0.91
50	37.31	37.18	1.113
100	74.63	81.97	1.63

Note: ARM paleointensity in μ T = (NRM/ARM)/ f' \times (bias field in μ T) using $f' = 1.34$. Uncertainties on each limit are formal 95% confidence intervals on the slope fit using Student's t -test (102).

Table S4. Rock magnetic parameters derived from remanence measurements on 10020.

Sample	MDF ARM ₂₀₀ (mT)	MDF IRM ₂₀₀ (mT)	R	H_{cr} (mT)	H_c (mT)	M_{rs} (Am ²)	M_s (Am ²)
234c	9	8	-	-/38	4.7	1.49×10^{-7}	1.30×10^{-5}
234d	13.5	14	-	-	-	-	-
234b4	22	14	0.32	53/45	-	-	-

Note: The first column gives the names of the subsample, the second column gives the mean AF destructive field for an ARM produced by a 200 mT AC field and 2 mT DC field; the third column gives the mean AF destructive field for an IRM produced by a 200 mT field; the fourth column gives the Cisowski R value (49); the fifth column gives two estimates of the coercivity of remanence (H_{cr}): the first is derived from the intersection of AF of IRM and IRM acquisition curves (Fig. S8) following (49), while the second is the back field required to reduce a saturation IRM to zero moment; the sixth column gives the coercivity (H_c), the seventh column gives the saturation remanence (M_{rs}), and the seventh column gives the saturation magnetization (M_s). A dash indicates that quantity was not measured.

Table S5. Petrography of phases in 10020.

Phase	Modal Abundance*
Pyroxene	45-46%
Plagioclase	31-34%
Fe-Ti Oxides	12-15%
Olivine	3-5%
K-Glass	1-2%

Compositions of typical metal grains ($N=3$)

Grain #	Fe	Ni	Total
14	99.8	-	99.8
15	99.1	-	99.1
16	98.1	-	98.1
Average	99	-	99
Maximum	99.8	-	99.8
Minimum	98.1	-	98.1

Compositions of larger plagioclase grains ($N=40$)

Spot #	FeO	SiO ₂	CaO	K ₂ O	Na ₂ O	Al ₂ O ₃	MgO	Total	An±	Ab±	Or±	FeO	Ca/K
80	0.73	47.2	18.1	0.03	1.12	33.7	0.31	101.2	0.9	0.1	0.002	0.73	552.5
81	0.59	46.5	18.5	0.02	0.94	34.2	0.3	101	0.91	0.08	0.001	0.59	695.4
82	0.56	46.2	18.7	0.02	0.94	34.6	0.28	101.3	0.92	0.08	0.001	0.56	914
83	0.52	45.9	18.9	0.02	0.83	35.1	0.28	101.5	0.93	0.07	0.001	0.52	769.2
84	0.4	45.5	19.1	0.02	0.72	35.2	0.25	101.2	0.93	0.06	0.001	0.4	778.3
85	0.38	45.3	19.1	0.01	0.68	35.2	0.23	101	0.94	0.06	0.001	0.38	1043.3
86	0.49	45.4	19.3	0.02	0.76	35.4	0.2	101.6	0.93	0.07	0.001	0.49	942
87	0.39	45.4	19.1	0.02	0.72	35.3	0.24	101.2	0.94	0.06	0.001	0.39	848.2
88	0.46	45.7	19.1	0.02	0.82	35	0.25	101.3	0.93	0.07	0.001	0.46	935
89	0.35	45.7	19	0.02	0.75	35.2	0.26	101.3	0.93	0.07	0.001	0.35	844.5
90	0.37	45	19.4	0.02	0.56	35.6	0.19	101.1	0.95	0.05	0.001	0.37	951
92	0.39	44.8	19.5	0.01	0.51	36	0.19	101.4	0.95	0.04	0.001	0.39	1908
93	0.32	45	19.5	0.01	0.55	35.9	0.21	101.4	0.95	0.05	0	0.32	1904
94	0.3	44.7	19.5	0.01	0.53	35.8	0.2	101	0.95	0.05	0.001	0.3	1198.8
95	0.33	44.9	19.2	0.01	0.56	35.9	0.19	101.1	0.95	0.05	0.001	0.33	1344.3

Compositions of larger plagioclase grains (*continued*)

Spot #	FeO	SiO ₂	CaO	K ₂ O	Na ₂ O	Al ₂ O ₃	MgO	Total	An#	Ab#	Or#	FeO	Ca/K
96	0.28	45.1	19.2	0.01	0.61	35.5	0.23	101	0.94	0.05	0.001	0.28	1045.6
97	0.22	45.6	19.4	0.02	0.7	35.3	0.24	101.4	0.94	0.06	0.001	0.22	945
98	0.28	45	19.4	0.02	0.62	35.8	0.23	101.3	0.94	0.05	0.001	0.28	1052.2
99	0.23	44.9	19.5	0.02	0.63	35.7	0.22	101.1	0.94	0.05	0.001	0.23	1061.1
100	0.32	44.9	19.4	0.01	0.65	35.4	0.21	100.9	0.94	0.06	0.001	0.32	1188.8
101	0.26	45.5	19	0.02	0.73	35.2	0.23	100.9	0.93	0.07	0.001	0.26	1032.2
102	0.38	45.4	19.2	0.02	0.69	35.5	0.22	101.3	0.94	0.06	0.001	0.38	1041.1
103	0.33	44.5	19	0.02	0.65	34.9	0.21	99.6	0.94	0.06	0.001	0.33	946
104	0.32	45.3	19.1	0.01	0.67	35.5	0.24	101.2	0.94	0.06	0.001	0.32	1170
60	0.47	47.6	17.8	0.03	1.26	33.3	0.31	100.7	0.88	0.11	0.002	0.47	457.4
61	0.45	47.5	18.1	0.03	1.18	33.5	0.35	101.1	0.89	0.11	0.002	0.45	466.3
62	0.41	46.6	18.5	0.04	1.02	34.2	0.33	101.1	0.91	0.09	0.002	0.41	410.9
63	0.41	46.3	18.7	0.03	0.98	34.5	0.3	101.2	0.91	0.09	0.001	0.41	608
64	0.35	46.1	18.7	0.03	0.88	34.8	0.28	101.1	0.92	0.08	0.002	0.35	610.7
65	0.35	45.7	18.9	0.02	0.8	35.1	0.26	101.1	0.93	0.07	0.001	0.35	841.8
66	0.24	45.5	19.1	0.02	0.71	35.4	0.24	101.2	0.94	0.06	0.001	0.24	936
67	0.33	45.2	19.1	0.02	0.71	35.3	0.25	101	0.94	0.06	0.001	0.33	851.8
68	0.33	45.4	19.1	0.02	0.71	35.3	0.23	101.2	0.94	0.06	0.001	0.33	780
69	0.17	45.5	19.3	0.02	0.73	35.2	0.23	101.2	0.93	0.06	0.001	0.17	858.2
70	0.36	45.5	19	0.02	0.69	35.2	0.23	101.1	0.94	0.06	0.001	0.36	775
71	0.35	45.7	19.1	0.02	0.74	35	0.23	101.1	0.93	0.07	0.001	0.35	934
72	0.32	45.6	19.1	0.02	0.76	35.3	0.25	101.3	0.93	0.07	0.001	0.32	932
73	0.36	45.6	19.1	0.02	0.74	35.2	0.23	101.2	0.93	0.07	0.001	0.36	847.3
74	0.39	45.4	19.1	0.02	0.73	35.1	0.23	101	0.93	0.06	0.001	0.39	851.8
75	0.46	45.5	19.2	0.02	0.68	35.3	0.22	101.4	0.94	0.06	0.001	0.46	936
Average	0.37	45.59	19.02	0.02	0.76	35.11	0.24	101.12	0.93	0.07	0.001	0.37	848.0
Maximum	0.73	47.55	19.53	0.04	1.26	35.98	0.35	101.63	0.95	0.11	0.002	0.73	
Minimum	0.17	44.48	17.75	0.01	0.51	33.28	0.19	99.63	0.88	0.04	0	0.17	

Compositions of typical smaller plagioclase grains ($N=15$)

Spot #	FeO	SiO ₂	CaO	K ₂ O	Na ₂ O	Al ₂ O ₃	MgO	Total	An±	Ab±	Or±	FeO	Ca/K
25	3.59	48.3	17	0.03	1.27	26.2	2.85	99.2	0.88	0.12	0.002	3.59	451.6
26	0.64	46.1	18.5	0.03	1	34.1	0.3	100.7	0.91	0.09	0.002	0.64	567.5
27	0.35	45.6	18.7	0.02	0.89	34.6	0.25	100.4	0.92	0.08	0.001	0.35	707.7
28	0.49	46	18.6	0.02	0.91	34.4	0.29	100.8	0.92	0.08	0.001	0.49	913
29	0.58	46.9	18	0.06	1.11	33.6	0.24	100.6	0.9	0.1	0.004	0.58	252.9
46	0.71	47.8	17.9	0.04	1.28	33.2	0.32	101.2	0.88	0.11	0.002	0.71	396.4
47	0.6	47.6	17.9	0.04	1.2	33.5	0.33	101.2	0.89	0.11	0.003	0.6	349.2
48	0.8	47.5	17.7	0.04	1.18	33.4	0.35	101	0.89	0.11	0.002	0.8	393.6
49	0.87	47	17.7	0.05	1.25	33	0.32	100.2	0.88	0.11	0.003	0.87	311.8
50	0.95	47.3	18.1	0.04	1.15	32.3	0.63	100.5	0.89	0.1	0.002	0.95	370.8
51	4.31	47.3	17.8	0.03	0.8	24	3.97	98.2	0.92	0.07	0.002	4.31	509.4
76	3.79	49.1	16.1	0.22	1.32	28.2	0.48	99.2	0.86	0.13	0.014	3.79	60.4
77	0.92	49.2	17.2	0.09	1.42	32.4	0.22	101.5	0.87	0.13	0.005	0.92	157.9
78	0.8	48.7	17.5	0.05	1.41	32.6	0.27	101.3	0.87	0.13	0.003	0.8	303.6
79	0.82	48.6	17.5	0.05	1.35	32.5	0.27	101	0.88	0.12	0.003	0.82	275.8
Average	1.19	47.03	17.91	0.05	1.11	32.31	0.66	100.07	0.89	0.11	0.024	1.35	271.4
Maximum	4.31	49.15	18.67	0.22	1.42	34.62	3.97	101.48	0.92	0.13	0.014	4.31	
Minimum	0.35	45.58	16.12	0.02	0.8	24.03	0.22	98.24	0.86	0.07	0.001	0.35	

Compositions of typical K-glass grains ($N=3$)

Spot #	CaO	SiO ₂	FeO	K ₂ O	Na ₂ O	Al ₂ O ₃	MgO	Total
32	2.6	75.1	1.2	4.9	0.22	10.9	0.15	95.1
33	1.6	77.2	0.8	5.7	0.21	10.96	0.08	96.5
34	1.9	76.4	1.0	5.2	0.21	10.59	0.09	95.4
Average	2.0	76.2	1.0	5.3	0.22	10.83	0.11	95.7
Maximum	2.6	77.2	1.2	5.7	0.22	10.96	0.15	96.5
Minimum	1.6	75.1	0.8	4.9	0.21	10.59	0.08	95.1

Compositions of typical pyroxene grains (*N*=16)

Spot #	CaO	Al ₂ O ₃	K ₂ O	MnO	Na ₂ O	TiO ₂	SiO ₂	Cr ₂ O ₃	FeO	MgO	NiO	Total
1	11.7	1.8	-	0.34	0.029	1.5	51.2	-	18.0	16.1	-	100.6
2	15.0	3.4	-	0.25	-	2.6	49.6	-	14.2	15.1	-	100.3
3	18.8	4.6	-	0.20	0.041	4.1	47.8	-	11.3	13.1	-	100.0
4	17.1	4.8	-	0.23	0.034	3.8	48.0	-	12.4	13.7	-	100.2
5	8.0	1.6	-	0.38	0.085	1.4	51.1	-	19.6	19.5	-	101.6
6	5.9	0.8	0.02	0.36	0.032	0.91	52.6	-	20.4	19.6	-	100.7
7	16.3	2.3	-	0.28	-	2.1	49.2	-	16.1	12.7	-	98.9
8	10.9	1.5	0.01	0.46	0.028	1.4	50.1	-	24.00	12.7	-	101.1
9	20.1	5.3	-	0.17	0.075	4.6	47.3	-	9.9	12.8	-	100.2
10	19.1	6.1	0.01	0.20	0.075	4.7	46.5	-	10.1	13.0	-	99.8
11	19.2	6.2	-	0.19	0.060	4.7	46.4	-	10.2	12.9	-	99.7
12	19.7	4.9	-	0.20	0.086	4.3	47.5	-	10.0	13.1	-	99.8
13	18.6	4.6	-	0.18	0.035	4.0	48.1	-	11.1	13.6	-	100.2
14	15.4	2.3	-	0.28	0.046	2.1	51.0	-	13.4	15.8	-	100.2
15	14.2	1.4	-	0.30	-	1.5	51.7	-	15.6	16.0	-	100.6
16	13.2	2.3	0.01	0.36	-	1.9	50.4	-	18.3	14.1	-	100.6
Average	15.2	3.4	0.01	0.27	0.040	2.9	49.3	-	14.7	14.6	-	100.3
Maximum	20.1	6.2	0.02	0.46	0.086	4.7	52.6	-	24.00	19.6	-	101.6
Minimum	5.9	0.8	0.01	0.17	0.028	0.91	46.4	-	9.9	12.7	-	98.9

Note: Analyses presented as wt% oxides rounded to the nearest decimal place. Calculations were conducted using raw data.

*Modal abundances from (13) except K-glass.

- Indicates concentration below minimum detection limit. Detection limits as follows (in wt%): Metals; Ni-0.019, Fe-0.027. Silicates; Ni-0.017, Fe-0.015 (0.0375 in feldspar), K-0.01, Cr-0.008, Na-0.014 (0.022 in pyroxene).

‡An, Ab, and Or data are presented as relative percentages (e.g., An= CaO/(Na₂O+CaO+K₂O) and rounded to the nearest decimal place.

N denotes number of analyses included in calculation. FeO, CaO, TiO₂, MnO, MgO, K₂O, and Na₂O are presented as mass percents.

Standards for Fe and Ni analyses are pure Fe and Ni metal. Silicate standards were synthetic orthoclase (K), clinopyroxene (Ca), rutile (Ti), rhodonite (Mn), and orthopyroxene (Fe, Mg).

Table S6: Analytical Details

COMPLETE ⁴⁰Ar/³⁹Ar INCREMENTAL HEATING RESULTS

#	Temp (°C)	⁴⁰ Ar ± 1σ	³⁹ Ar ± 1σ	³⁸ Ar ± 1σ	³⁷ Ar ± 1σ	³⁶ Ar ± 1σ	⁴⁰ Ar ^a (%)	³⁹ Ar _t (%)	³⁸ Ar _{cos} (%)	³⁸ Ar _{trap} (%)	³⁸ Ar _{cl} (%)	³⁶ Ar _{cos} (%)	³⁶ Ar _{trap} (%)	Ca/K	Apparent Age ± 1σ (Ma)
10020-1 whole-rock fragment															
1	460 °C	0.51600 ± 0.00276	0.00818 ± 0.00009	0.00103 ± 0.00003	0.04619 ± 0.00063	0.00061 ± 0.00004	100.0	99.6	90.4	0.0	0.0	100.0	0.0	11.1	1771 ± 17
2	459 °C	0.42904 ± 0.00260	0.00685 ± 0.00012	0.00078 ± 0.00003	0.03459 ± 0.00060	0.00065 ± 0.00005	100.0	99.6	84.0	5.3	0.0	65.2	33.4	9.9	1762 ± 22
3	513 °C	1.81550 ± 0.00267	0.02340 ± 0.00017	0.00392 ± 0.00004	0.17615 ± 0.00150	0.00255 ± 0.00004	100.0	99.5	91.8	0.8	0.0	91.4	6.8	14.8	2015 ± 13
4	513 °C	1.26244 ± 0.00273	0.01649 ± 0.00012	0.00224 ± 0.00003	0.10194 ± 0.00087	0.00147 ± 0.00004	100.0	99.6	89.7	1.2	0.0	88.2	10.0	12.2	1998 ± 13
5	566 °C	3.73898 ± 0.00426	0.03610 ± 0.00014	0.00819 ± 0.00005	0.38252 ± 0.00242	0.00555 ± 0.00005	100.0	99.3	93.4	1.1	0.0	89.3	8.9	20.9	2385 ± 12
6	566 °C	2.47455 ± 0.00356	0.02122 ± 0.00015	0.00507 ± 0.00004	0.23975 ± 0.00225	0.00339 ± 0.00004	100.0	99.2	93.9	0.9	0.0	90.9	7.2	22.3	2545 ± 15
7	619 °C	6.58017 ± 0.00485	0.04241 ± 0.00021	0.01679 ± 0.00006	0.81115 ± 0.00555	0.01122 ± 0.00006	100.0	98.7	96.3	0.6	0.0	93.3	4.8	38.0	2956 ± 14
8	620 °C	4.34691 ± 0.00894	0.02542 ± 0.00020	0.01059 ± 0.00006	0.48998 ± 0.00337	0.00709 ± 0.00005	100.0	98.7	96.4	0.6	0.0	93.3	4.9	38.3	3099 ± 17
9	672 °C	10.43597 ± 0.00685	0.05096 ± 0.00014	0.03077 ± 0.00009	1.50736 ± 0.01101	0.02055 ± 0.00009	100.0	97.9	97.5	0.4	0.0	94.5	3.5	59.2	3381 ± 13
10	672 °C	6.52629 ± 0.00503	0.03047 ± 0.00013	0.01898 ± 0.00006	0.94461 ± 0.00452	0.01265 ± 0.00008	100.0	97.8	97.6	0.4	0.0	94.8	3.2	62.1	3452 ± 14
11	725 °C	14.83099 ± 0.00435	0.06285 ± 0.00030	0.05625 ± 0.00013	2.84560 ± 0.01866	0.03775 ± 0.00012	100.0	96.9	98.2	0.4	0.0	94.7	3.3	91.6	3618 ± 15
12	725 °C	8.96590 ± 0.00629	0.03741 ± 0.00023	0.03755 ± 0.00009	1.90419 ± 0.01004	0.02484 ± 0.00008	100.0	96.5	98.5	0.2	0.0	96.5	1.5	103.4	3649 ± 16
13	776 °C	17.55852 ± 0.00884	0.07154 ± 0.00027	0.08768 ± 0.00014	4.51674 ± 0.03618	0.05945 ± 0.00025	100.0	95.6	98.4	0.5	0.0	94.0	4.0	129.4	3700 ± 14
14	777 °C	9.70741 ± 0.00629	0.03959 ± 0.00020	0.04980 ± 0.00011	2.53338 ± 0.01187	0.03351 ± 0.00010	100.0	95.6	98.6	0.4	0.0	94.9	3.1	131.3	3699 ± 15
15	828 °C	16.04087 ± 0.00818	0.06485 ± 0.00027	0.08296 ± 0.00016	4.14558 ± 0.03272	0.05511 ± 0.00013	100.0	95.6	98.8	0.2	0.0	96.3	1.7	131.1	3713 ± 14
16	829 °C	8.54890 ± 0.00504	0.03392 ± 0.00022	0.04413 ± 0.00010	2.28319 ± 0.01257	0.02938 ± 0.00009	100.0	95.3	98.8	0.2	0.0	96.1	1.8	138.4	3747 ± 16
17	880 °C	13.26167 ± 0.00854	0.05423 ± 0.00028	0.06785 ± 0.00014	3.43464 ± 0.02953	0.04554 ± 0.00012	100.0	95.6	98.6	0.4	0.0	95.2	2.8	130.2	3695 ± 15
18	879 °C	6.26351 ± 0.01101	0.02664 ± 0.00018	0.03375 ± 0.00010	1.69898 ± 0.01186	0.02263 ± 0.00007	100.0	95.5	98.7	0.3	0.0	95.3	2.7	134.0	3671 ± 32
19	931 °C	10.66180 ± 0.01102	0.04674 ± 0.00014	0.04897 ± 0.00012	2.41054 ± 0.01392	0.03295 ± 0.00019	100.0	96.4	98.4	0.4	0.0	94.7	3.4	104.8	3572 ± 21
20	931 °C	3.86213 ± 0.01102	0.01693 ± 0.00015	0.02006 ± 0.00008	0.96721 ± 0.00560	0.01354 ± 0.00007	100.0	96.0	98.5	0.5	0.0	94.5	3.6	116.6	3579 ± 48
21	982 °C	6.70207 ± 0.01103	0.03029 ± 0.00021	0.03878 ± 0.00009	1.71628 ± 0.00745	0.02684 ± 0.00016	100.0	96.1	98.2	0.8	0.0	91.9	6.4	115.6	3569 ± 30
22	982 °C	2.08706 ± 0.01101	0.00819 ± 0.00011	0.01360 ± 0.00006	0.59781 ± 0.00268	0.00923 ± 0.00005	100.0	94.9	98.7	0.5	0.0	94.3	4.0	150.8	3771 ± 87
23	1032 °C	5.16768 ± 0.01106	0.02429 ± 0.00011	0.09735 ± 0.00016	4.22515 ± 0.02643	0.06480 ± 0.00024	100.0	87.9	99.5	0.2	0.0	96.8	1.5	387.8	3607 ± 36
24	1031 °C	1.52820 ± 0.01101	0.00698 ± 0.00005	0.03288 ± 0.00010	1.44085 ± 0.00828	0.02245 ± 0.00017	100.0	85.7	99.1	0.5	0.0	94.1	4.2	472.1	3692 ± 115
25	1083 °C	8.79280 ± 0.01104	0.05516 ± 0.00024	0.62380 ± 0.00058	27.27059 ± 0.10471	0.04156 ± 0.00100	100.0	65.6	99.8	0.0	0.0	98.0	0.3	1476.4	3613 ± 28
26	1083 °C	0.99286 ± 0.00200	0.00791 ± 0.00013	0.13728 ± 0.00021	5.77289 ± 0.03712	0.09082 ± 0.00032	100.0	49.3	99.8	0.1	0.0	97.7	0.6	2904.6	3689 ± 58
27	1133 °C	1.15920 ± 0.00197	0.01131 ± 0.00008	0.23372 ± 0.00039	9.66704 ± 0.08508	0.15455 ± 0.00040	100.0	40.6	99.8	0.1	0.0	97.8	0.6	4128.9	3675 ± 47
28	1132 °C	0.00611 ± 0.00140	0.00009 ± 0.00005	0.00019 ± 0.00001	0.00921 ± 0.00031	0.00012 ± 0.00002									
29	1182 °C	0.00967 ± 0.00140	0.00004 ± 0.00006	0.00042 ± 0.00001	0.00762 ± 0.00031	0.00031 ± 0.00002									
30	1179 °C	0.00564 ± 0.00137	0.00004 ± 0.00005	0.00021 ± 0.00001	0.00282 ± 0.00025	0.00015 ± 0.00002									
31	1232 °C	0.00344 ± 0.00135	-0.00004 ± 0.00006	0.00014 ± 0.00001	0.00227 ± 0.00026	0.00005 ± 0.00001									
32	1231 °C	0.00242 ± 0.00135	0.00008 ± 0.00005	0.00002 ± 0.00001	0.00020 ± 0.00022	0.00000 ± 0.00001									
33	1281 °C	0.01441 ± 0.00135	0.00052 ± 0.00006	0.00007 ± 0.00001	0.00103 ± 0.00027	0.00007 ± 0.00002									
34	1280 °C	0.01390 ± 0.00134	0.00058 ± 0.00005	0.00009 ± 0.00001	0.00045 ± 0.00026	0.00005 ± 0.00001									
35	1330 °C	0.02555 ± 0.00142	0.00089 ± 0.00005	0.00007 ± 0.00001	0.00050 ± 0.00026	0.00012 ± 0.00001									
36	1330 °C	0.02263 ± 0.00146	0.00068 ± 0.00005	0.00007 ± 0.00001	0.00064 ± 0.00027	0.00009 ± 0.00001									
10020-2 whole-rock fragment															
1	460 °C	1.02492 ± 0.00271	0.01564 ± 0.00011	0.00188 ± 0.00003	0.08112 ± 0.00072	0.00131 ± 0.00004	100.0	99.6	87.7	2.2	0.0	16.6	16.6	10.2	1814 ± 12
2	460 °C	0.77929 ± 0.00262	0.01249 ± 0.00010	0.00119 ± 0.00002	0.04994 ± 0.00062	0.00070 ± 0.00005	100.0	99.7	86.9	0.2	0.0	96.0	2.1	7.9	1757 ± 13
3	513 °C	2.87722 ± 0.00437	0.03588 ± 0.00018	0.00496 ± 0.00004	0.22043 ± 0.00222	0.00303 ± 0.00006	100.0	99.6	90.9	0.2	0.0	96.4	1.7	12.1	2054 ± 12
4	513 °C	2.00229 ± 0.00293	0.02422 ± 0.00011	0.00131 ± 0.00004	0.12933 ± 0.00093	0.00193 ± 0.00004	100.0	99.6	90.0	0.5	0.0	94.0	4.2	10.5	2091 ± 11
5	566 °C	5.66836 ± 0.00485	0.05031 ± 0.00014	0.01026 ± 0.00005	0.47600 ± 0.00296	0.00666 ± 0.00008	100.0	99.3	93.4	0.6	0.0	93.2	4.9	18.7	2496 ± 11
6	566 °C	3.80507 ± 0.00443	0.03014 ± 0.00013	0.00454 ± 0.00005	0.29822 ± 0.00243	0.00404 ± 0.00007	100.0	99.3	94.4	-0.1	0.0	98.8	-0.8	19.5	2653 ± 13
7	619 °C	9.99569 ± 0.00583	0.05805 ± 0.00026	0.02084 ± 0.00007	0.95659 ± 0.00519	0.01386 ± 0.00008	100.0	98.9	96.0	0.6	0.0	93.4	4.7	32.7	3106 ± 14
8	619 °C	6.61146 ± 0.00460	0.03490 ± 0.00021	0.01303 ± 0.00005	0.60549 ± 0.00411	0.00852 ± 0.00006	100.0	98.8	96.3	0.3	0.0	95.4	2.8	34.4	3250 ± 15
9	672 °C	15.54589 ± 0.00713	0.07096 ± 0.00027	0.03592 ± 0.00008	1.76514 ± 0.00915	0.02478 ± 0.00017	100.0	98.3	96.6	1.0	0.0	90.7	7.5	49.6	3480 ± 14
10	672 °C	9.71369 ± 0.00602	0.04166 ± 0.00023	0.02260 ± 0.00007	1.11102 ± 0.00527	0.01523 ± 0.00007	100.0	98.1	97.1	0.6	0.0	93.3	4.8	53.3	3579 ± 15
11	725 °C	22.03431 ± 0.01127	0.08910 ± 0.00035	0.06484 ± 0.00013	3.23464 ± 0.01885	0.04331 ± 0.00011	100.0	97.5	97.9	0.4	0.0	94.9	3.1	73.0	3681 ± 14
12	724 °C	14.04383 ± 0.00760	0.05731 ± 0.00023	0.04568 ± 0.00011	2.29555 ± 0.00948	0.03023 ± 0.00020	100.0	97.2	98.2	0.2	0.0	96.1	1.9	80.8	3671 ± 14
13	775 °C	25.96550 ± 0.01127	0.10431 ± 0.00033	0.09314 ± 0.00013	4.79585 ± 0.04191	0.06292 ± 0.00027	100.0	96.8	98.1	0.5	0.0	94.0	4.0	93.1	3703 ± 13
14	775 °C	14.54644 ± 0.00657	0.05743 ± 0.00028	0.05208 ± 0.00011	2.62941 ± 0.01034	0.03597 ± 0.00020	100.0	96.8	97.8	0.8	0.0	91.7	6.4	92.7	3730 ± 15
15	829 °C	23.89024 ± 0.00913	0.09558 ± 0.00033	0.08652 ± 0.00015	4.36456 ± 0.02503	0.05799 ± 0.00027	100.0	96.8	98.2	0.4	0.0	94.9	3.1	92.4	3709 ± 14
16	829 °C	13.14192 ± 0.00780	0.05276 ± 0.00025	0.04888 ± 0.00010	2.44240 ± 0.01297	0.03287 ± 0.00015	100.0	96.8	98.2	0.4	0.0	94.6	3.4	93.8	3704 ± 15
17	879 °C	20.12732 ± 0.00893	0.08162 ± 0.00035	0.07627 ± 0.00015	3.80649 ± 0.02560	0.05135 ± 0.00024	100.0	96.8	98.2	0.5	0.0	94.5	3.6	94.5	3689 ± 14
18	880 °C	9.32794 ± 7													

Table S7: Summary of cosmic ray exposure ages

Aliquot	Phase	Cosmochron Analysis		
		Steps Used	$^{38}\text{Ar}_{\text{cos}}/^{37}\text{Ar}_{\text{Ca}} \pm 1\sigma$	CRE Age (Ma) $\pm 1\sigma$
10020,234c1	Plag	10 - 18	0.0194 ± 0.0002	101.8 ± 0.8
10020,234c2	Plag	9 - 18	0.0196 ± 0.0001	102.6 ± 0.6

CRE Ages calculated using the following parameters:

^{38}Ar Prod. Rates (10^{-13} moles/gCa/Ma):

Plagioclase = 8.081

Pyroxene = 8.795

γ , which relates ^{37}Ar produced during the neutron irradiation to the mass of Ca, is 4.24×10^{-9} moles/gCa

Table S8: Summary of MP-MDD model parameters

Phase	E_a (kJ/mol)	$\ln(D_0/a^2)_1$ [ln(s ⁻¹)]	Φ_{1-39}	Φ_{1-37}	Ca/K	P_{38Ca} (mol/g _{Ca} /Ma)	$\ln(D_0/a^2)_2$ [ln(s ⁻¹)]	Φ_{2-39}	Φ_{2-37}	Ca/K	P_{38Ca} (mol/g _{Ca} /Ma)
Plagioclase	200	12.4	0.060	0.599	895	8.08×10^{-15}	10.9	0.052	0.398	686	8.09×10^{-15}
K-Glass	138	8.7	0.210	0.001	0.43	3.85×10^{-14}	5.0	0.678	0.002	0.26	5.73×10^{-14}

Each phase is fit with a two domain model.

Φ_{X-Y} is the proportion of $^{39}\text{Ar}_K$ ($Y = 39$) or $^{37}\text{Ar}_{Ca}$ ($Y = 37$) contained within a given domain ($X = 1$ or 2) and is calculated based on the total Ar released in the first 20 extractions, with an overall Ca/K ratio of 88.1.

P_{38Ca} is the domain-specific production rate for $^{38}\text{Ar}_{cos}$.

Total $^{39}\text{Ar}_K$, $^{37}\text{Ar}_{Ca}$, and $^{38}\text{Ar}_{cos}$ signals were 0.694, 31.5, and 0.616 nanoamps, respectively.

Database S1: NRM AF demagnetization data in Caltech-standard date format (in cgs units) for 10020 subsamples 234c, 234d, 234b1, 234b2, 234b4, readable with the PaleoMag program (available at <http://cires.colorado.edu/people/jones.craig/PMag3.html>). Database contains a readme.txt file, .sam file for all subsamples (data file directory) and individual .rmg files (extended data files not readable with PaleoMag) and extensionless files (simplified data files readable with PaleoMag). Columns in the .rmg files are as follows: NRM (emu), AF level (G), Mz (emu) (geographic coordinates), Mx (emu) (geographic coordinates), My (emu) (geographic coordinates), M (emu), and date/time.

References and Notes

1. M. Fuller, S. M. Cisowski, in *Geomagnetism*, J. A. Jacobs, Ed. (Academic Press, Orlando, FL, 1987), vol. 2, pp. 307–455.
2. L. L. Hood, N. A. Artemieva, Antipodal effects of lunar basin-forming impacts: Initial 3D simulations and comparisons with observations. *Icarus* **193**, 485 (2008).
[doi:10.1016/j.icarus.2007.08.023](https://doi.org/10.1016/j.icarus.2007.08.023)
3. D. A. Crawford, P. H. Schultz, Electromagnetic properties of impact-generated plasma, vapor and debris. *Int. J. Impact Eng.* **23**, 169 (1999). [doi:10.1016/S0734-743X\(99\)00070-6](https://doi.org/10.1016/S0734-743X(99)00070-6)
4. I. Garrick-Bethell, B. P. Weiss, D. L. Shuster, J. Buz, Early lunar magnetism. *Science* **323**, 356 (2009). [doi:10.1126/science.1166804](https://doi.org/10.1126/science.1166804) [Medline](#)
5. R. C. Weber, P.-Y. Lin, E. J. Garnero, Q. Williams, P. Lognonné, Seismic detection of the lunar core. *Science* **331**, 309 (2011). [doi:10.1126/science.1199375](https://doi.org/10.1126/science.1199375) [Medline](#)
6. J. R. Williams, D. H. Boggs, C. F. Yoder, J. T. Ratcliff, J. O. Dickey, Lunar rotational dissipation in solid body and molten core. *J. Geophys. Res.* **106**, 27933 (2001).
[doi:10.1029/2000JE001396](https://doi.org/10.1029/2000JE001396)
7. D. J. Stevenson, Planetary magnetic fields: Achievements and prospects. *Space Sci. Rev.* **152**, 651 (2010). [doi:10.1007/s11214-009-9572-z](https://doi.org/10.1007/s11214-009-9572-z)
8. D. R. Stegman, A. M. Jellinek, S. A. Zatman, J. R. Baumgardner, M. A. Richards, An early lunar core dynamo driven by thermochemical mantle convection. *Nature* **421**, 143 (2003). [doi:10.1038/nature01267](https://doi.org/10.1038/nature01267) [Medline](#)
9. W. Konrad, T. Spohn, Thermal history of the Moon: Implications for an early core dynamo and post-accretionary magmatism. *Adv. Space Res.* **19**, 1511 (1997). [doi:10.1016/S0273-1177\(97\)00364-5](https://doi.org/10.1016/S0273-1177(97)00364-5)
10. M. Le Bars, M. A. Wiczeorek, Ö. Karatekin, D. Cébron, M. Laneuville, An impact-driven dynamo for the early Moon. *Nature* **479**, 215 (2011). [doi:10.1038/nature10565](https://doi.org/10.1038/nature10565) [Medline](#)
11. C. A. Dwyer, D. J. Stevenson, F. Nimmo, A long-lived lunar dynamo driven by continuous mechanical stirring. *Nature* **479**, 212 (2011). [doi:10.1038/nature10564](https://doi.org/10.1038/nature10564) [Medline](#)
12. D. W. Beaty, A. L. Albee, *Proc. Lunar Planet. Sci. Conf. 11th*, 23 (1980).
13. D. W. Beaty, A. L. Albee, *Proc. Lunar Planet. Sci. Conf. 9th*, 359 (1978).
14. E. Roedder, P. W. Weiblen, *Proc. Apollo 11 Lunar Sci. Conf.*, 801 (1970).
15. M. R. Dence, J. A. V. Douglas, A. G. Plant, R. J. Traill, *Proc. Apollo 11 Lunar Sci. Conf.*, 315 (1970).
16. S. E. Haggerty, F. R. Boyd, P. M. Bell, L. W. Finger, W. B. Bryan, *Proc. Apollo 11 Lunar Sci. Conf.*, 513 (1970).
17. J. Geiss *et al.*, Absolute time scale of lunar mare formation and filling. *Philos. Trans. R. Soc. London Ser. A* **285**, 151 (1977). [doi:10.1098/rsta.1977.0051](https://doi.org/10.1098/rsta.1977.0051)
18. S. Guggisberg *et al.*, *Proc. Lunar Planet. Sci. Conf. 10th*, 1 (1979).

19. G. A. Snyder, D.-C. Lee, L. A. Taylor, A. N. Halliday, E. A. Jerde, Evolution of the upper mantle of the Earth's Moon: Neodymium and strontium isotopic constraints from high-Ti mare basalts. *Geochim. Cosmochim. Acta* **58**, 4795 (1994). [doi:10.1016/0016-7037\(94\)90209-7](https://doi.org/10.1016/0016-7037(94)90209-7)
20. D. W. Collinson, S. K. Runcorn, A. Stephenson, A. J. Manson, *Proc. Lunar Sci. Conf. 3rd*, 2343 (1972).
21. T. L. Grove, D. Walker, *Proc. Lunar Sci. Conf. 8th*, 1501 (1977).
22. K. P. Lawrence, C. L. Johnson, L. Tauxe, J. Gee, Lunar paleointensity measurements: Implications for lunar magnetic evolution. *Phys. Earth Planet. Inter.* **168**, 71 (2008). [doi:10.1016/j.pepi.2008.05.007](https://doi.org/10.1016/j.pepi.2008.05.007)
23. G. W. Pearce, D. W. Strangway, *Apollo 16 Preliminary Science Report. NASA SP-315* (NASA, Washington, DC, 1972), pp. 7-55 to 7-58.
24. B. P. Weiss *et al.*, Magnetism on the angrite parent body and the early differentiation of planetesimals. *Science* **322**, 713 (2008). [doi:10.1126/science.1162459](https://doi.org/10.1126/science.1162459) [Medline](#)
25. P. R. Renne, G. Balco, K. Ludwig, R. Mundil, K. Min, Response to the comment by W. H. Schwarz *et al.* on “Joint determination of ^{40}K decay constants and $^{40}\text{Ar}^*/^{40}\text{K}$ for the Fish Canyon sanidine standard, and improved accuracy for $^{40}\text{Ar}/^{39}\text{Ar}$ geochronology” by P. R. Renne *et al.* (2010). *Geochim. Cosmochim. Acta* **75**, 5097 (2011). [doi:10.1016/j.gca.2011.06.021](https://doi.org/10.1016/j.gca.2011.06.021)
26. G. Turner, $^{40}\text{Ar}/^{39}\text{Ar}$ ages from the lunar maria. *Earth Planet. Sci. Lett.* **11**, 169 (1971). [doi:10.1016/0012-821X\(71\)90161-0](https://doi.org/10.1016/0012-821X(71)90161-0)
27. Some other thermal histories cannot be excluded by the Ar data alone. However, the combination of Ar data with geologic constraints strongly favors solar heating as the only major thermal disturbance after primary cooling (SOM 6).
28. C. R. Chapman, B. A. Cohen, D. H. Grinspoon, What are the real constraints on the existence and magnitude of the late heavy bombardment? *Icarus* **189**, 233 (2007). [doi:10.1016/j.icarus.2006.12.020](https://doi.org/10.1016/j.icarus.2006.12.020)
29. H. Fechtig, S. T. Kalbitzer, in *Potassium Argon Dating*, O. A. Schaeffer, J. Zahringer, Eds. (Springer-Verlag, New York, 1966), pp. 68–107.
30. J. L. Kirschvink, R. E. Kopp, T. D. Raub, C. T. Baumgartner, J. W. Holt, Rapid, precise, and high-sensitivity acquisition of paleomagnetic and rock-magnetic data: Development of a low-noise automatic sample changing system for superconducting rock magnetometers. *Geochem. Geophys. Geosys.* **9**, Q05Y01 (2008).
31. B. P. Weiss, J. Gattacceca, S. Stanley, P. Rochette, U. R. Christensen, Paleomagnetic records of meteorites and early planetesimal differentiation. *Space Sci. Rev.* **152**, 341 (2010). [doi:10.1007/s11214-009-9580-z](https://doi.org/10.1007/s11214-009-9580-z)
32. J. R. Dunn, M. Fuller, On the remanent magnetism of lunar samples with special reference to 10048,55 and 14053.48. *Proc. Lunar Sci. Conf. 3rd*, 2363 (1972).
33. J. L. Kirschvink, The least-squares line and plane and the analysis of paleomagnetic data: Examples from Siberia and Morocco. *Geophys. J. R. Astron. Soc.* **62**, 699 (1980).

34. L. Tauxe, H. Staudigel, Strength of the geomagnetic field in the Cretaceous Normal Superchron: New data from submarine basaltic glass of the Troodos Ophiolite. *Geochem. Geophys. Geosyst.* **5**, Q02H06 (2004). [doi:10.1029/2003GC000635](https://doi.org/10.1029/2003GC000635)
35. A. R. Muxworthy, D. Heslop, G. A. Paterson, D. Michalk, A Preisach method for estimating absolute paleofield intensity under the constraint of using only isothermal measurements: 2. Experimental testing. *J. Geophys. Res.* **116**, (2011). 10.1029/2010JB007844
36. A. R. Muxworthy, D. Heslop, A Preisach method for estimating absolute paleofield intensity under the constraint of using only isothermal measurements: 1. Theoretical framework. *J. Geophys. Res.* **116**, (2011). 10.1029/2010JB007843
37. J. Gattacceca, P. Rochette, Toward a robust normalized magnetic paleointensity method applied to meteorites. *Earth Planet. Sci. Lett.* **227**, 377 (2004). [doi:10.1016/j.epsl.2004.09.013](https://doi.org/10.1016/j.epsl.2004.09.013)
38. Y. Yu, Paleointensity determination using anhysteretic remanence and saturation isothermal remanence. *Geochem. Geophys. Geosyst.* **11**, Q02Z12 (2010). [doi:10.1029/2009GC002804](https://doi.org/10.1029/2009GC002804)
39. G. Kletetschka, M. H. Acuna, T. Kohout, P. J. Wasilewski, J. E. P. Connerney, An empirical scaling law for acquisition of thermoremanent magnetization. *Earth Planet. Sci. Lett.* **226**, 521 (2004). [doi:10.1016/j.epsl.2004.08.001](https://doi.org/10.1016/j.epsl.2004.08.001)
40. S. M. Cisowski, D. W. Collinson, S. K. Runcorn, A. Stephenson, M. Fuller, A review of lunar paleointensity data and implications for the origin of lunar magnetism. *Proc. Lunar Planet. Sci. Conf. 13th*, A691 (1983).
41. Y. J. Yu, How accurately can NRM/SIRM determine the ancient planetary magnetic field intensity. *Earth Planet. Sci. Lett.* **250**, 27 (2006). [doi:10.1016/j.epsl.2006.07.027](https://doi.org/10.1016/j.epsl.2006.07.027)
42. Y. Yu, L. Tauxe, J. S. Gee, A linear field dependence of thermoremanence in low magnetic fields. *Phys. Earth Planet. Inter.* **162**, 244 (2007). [doi:10.1016/j.pepi.2007.04.008](https://doi.org/10.1016/j.pepi.2007.04.008)
43. S. Weisberg, *Applied Linear Regression* (Wiley, New York, 1985).
44. A. Stephenson, S. K. Runcorn, D. W. Collinson, Paleointensity estimates from lunar samples 10017 and 10020. *Proc. Lunar Sci. Conf. 8th*, 679 (1977).
45. P. A. Selkin, J. S. Gee, L. Tauxe, W. P. Meurer, A. J. Newell, The effect of remanence anisotropy on paleointensity estimates: A case study from the Archean Stillwater Complex. *Earth Planet. Sci. Lett.* **183**, 403 (2000). [doi:10.1016/S0012-821X\(00\)00292-2](https://doi.org/10.1016/S0012-821X(00)00292-2)
46. S. M. Tikoo *et al.*, Fidelity of mare basalts as magnetic recorders and implications for lunar paleomagnetism. *EOS Trans. AGU Fall Meeting*, abs. GP43B (2010).
47. D. J. Dunlop, K. S. Argyle, Thermoremanence, anhysteretic remanence, and susceptibility of submicron magnetites: Nonlinear field dependence and variation with grain size. *J. Geophys. Res.* **102**, 20199 (1997). [doi:10.1029/97JB00957](https://doi.org/10.1029/97JB00957)
48. M. Fuller, Lunar magnetism. *Rev. Geophys. Space Phys.* **12**, 23 (1974). [doi:10.1029/RG012i001p00023](https://doi.org/10.1029/RG012i001p00023)

49. S. M. Cisowski, Interacting vs. non-interacting single domain behavior in natural and synthetic samples. *Phys. Earth Planet. Inter.* **26**, 56 (1981). [doi:10.1016/0031-9201\(81\)90097-2](https://doi.org/10.1016/0031-9201(81)90097-2)
50. W. Lowrie, M. Fuller, On the alternating-field demagnetization characteristics of multidomain thermoremanent magnetization in magnetite. *J. Geophys. Res.* **76**, 6339 (1971). [doi:10.1029/JB076i026p06339](https://doi.org/10.1029/JB076i026p06339)
51. S. Xu, D. J. Dunlop, Toward a better understanding of the Lowrie-Fuller test. *J. Geophys. Res.* **100**, 22533 (1995). [doi:10.1029/95JB02154](https://doi.org/10.1029/95JB02154)
52. T. Kohout, G. Kletetschka, F. Donadini, M. Fuller, E. Herrero-Bervera, Analysis of the natural remanent magnetization of rocks by measuring the efficiency ratio through alternating field demagnetization spectra. *Stud. Geophys. Geod.* **52**, 225 (2008). [doi:10.1007/s11200-008-0015-1](https://doi.org/10.1007/s11200-008-0015-1)
53. P. Wasilewski, Magnetic characterization of the new magnetic mineral tetrataenite and its contrast with isochemical taenite. *Phys. Earth Planet. Inter.* **52**, 150 (1988). [doi:10.1016/0031-9201\(88\)90063-5](https://doi.org/10.1016/0031-9201(88)90063-5)
54. L. J. Srnka, Spontaneous magnetic field generation in hypervelocity impacts. *Proc. Lunar Sci. Conf. 8th*, 785 (1977).
55. J. Gattacceca *et al.*, On the efficiency of shock magnetization processes. *Phys. Earth Planet. Inter.* **166**, 1 (2008). [doi:10.1016/j.pepi.2007.09.005](https://doi.org/10.1016/j.pepi.2007.09.005)
56. J. Gattacceca *et al.*, Can the lunar crust be magnetized by shock: Experimental groundtruth. *Earth Planet. Sci. Lett.* **299**, 42 (2010). [doi:10.1016/j.epsl.2010.08.011](https://doi.org/10.1016/j.epsl.2010.08.011)
57. B. P. Weiss *et al.*, Paleomagnetism of impact spherules from Lonar crater, India and a test for impact-generated fields. *Earth Planet. Sci. Lett.* **298**, 66 (2010). [doi:10.1016/j.epsl.2010.07.028](https://doi.org/10.1016/j.epsl.2010.07.028)
58. K. L. Louzada *et al.*, Paleomagnetism of Lonar impact crater, India. *Earth Planet. Sci. Lett.* **275**, 308 (2008). [doi:10.1016/j.epsl.2008.08.025](https://doi.org/10.1016/j.epsl.2008.08.025)
59. Y. Yu, L. Tauxe, Acquisition of viscous remanent magnetization. *Phys. Earth Planet. Inter.* **159**, 32 (2006). [doi:10.1016/j.pepi.2006.05.002](https://doi.org/10.1016/j.pepi.2006.05.002)
60. A. Stephenson, S. Sadikun, D. Potter, K., A theoretical and experimental comparison of the anisotropies of magnetic susceptibility and remanence in rocks and minerals. *Geophys. J. R. Astron. Soc.* **84**, 185 (1986).
61. J. F. Nye, *Physical Properties of Crystals: Their Representation by Tensors and Matrices* (Oxford Univ. Press, Oxford, 1985).
62. T. Nagata, *Rock Magnetism* (Maruzen Company, Tokyo, 1961).
63. V. Jelinek, Characterization to the magnetic fabric of rocks. *Tectonophys.* **79**, T63 (1981). [doi:10.1016/0040-1951\(81\)90110-4](https://doi.org/10.1016/0040-1951(81)90110-4)
64. E. M. Shoemaker *et al.*, in *Apollo 11 Preliminary Science Report* (NASA Johnson Space Center, Houston, TX, 1969), pp. 41–83.

65. M. I. Staid, C. M. Pieters, J. W. Head III, Mare Tranquillitatis: Basalt emplacement history and relation to lunar samples. *J. Geophys. Res.* **101**, 23213 (1996).
[doi:10.1029/96JE02436](https://doi.org/10.1029/96JE02436)
66. G. A. Snyder, C. M. Hall, D.-C. Lee, L. A. Taylor, A. N. Halliday, Earliest high-Ti volcanism on the Moon: ^{40}Ar - ^{39}Ar , Sm-Nd, and Rb-Sr isotopic studies of Group D basalts from the Apollo 11 landing site. *Meteorit. Planet. Sci.* **31**, 328 (1996).
67. G. H. Heiken, D. T. Vaniman, B. M. French, *Lunar Sourcebook: A User's Guide to the Moon* (Cambridge Univ. Press, London, 1991).
68. C. Meyer, Lunar Sample Compendium; www-curator.jsc.nasa.gov/lunar/compendium.cfm (2011).
69. F. Hörz, E. Schneider, D. E. Gault, J. B. Hartung, D. E. Brownlee, Catastrophic rupture of lunar rocks: A Monte Carlo simulation. *Earth Moon Planets* **13**, 235 (1975).
70. M. J. Grolier, in *U.S. Geologic Survey Miscellaneous Geologic Investigations*. (U.S. Geological Survey, Washington, DC, 1970), Map I-619.
71. J. T. Armstrong, in *Microbeam Analysis*, K. F. J. Heinrich, Ed. (San Francisco Press, San Francisco, 1982), pp. 175–180.
72. J. T. Armstrong, Citzaf—A package of correction programs for the quantitative electron microbeam x-ray analysis of thick polished materials, thin-films, and particles. *Microbeam Anal.* **4**, 177 (1995).
73. J. T. Armstrong, in *Electron Probe Quantitation*, K. F. J. Heinrich, D. E. Newbury, Eds. (Plenum, Gaithersburg, MD, 1991), pp. 261–315.
74. J. L. Pouchou, F. Pichoir, in *Electron Probe Quantitation*, K. F. J. Heinrich, D. E. Newbury, Ed. (Plenum, Gaithersburg, MD, 1991), pp. 31–75.
75. I. Garrick-Bethell, B. P. Weiss, Kamacite blocking temperatures and applications to lunar magnetism. *Earth Planet. Sci. Lett.* **294**, 1 (2010). [doi:10.1016/j.epsl.2010.02.013](https://doi.org/10.1016/j.epsl.2010.02.013)
76. D. J. Dunlop, O. Ozdemir, *Rock Magnetism: Fundamentals and Frontiers* (Cambridge Univ. Press, Cambridge, 1997).
77. T. L. Grove, Cooling histories of Luna 24 very low Ti (VLT) ferrobasalts: An experimental study. *Proc. Lunar Planet. Sci. Conf. 9th*, 565 (1978).
78. D. Stöffler *et al.*, Cratering history and lunar chronology. *Rev. Mineral. Geochem.* **60**, 519 (2006). [doi:10.2138/rmg.2006.60.05](https://doi.org/10.2138/rmg.2006.60.05)
79. P. R. Renne, K. B. Knight, S. Nomade, K. N. Leung, T. P. Lou, Application of deuteron-deuteron (D-D) fusion neutrons to $^{40}\text{Ar}/^{39}\text{Ar}$ geochronology. *Appl. Radiat. Isot.* **62**, 25 (2005). [doi:10.1016/j.apradiso.2004.06.004](https://doi.org/10.1016/j.apradiso.2004.06.004) [Medline](#)
80. R. H. Steiger, E. Jäger, Subcommittee on Geochronology: Convention on use of decay constants in geochronology and cosmochronology. *Earth Planet. Sci. Lett.* **36**, 359 (1977). [doi:10.1016/0012-821X\(77\)90060-7](https://doi.org/10.1016/0012-821X(77)90060-7)
81. W. Cassata, D. L. Shuster, P. R. Renne, B. P. Weiss, Evidence for shock heating and constraints on Martian surface temperatures revealed by $^{40}\text{Ar}/^{39}\text{Ar}$ thermochronometry of

- Martian meteorites. *Geochim. Cosmochim. Acta* **74**, 6900 (2010).
[doi:10.1016/j.gca.2010.08.027](https://doi.org/10.1016/j.gca.2010.08.027)
82. R. Wieler, Cosmic-ray-produced noble gases in meteorites. *Rev. Mineral. Geochem.* **47**, 125 (2002). [doi:10.2138/rmg.2002.47.5](https://doi.org/10.2138/rmg.2002.47.5)
 83. J. Levine, P. R. Renne, R. A. Muller, Solar and cosmogenic argon in dated lunar impact spherules. *Geochim. Cosmochim. Acta* **71**, 1624 (2007). [doi:10.1016/j.gca.2006.11.034](https://doi.org/10.1016/j.gca.2006.11.034)
 84. O. Eugster, T. Michel, Common asteroid break-up events of eucrites, diogenites, and howardites and cosmic-ray production rates for noble gases in achondrites. *Geochim. Cosmochim. Acta* **59**, 177 (1995). [doi:10.1016/0016-7037\(94\)00327-I](https://doi.org/10.1016/0016-7037(94)00327-I)
 85. W. S. Cassata, P. R. Renne, D. L. Shuster, Argon diffusion in plagioclase and implications for thermochronometry: A case study from the Bushveld Complex, South Africa. *Geochim. Cosmochim. Acta* **73**, 6600 (2009). [doi:10.1016/j.gca.2009.07.017](https://doi.org/10.1016/j.gca.2009.07.017)
 86. D. L. Shuster *et al.*, A record of impacts preserved in the lunar regolith. *Earth Planet. Sci. Lett.* **290**, 155 (2010). [doi:10.1016/j.epsl.2009.12.016](https://doi.org/10.1016/j.epsl.2009.12.016)
 87. I. McDougall, M. T. Harrison, *Geochronology and Thermochronology by the $^{40}\text{Ar}/^{39}\text{Ar}$ Method* (Oxford Univ. Press, Oxford, 1999).
 88. J. Crank, *The Mathematics of Diffusion* (Oxford Univ. Press, Oxford, ed. 2, 1975).
 89. O. M. Lovera, F. M. Richter, T. M. Harrison, Diffusion domains determined by ^{39}Ar released during step heating. *J. Geophys. Res.* **96**, 2057 (1991). [doi:10.1029/90JB02217](https://doi.org/10.1029/90JB02217)
 90. G. B. Hazelton, G. Axen, O. Lovera, Argon retention properties of silicate glasses and implications for $^{40}\text{Ar}/^{39}\text{Ar}$ age and noble gas diffusion studies. *Contrib. Mineral. Petrol.* **145**, 1 (2003). [doi:10.1007/s00410-003-0440-7](https://doi.org/10.1007/s00410-003-0440-7)
 91. D. L. Shuster, K. A. Farley, The influence of artificial radiation damage and thermal annealing on helium diffusion kinetics in apatite. *Geochim. Cosmochim. Acta* **73**, 183 (2009). [doi:10.1016/j.gca.2008.10.013](https://doi.org/10.1016/j.gca.2008.10.013)
 92. A. Bischoff, D. Stoffler, Shock metamorphism as a fundamental process in the evolution of planetary bodies—information from meteorites. *Eur. J. Mineral.* **4**, 707 (1992).
 93. H. Hiesinger, R. Jaumann, G. Neukum, J. W. Head III, Ages of mare basalts on the lunar nearside. *J. Geophys. Res.* **105**, 29239 (2000). [doi:10.1029/2000JE001244](https://doi.org/10.1029/2000JE001244)
 94. P. Eberhardt *et al.*, Correlation between rock type and irradiation history of Apollo 11 igneous rocks. *Earth Planet. Sci. Lett.* **10**, 67 (1970). [doi:10.1016/0012-821X\(70\)90065-8](https://doi.org/10.1016/0012-821X(70)90065-8)
 95. K. E. Bauch, H. Hiesinger, J. Helbert, Estimation of lunar surface temperatures: A numerical model. *Lunar Planet. Sci. Conf. XL*, abs. 1789 (2009).
 96. S. Huang, Surface temperatures at the nearside of the Moon as a record of the radiation budget of Earth's climate system. *Adv. Space Res.* **41**, 1853 (2008).
[doi:10.1016/j.asr.2007.04.093](https://doi.org/10.1016/j.asr.2007.04.093)
 97. C. J. Cremers, R. C. Birkebak, J. E. White, Lunar surface temperatures from Apollo 12. *Earth Moon Planets* **3**, 346 (1971).

98. C. Huber, W. S. Cassata, P. R. Renne, A lattice-Boltzman model for noble gas diffusion in solids: The importance of domain shape and diffusive anisotropy and implications for thermochronometry. *Geochim. Cosmochim. Acta* **75**, 2170 (2011).
99. G. Turner, Argon-40/argon-39 dating of lunar rock samples. *Proc. Apollo 11 Lunar Sci. Conf.*, 1665 (1970).
100. A. Stettler, P. Eberhardt, J. Geiss, N. Grögler, P. Maurer, On the duration of lava flow activity in Mare Tranquillitatis. *Proc. Lunar Sci. Conf. 5th*, 1557 (1974).
101. D. F. McNeill, Facies and early diagenetic influence on the depositional magnetization of carbonates. *Geology* **25**, 799 (1997). [doi:10.1130/0091-7613\(1997\)025<0799:FAEDIO>2.3.CO;2](https://doi.org/10.1130/0091-7613(1997)025<0799:FAEDIO>2.3.CO;2)
102. Student, The probable error of a mean. *Biometrika* **6**, 1 (1908).